Artificial Muscles: Actuators for Biorobotic Systems

Glenn Kenneth Klute

A dissertation submitted in partial fulfillment of the
requirements for the degree of

Doctor of Philosophy

University of Washington

1999

Program Authorized to Offer Degree: Department of Bioengineering

University of Washington

Graduate School

This is to certify that I have examined this copy of a doctoral dissertation by

Glenn Kenneth Klute

And have found that it is complete and satisfactory in all respects,
and that any and all revisions required by the final
examining committee have been made.

Chair of Supervisory Committee:

Signature on Original Document
Blake Hannaford

Reading Committee:

Signature on Original Document
Blake Hannaford

Signature on Original Document
Thomas L. Daniel

Signature on Original Document
Joan E. Sanders

Date: October 11, 1999

Signature on Original Document

Date October 11, 1999

University of Washington

Abstract

Artificial Muscles: Actuators for Biorobotic Systems

Glenn Kenneth Klute

Chairperson of the Supervisory Committee:
Professor Blake Hannaford
Department of Bioengineering

Biorobotic research seeks to develop new robotic technologies based on the performance of human and animal neuromuscular systems. The development of one component of a biorobotic system, an artificial muscle and tendon, is documented here. The device is based on known static and dynamic properties of biological muscle and tendon which were extracted from the literature and used to mathematically describe the unique force, length, and velocity relationships. As biological tissue exhibits wide variation in performance, ranges are identified which encompass typical behavior for design purposes.

The McKibben pneumatic actuator is proposed as the contractile element of the artificial muscle. A model is presented that includes not only the geometric properties of the actuator, but also the material properties of the actuator's inner bladder and frictional effects. Experimental evidence is presented that validates the model and shows the force-length properties to be muscle-like, while the force-velocity properties are not. The addition of a hydraulic damper is proposed to improve the actuator's velocity-dependent properties, complete with computer simulations and experimental evidence validating the design process. Furthermore, an artificial tendon is proposed to serve as connective tissue between the artificial muscle and a skeleton. A series of experimental tests verifies that the design provides suitable tendon-like performance.

A complete model of the artificial musculo-tendon system is then presented which predicts the expected force-length-velocity performance of the artificial system. Based on the model predictions, an artificial muscle was assembled and subjected to numerous performance tests. The results exhibited muscle-like performance in general: higher activation pressures yielded higher output forces, faster concentric contractions resulted in lower force outputs, faster eccentric contractions produced higher force outputs, and output forces were higher at longer muscle lengths than shorter lengths. Furthermore, work loop tests used to experimentally measure the sustained work output during typical stretch-shortening cycles indicate the capacity to perform work increases with the magnitude of activation and is a function of both velocity and activation timing.

TABLE OF CONTENTS

LIST OF FIGURES

LIST OF TABLES

Chapter 1: Introduction

Over the past two decades, few revolutionary technological developments have occurred in the field of robotics. While United States robot shipment revenues exceeded $1.1 billion in 1997, growth beyond the traditional industries (automotive, consumer electronics, aerospace, appliance manufacturing, and the food and beverage) has been slow. Analyst explanations of this slow growth indicate small improvements in speed of operation, accuracy of movement, and magnitude of payload, coupled with the lack of technological breakthroughs to be the root cause (Anonymous, 1998; Trevelyan, 1997; Ejiri, 1996; Albus, 1990).

Expansion into new industries, such as agriculture, construction, environmental (hazardous waste), human welfare and associated medical services, and entertainment, will demand significant advances in the robotic state-of-the-art. In particular, these new robots will need to perform well in an uncontrolled, dynamic environment where a premium is placed on contact stability. Clearly, the requirements for a surgical robot interacting with both surgeon and patient are far different than those for a robot that assembles cell phones. These industries will need robotic systems that extend or augment human performance while sharing the work environment with their human operators.

Biorobotics

The "Biorobotic" approach to advancing the state-of-the-art is to emulate the very properties that allow humans to be successful. Each component of a biorobotic system incorporates as many of the known aspects of such diverse areas as neuromuscular physiology, biomechanics, and cognitive sciences, into the design of sensors, actuators, circuits, processors, and control algorithms (see figure 1.1).

The overall aim of the research presented here is to develop one component of a biorobotic system: a musculotendon-like actuator (see figure 1.2). An important step in the development is identifying the properties and performance that the artificial system is expected to achieve. These properties are based on those of the biological system. Chapter two identifies the known static and dynamic properties of biological muscle through the use of mathematical models that describe their performance. It is these criteria that an artificial muscle must be measured against. Chapter three makes note of other attempts to develop artificial muscles and focuses on the properties of one type of actuator invented by R. H. Gaylord and applied to orthotic appliances by J. L. McKibben in the late 1950's. The theoretical models presented are experimentally validated and the force-length properties are shown to be muscle-like, but the force-velocity properties require improvement.

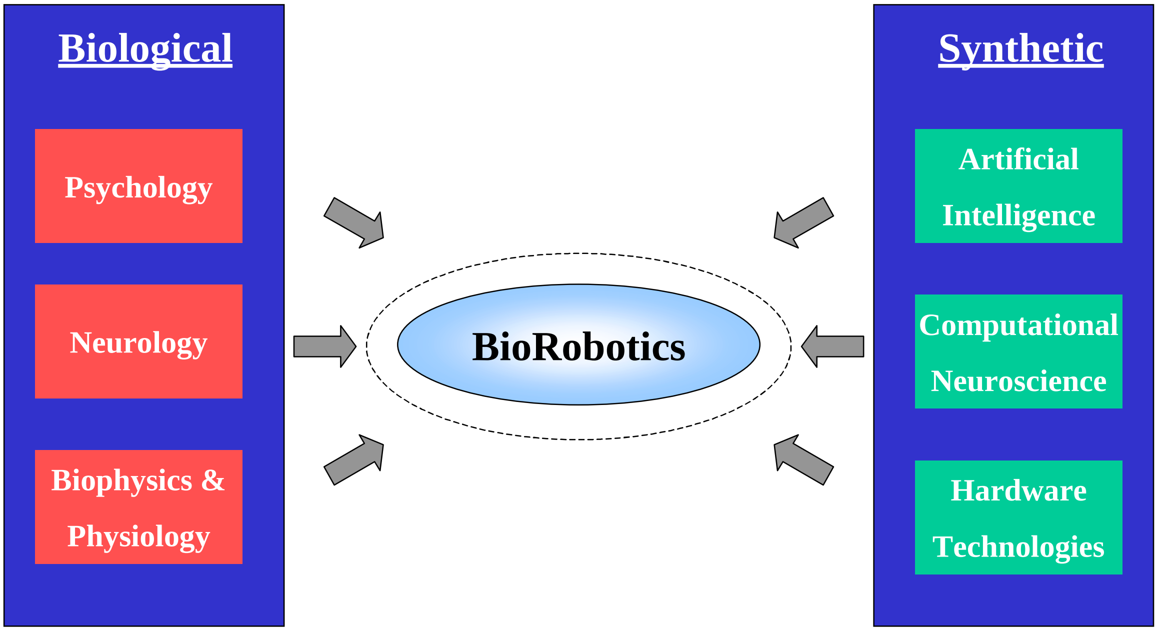

Figure 1.1: Biological and synthetic aspects of biorobotic systems [figure adapted from Franklin, 1997].

Chapter four describes the efforts to improve the force-velocity properties through the addition of a hydraulic damper. The theory used to design the damper is presented and is accompanied by experiments that validate the design process. The damper model is then combined with the McKibben actuator model and the expected performance of the simulated artificial muscle is presented.

In biological systems, muscles attach to bone through tendons. The artificial system should be no different. The properties of tendons are examined in chapter five, and design requirements for an artificial tendon are developed from the published properties of numerous mammalian tendons. A simple but effective artificial tendon that meets these requirements is presented in chapter six.

The performance of the complete artificial musculo-tendon system is presented in chapter seven. Both model and experimental results document the ability of the artificial system to mimic the performance of the biological system in terms of its force, length, and velocity properties. In chapter eight, it is noted that the force-length-velocity relationship can be used to calculate the instantaneous work performed by the artificial system. However, for biological muscle, this approach in calculating the instantaneous work is often far greater than the sustainable work performed during a cyclic operation such as locomotion. To overcome this discrepancy, the work loop method is presented to determine the amount of sustainable work produced in repeated, stretch-shortening cycles. Finally, chapter nine summarizes all of the work presented and provides suggestions for future work.

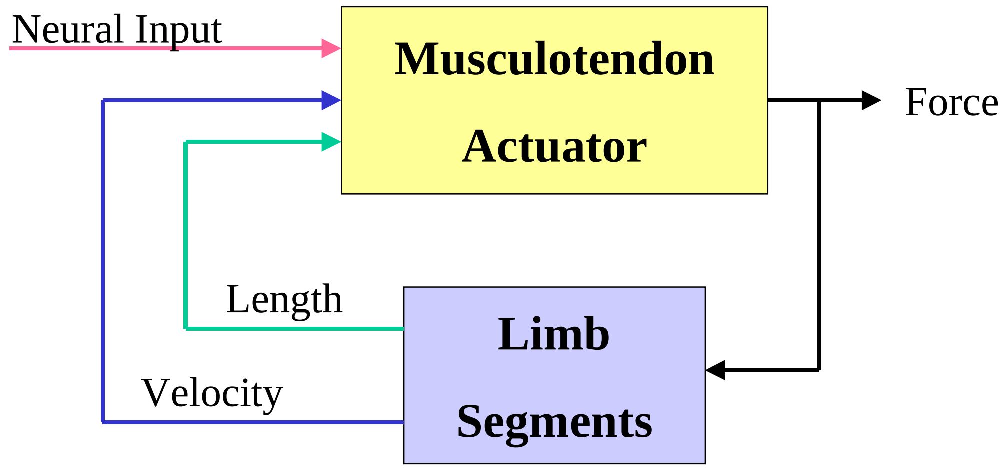

Figure 1.2: The musculo-tendon actuator system.

Chapter 2: Biological Muscle

The first step in the development of an artificial musculo-tendon system is to identify the properties to be emulated. As will be shown, muscle and tendon properties vary widely, not only between species but also within a species. The approach used here will be to present models and data of various species from the literature and then use this information as a guideline to specify a range appropriate for an artificial system.

During the last century, two muscle modeling approaches have become well established: a phenomenological approach originating with A. V. Hill (1938) and a biophysical cross-bridge model originating with A. F. Huxley (1957). Both models have received numerous contributions from contemporary researchers who continue to refine and evolve these models. Hill-based models are founded upon experiments yielding parameters for visco-elastic series and parallel elements coupled with a contractile element (see figure 2.1). The results of such models are often used to predict force, length, and velocity relationships describing muscle behavior. Huxley-based models are built upon biochemical, thermodynamic, and mechanical experiments that describe muscle at the molecular level. These models are used to understand the properties of the microscopic contractile elements.

Biomechanists, engineers, and motor control scientists using models to describe muscle behavior in applications ranging from isolated whole muscle to bi-articulate, multi-muscle systems have almost exclusively used Hill-based models (Zahalak, 1990). Criticisms of this approach have noted that Hill models may be too simple and fail to capture the essential elements of real muscle. However, the Hill approach has endured because accurate data for model parameters exist in the literature, motor function described by Hill models has often been verified experimentally, and simple models often provide insights hidden by overly complex models (Winters, 1995). The modeling task here is to provide a description of whole muscle performance to design an artificial system. As a result, a Hill-based model is an appropriate beginning. Various incarnations of the Hill model exist, but there are essentially three components: a parallel element, a series element, and a contractile element as shown with nomenclature in figure 2.1.

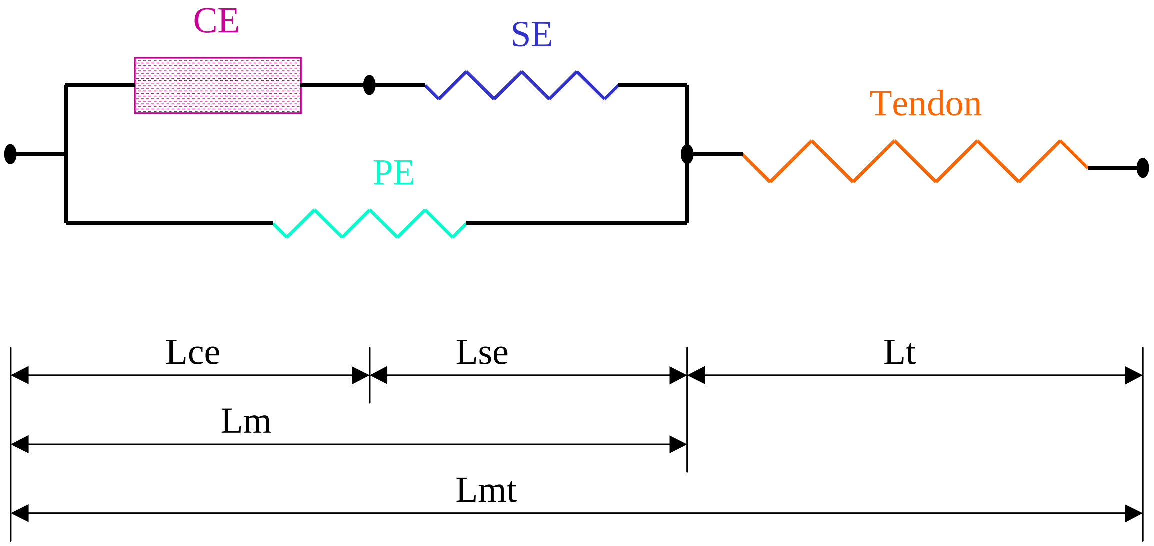

Figure 2.1: Schematic of the Hill muscle model (1938) identifying the relationship between the contractile element (CE), the series element (SE), the parallel element (PE) and the tendon. The nomenclature identifying the lengths of the various elements are also shown.

Static Properties of Biological Muscle

The mathematical models and data describing the static properties of the parallel, series, and contractile elements of the Hill muscle model are provided in the next three subsections. The results will be used to identify an acceptable range for the performance of an artificial muscle.

The parallel and series elements can be accurately modeled as Kelvin or "standard elements" (i.e. viscoelastic models), but rarely is the complexity of such a model worth the computational effort. Furthermore, experimentally derived parameters for such models are essentially non-existent. However, when the parallel and series elements are treated as simple elastic elements, experimental data is available in the literature for a variety of animal models. Of course, the contractile element is the dominant component of the Hill muscle model. Cook and Stark (1968) showed that this element could be treated as a force generator in parallel with a damping element. Under isometric or static conditions (zero contractile velocity), the output force can be described as a parabolic function of muscle length, and again, experimental data is available in the literature for a variety of animal models (e.g. references cited in tables 2.1, 2.2, and 2.3).

Parallel Element

Experimental evidence in the muscle physiology literature shows the parallel element to be a lightly damped, non-linear elastic element (Winters, 1990). This element is often ignored in skeletal muscle models because the force across the element is insignificant until the muscle is stretched beyond its usual physiological range (~1.2 times the muscle's resting length). When the damping is neglected, an exponential, power, or polynomial function can be used to approximate the non-linear spring. After examining the experimental literature, the form selected for use here is given by:

$$\frac{F_{pe}}{F_{m,o}} = k_1 \left(\frac{l_m}{l_{m,o}} \right)^{k_2} \tag{2.1}$$

where F_{pe} is the force across the parallel element, $F_{m,o}$ is the maximum isometric force when the muscle is at its resting length ($l_{m,o}$), and l_m is the instantaneous muscle length. Values for constants k_1 and k_2 can be found in the literature for many different vertebrates, including the frog, rat, cat, and human as listed in table 2.1. Other investigators have also used animal data to construct models of skeletal muscle that include parallel elements. The parallel element parameters from two of these biomechanic models are also listed in table 2.1. The resulting curves from the data in table 2.1 are plotted in figure 2.2. The figure shows that the force across the parallel element is relatively small, but rapidly increases as the muscle is stretched to lengths greater than resting.

Table 2.1: Parallel elastic element force versus elongation data from the literature.

Animal Model	k_1	k_2	$l_{m,o}$	$F_{m,o}$	
Rat[1]					
Frog[2]	0.0006	20.63	31.0 mm	0.67 N	r^2=0.95
Cat[3]	0.0301	9.16	31.9 mm	0.18 N	r^2=0.95
Human[4]	0.0037	10.43	215.9 mm	193.1 N	r^2=0.89
Skeletal Muscle Model[5]	0.0787	7.93			r^2=0.99
Human Model[6]	0.00001	24.59	61.0 mm	2430 N	r^2=0.99

[1] Bahler, 1968, states the "parallel elastic element may be neglected" when $l_m \leq 1.20 \cdot l_{m,o}$.

[2] Wilkie, 1956, data from his figure 2 with a range of $0.94 \cdot l_{m,o} \leq l_m \leq 1.39 \cdot l_{m,o}$. Frog *sartorius* muscle at 0 degrees C.

[3] McCrorey et al., 1966, data from his figure 10 with a range of $1.00 \cdot l_{m,o} \leq l_m \leq 1.40 \cdot l_{m,o}$. Cat *tenuissimus* muscle at 37 degrees C.

[4] Ralston et al., 1949, data from his figure 5 with a range of $1.05 \cdot l_{m,o} \leq l_m \leq 1.29 \cdot l_{m,o}$. Human *pectoralis major*, sternal portion at 37 degrees C. Measurements made *in-vivo* on amputees possessing cineplastic tunnels. *Caveats* include: (1) Results are not that of isolated muscle as the insertion tendon is necessarily included, (2) Ralston was unable to measure muscle length so data from a single cadaver (Wood et al., 1989) was used instead.

[5] Woittiez et al., 1984, used an exponential relationship to describe the passive elastic element from experiments on rats. His equation A-24 has been curve fit to the form presented here.

[6] Bobbert and van Ingen Schenau, 1990 also used an exponential relationship to describe the passive elastic element from experiments conducted by ter Keurs et al., 1978 on frogs.

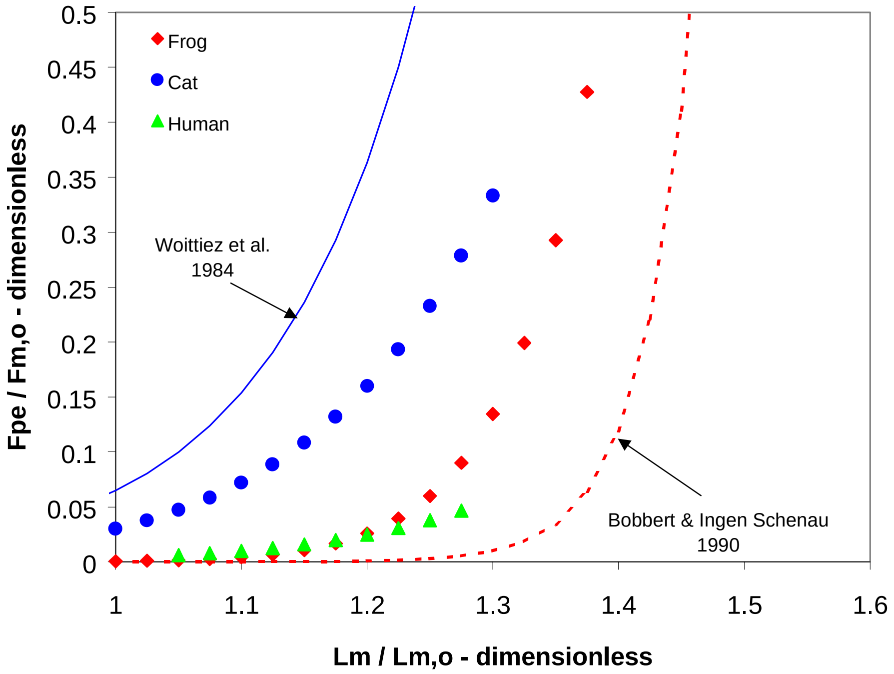

Figure 2.2: Parallel element force v. length relationship. Animal and model data from the muscle physiology and biomechanics literature as cited in table 2.1.

Series Elastic Element

The series element is the larger of the two “springs” in the Hill model. It is also generally accepted to be a lightly damped element; thus the damping can be neglected with little loss of accuracy (Winters, 1990). Again, a variety of mathematical functions could be used to model the non-linear spring. After examining the experimental literature, the form selected to relate force to deformation is given by:

$$\frac{\Delta l_{se}}{l_{m,o}} = k_3 \ln\left(\frac{F_m}{F_{m,o}}\right) + k_4 \qquad (2.2)$$

where Δl_{se} is the elongation of the series element and F_m is the instantaneous muscle force. Values for constants k_3 and k_4 are available in the literature for the frog, rat, and cat. These values are tabulated in table 2.2 and plotted in figure 2.3. As the force is increased across the element, it elongates. However, the magnitude of the elongation is small in comparison with the length of the resting muscle.

Table 2.2: Series elastic element force v. elongation data from the literature.

Animal Model	k_3	k_4	$l_{m,o}$	$F_{m,o}$	
Rat[1]	0.027	0.079	27.0 mm	0.29 N	r^2=0.98
Frog[2]	0.014	0.049	31.0 mm	0.67 N	r^2=0.99
Cat[3]	0.028	0.083	31.9 mm	0.18 N	r^2=0.98

[1] Bahler, 1967, data from his figure 6. Rat *gracilis anticus* muscle at 17.5 degrees C. Bahler, 1968, used a third order polynomial to describe this data.

[2] Wilkie, 1956, data from his figure 4. Frog *sartorius* muscle at 0 degrees C. Values for $l_{m,o}$ and $F_{m,o}$ were taken from Bahler's table 1 (1967) who attributed them to Wilkie, 1956.

[3] McCrorey et al., 1966, data from controlled-release experiments in his figure 6. Cat *tenuissimus* muscle at 37 degrees C.

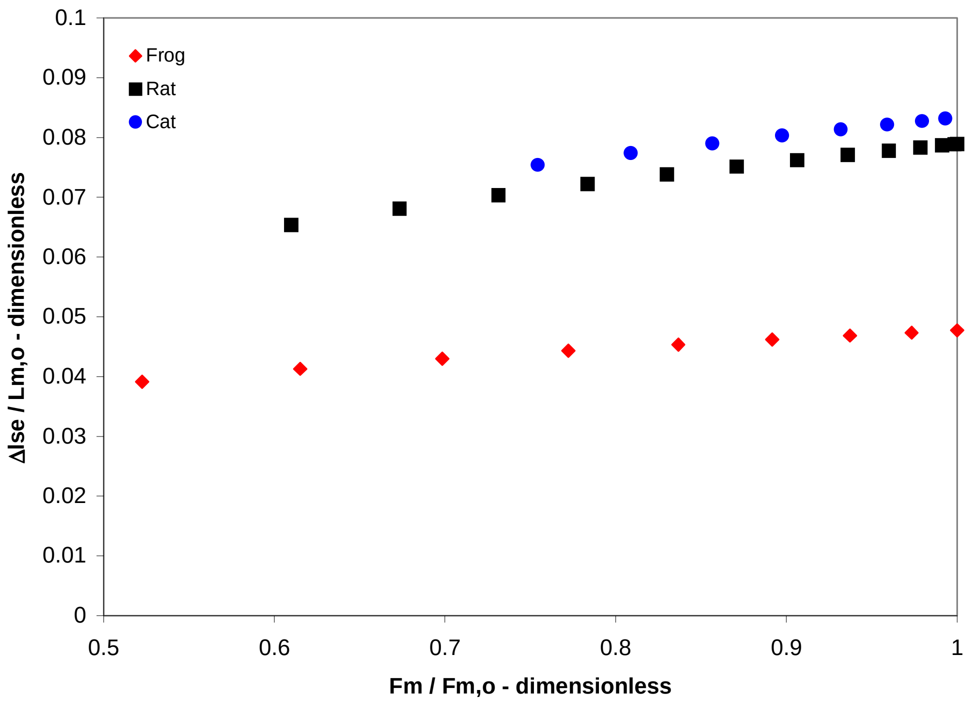

Figure 2.3: Series element force v. length relationship. Animal and model data from the muscle physiology and biomechanics literature as cited in table 2.2.

Contractile Element

The contractile element is the dominant component of the Hill muscle model. Cook and Stark (1968) showed that this element could be treated as a force generator in parallel with a damping element. Under isometric conditions (zero contractile velocity), the output force can be described as a parabolic function of muscle length by (Bahler, 1968):

$$\frac{F_{ce}}{F_{ce,o}} = k_5\left(\frac{l_{ce}}{l_{ce,o}}\right)^2 + k_6\left(\frac{l_{ce}}{l_{ce,o}}\right) + k_7 \tag{2.3}$$

where $F_{ce,o}$ is the maximum isometric force generated by the contractile element when it is at its "optimum length" ($l_{ce,o}$ =1.0). The instantaneous contractile element length is given by l_{ce} and the instantaneous contractile element force is given by F_{ce}. Values for the empirical constants k_5, k_6, and k_7 can again be found in the literature for the frog, rat, cat, and human, as well as the model proposed by Woittiez *et al.* (1984). These values are tabulated in table 2.3 and their resulting curves are plotted in figure 2.4. The biomechanic model of Bobbert and others (1986) uses the same values as Woittiez and hence is not plotted. Two other biomechanic models published in the literature (Bobbert and Ingen Schenau, 1990; Hoy et al., 1990) conform to the parabolic form but do not provide a mathematical equation. These two models are also plotted in figure 2.4 using digitized data from the original source. The results in figure 2.4 demonstrate the parabolic nature of the force-length relationship, but there is considerable variability between species and models. The human data has the largest change in slope and the narrowest "operating" length. The selected frog and rat muscles contract a larger amount by comparison, but the cat muscle was capable of generating force and lengths much greater than optimum ($l_{ce,o}$ =1.0). The model of Bobbert and others (1986) fit the data most closely, while the other models over predicted the force at shorter muscle lengths.

Table 2.3: Isometric force v. length data from the literature.

Animal Model	k_5	k_6	k_7	$l_{ce,o}$	$F_{ce,o}$	
Rat[1]	-4.50	8.95	-3.45	27.0 mm	0.29 N	$p \leq 0.001$
Frog[2]	-6.79	14.69	-6.88	31.0 mm	0.67 N	r^2=0.96
Cat[3]	-5.71	11.52	-4.81	31.9 mm	0.18 N	r^2=0.99
Human[4]	-13.43	28.23	-13.96	215.9 mm	193.1 N	r^2=0.75
Skeletal Muscle Model[5]	-6.25	12.50	-5.25	60.0 mm	3000 N	

[1] Bahler, 1968, his equation 16. Rat *gracilis anticus* muscle at 17.5 degrees C. Bahler's equation is valid over the range $0.7 \cdot l_{ce,o} \leq l_{ce} \leq 1.2 \cdot l_{ce,o}$. Bahler fitted his data using a "least mean square fit (significant to $p \leq 0.001$)."

[2] Wilkie, 1956, data from his figure 2 and 4. Frog *sartorius* muscle at 0 degrees C. For Wilkie's data, $0.68 \cdot l_{ce,o} \leq l_{ce} \leq 1.34 \cdot l_{ce,o}$ is valid.

[3] McCrorey et al., 1966, data from his figure 6 (controlled-release data) and 10. Cat *tenuissimus* muscle at 37 degrees C. For McCrorey's data, $0.73 \cdot l_{ce,o} \leq l_{ce} \leq 1.35 \cdot l_{ce,o}$ is valid.

[4] Ralston et al., 1949, data from his figure 5 using l_m and $l_{m,o}$ in place of l_{ce} and $l_{ce,o}$, respectively. Human *pectoralis major*, sternal portion at 37 degrees C. *Caveats* include: (1) results are not that of isolated muscle as the insertion tendon is necessarily included, (2) Ralston was unable to measure muscle length so data from from a single cadaver (Wood et al., 1989) was used instead, and (3) performance of residual amputee muscles may not be the same as those of intact individuals. Wilkie (1950) estimated the length change of Ralston's data to be three times less than normal and the peak isometric force to be five times less than normal. For Ralston's data, $0.82 \cdot l_{m,o} \leq l_m \leq 1.28 \cdot l_{m,o}$ is valid.

[5] Woittiez et al., 1984, his equation A-23. Constants for Woittiez model of skeletal muscle were chosen based on the work of Gordon et al., 1966, Hill 1953, and ter Keurs et al., 1978 (frog).

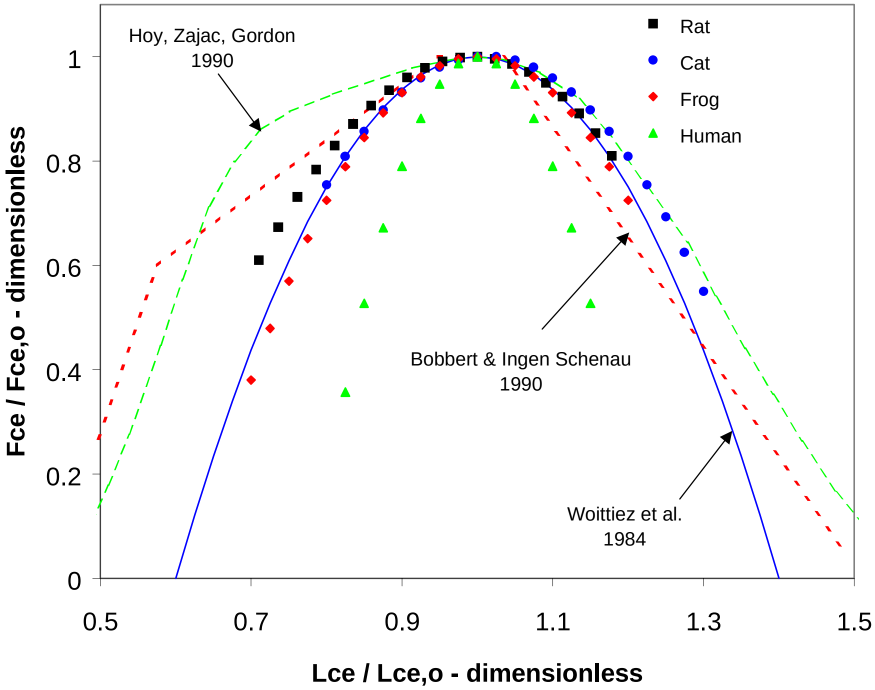

Figure 2.4: The dimensionless relationship between force and length under isometric conditions at maximal activation for the animal data and biomechanic models cited in the text and table 2.3.

Dynamic Properties of Biological Muscle

Under non-isometric conditions, the output of the contractile element is a function of both length and velocity for a given level of activation. It is also dependent on whether the muscle is shortening (concentric contraction) or lengthening (eccentric contraction) under load.

Concentric Contractions

It is well known that the output force of biological muscle drops significantly as concentric contraction velocities increase. The general form of this relationship is given by (Hill, 1938):

$$[F_m + a]\cdot[V + b] = [F(l_m) + a]\cdot b \tag{2.4}$$

where F_m is the instantaneous muscle force, V is the instantaneous muscle velocity, and $F(l_m)$ is the isometric muscle force at the instantaneous muscle length (l_m). The constants a and b are empirically determined and depend not only on the species of interest, but also on the type of muscle fiber within a species.

Values from the muscle physiology literature for the parameters in equation (2.4) are given in table 2.4 for the frog, rat, cat, and human. Furthermore, values from four published biomechanic models are also tabulated. Examination of the parameters in table 2.4 clearly indicates there are a wide range of possible values. Figure 2.5 plots the resulting curves when the muscle's instantaneous length is equal to its resting length ($l_{m,o}$). The human muscle generated higher forces for a particular velocity than the rat, frog, or cat respectively. The figure shows significant variation across animals as well as variation among published muscle models purporting to portray the performance of human skeletal muscle.

Table 2.4: Force v. velocity data from the muscle physiology literature for use in equation (2.4). See text for explanation of parameters.

Animal Model	$a/F_{m,o}$ - none	$F(l_{m,o})$ - N	$b/V_{m,o}$ - none	$V_{m,o}$ - mm/s
Rat[1]	0.356	4.30	0.38	144
Frog[2]	0.27	0.67	0.28	42
Cat[3]	0.27	0.18	0.30	191
Human[4]	0.81	200	0.81	1115
Skeletal Muscle Model[5]	0.224		0.224	
Human[6]	0.41	3000	0.39	756
Human[7]	0.41	2430	0.41	780
Human[8]	0.12		0.12	

[1] Wells, 1965, his table 1. Rat *tibialis anterior* muscle at 38 degrees C.
[2] Abbott and Wilkie, 1953, their figure 5. Frog *sartorius* muscle at 0 degrees C.
[3] McCrorey et al., 1966, their figure 1. Cat *tenuissimus* muscle at 37 degrees C.
[4] Ralston et al., 1949, their figure 1; but see also Wilkie, 1953. Human *pectoralis major in-vivo*, sternal portion at 37 degrees C.
[5] Woittiez et al., 1984, their equations A-22 and B-8. Model of generic skeletal muscle. Woittiez's dimensionless model did not require the specification of $F(l_{m,o})$ or $V_{m,o}$.
[6] Bobbert et al., 1986. Model of human *triceps surae*.
[7] Bobbert and van Ingen Schenau, 1990. Model of human *triceps surae*.
[8] Hof and van den Berg, 1981b. Model of human *triceps surae*. Hof and ven den Berg's model also did not require the specification of $F(l_{m,o})$ or $V_{m,o}$.

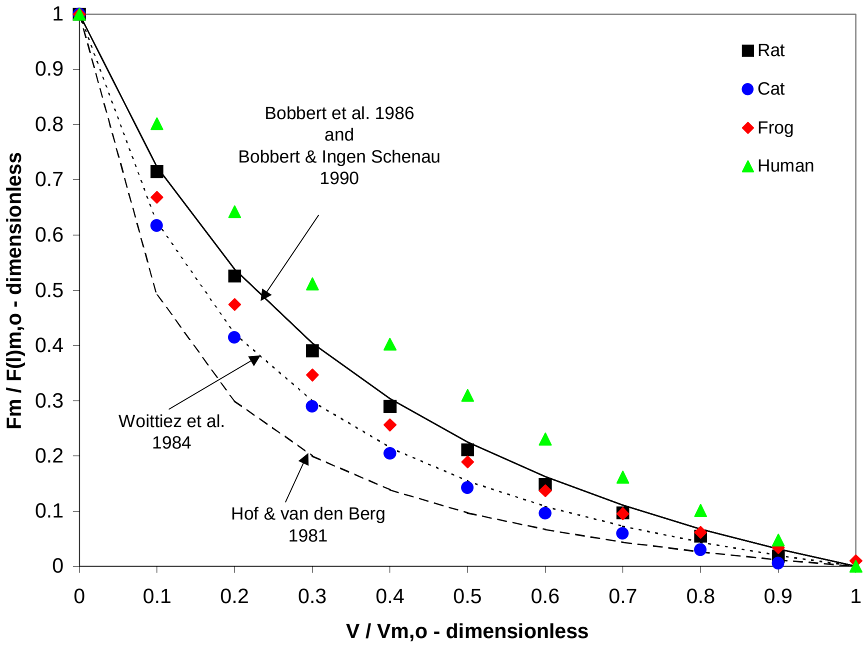

Figure 2.5: Predicted output force over a muscle's concentric (shortening) velocity range (positive values by convention) for four different animals and four published biomechanic models.

Eccentric Contractions

The majority of research conducted on the contractile element of muscle has involved concentric (i.e. shortening under load) contractions. Obviously, both biological and artificial muscles perform eccentric (i.e. lengthening under load) contractions, but unfortunately, there exists significant variation in output force for biological muscle under these conditions ($V / V_{m,o} \leq 0$).

Most biomechanical models assume an asymptotic relationship between force and increasing lengthening velocities. These models modify the "classic" Hill equation (eq. 2.4) to obtain an "inverted Hill's" model to describe lengthening muscle behavior. Saturation values for these models are typically assumed to be 1.3 $F_{m,o}$ (e.g. Hatze, 1981; Winters and Stark, 1985); however, values ranging from as low as 1.2 $F_{m,o}$ (Hof and van den Berg, 1981a) to as high as 1.8 $F_{m,o}$ (Lehman, 1990) have been used. As shown in figure 2.6, experimental evidence from the cat soleus muscle (Joyce et al., 1969) is perhaps closer to a saturation value of 1.3. In all cases, the force increases with increasing velocity.

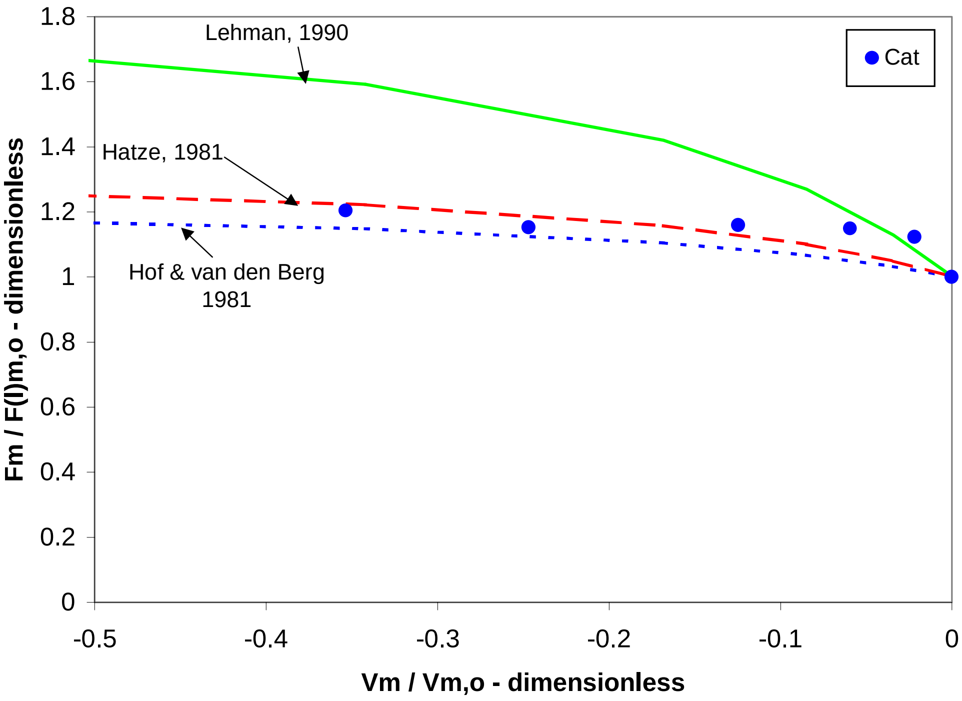

Figure 2.6: Predicted output force over a muscle's eccentric velocity range (negative values by convention) for the cat soleus and three published biomechanic models.

In-Vivo Experiments

Research to expose the properties of biological muscle is typically conducted using *in-vitro*, isotonic preparations. However, while most muscle function in nature is not isotonic, few *in-vivo* experiments have been conducted on mammals due to experimental difficulties. Of the few, the results of two such experiments raise interesting questions regarding *in-vivo* muscle performance.

Monti and others (1999) conducted experiments on the rat soleus muscle *in-situ* whose results are shown in figure 2.7. Following a maximal isometric tetanus lasting 375 msec, the muscle was released in order to obtain a constant velocity similar in magnitude to that occurring in locomotion. Approximately 50 msec was required to accelerated from zero velocity (point a on figure 2.7) until the desired contraction velocity was reached (point b on figure 2.7). The desired isokinetic velocity was then held for a further 100 msec (point c on figure 2.7). When compared with isotonic experiments conducted later on the same muscle, considerably higher forces were obtained during the transient period (between points a and b on figure 2.7). Monti's work demonstrates that significantly higher forces are produced during transient velocity periods than predicted by steady state isotonic experiments. The results imply higher forces may actually be produced during locomotion than those predicted from models founded on isotonic experimental data.

Gregor and others (1988) measured the performance of the cat soleus muscle during treadmill locomotion (constant gait velocity) and compared the results with isotonic experiments on the same muscle. Force and velocity curves were constructed from an average of five steps at 2.2 m/s. The results from one experiment are shown in figure 2.7 and again demonstrate higher forces than those observed during isotonic experiments. Gregor's results on additional cats exhibited significant variability and are not shown.

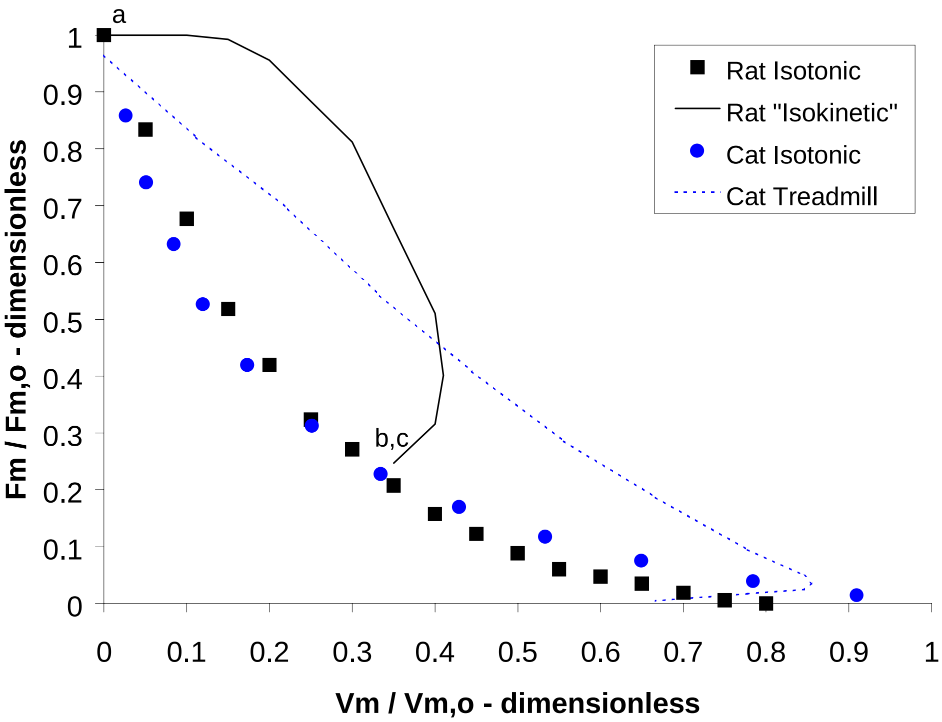

Figure 2.7: Force-velocity curves from *in-situ* rat soleus muscle (Monti et al., 1999, their figure 6) and *in-vivo* cat soleus muscle (Gregor et al., 1988, their figure 3). The isotonic experiments generated lower forces than with alternative velocity profiles.

These two experiments indicate higher forces can be realized when testing occurs outside the isotonic paradigm. Unfortunately, no modeling work has been conducted in an effort to understand or explain these results and additional work is warranted. In conclusion, the Hill model accurately predicts the forces produced during concentric, isotonic contractions, but may be insufficient otherwise.

Design Requirements for Artificial Muscle

Given the significant variability of biological muscle, specifying a range for the desired artificial muscle performance is reasonable. Furthermore, to simplify the requirements, both the parallel and series elements will be neglected for several reasons. As will be shown in chapter three, the McKibben actuator will be used as the contractile element of the artificial muscle. The physical structure of the McKibben actuator prevents elongation past its resting length. As shown above, this is precisely the point at which the parallel element properties gain prominence and hence can be neglected without loss of accuracy.

The series element will also be neglected. One application for this research is the development of a powered, prosthetic limb for trans-tibia amputees. The artificial musclo-tendon system to be emulated in this case is the *triceps surae* and includes both the *gastrocnemius* and *soleus* muscles and the *Achilles* tendon. In this case, the ratio of tendon length to muscle length is approximately 10:1 (Alexander and Vernon, 1975, Bouaziz et al., 1975; Rack et al., 1983; Yamaguchi et al., 1990). For a maximal contraction, the series element might elongate as much as eight percent of the muscle length (as shown in figure 2.3), but only 0.8 percent of the muscle plus tendon length. As shown by Zajac (1989), this results in negligible energy storage in the series element and can be safely neglected.

The contractile element can be accurately modeled as a parabolic function (equation 2.3) by specifying three constants. However, due to the wide variance in the force-length relationship, specifying exact parameters for the constants in equation (2.3) would certainly be controversial. However, by specifying a range, we can identify performance that would be acceptable. From the results in table 2.3 and figure 2.4, a range is proposed such that:

$$-4.5 \le k_5 \le -13.5 \qquad (2.5a)$$

$$9.0 \le k_6 \le 28.2 \qquad (2.5b)$$

$$-3.5 \le k_7 \le -14.0 \qquad (2.5c).$$

Similarly, the force-velocity relationship also exhibits wide variance. From the results in figure 2.5, a reasonable criteria for an artificial muscle is one that satisfies:

$$0.12 \le a/F_{m,o} \le 0.41 \qquad (2.5d)$$

$$0.12 \le b/V_{m,o} \le 0.41 \qquad (2.5e)$$

where $F_{m,o}$ is the maximum isometric force when the muscle is at its resting length ($l_{m,o}$) and $V_{m,o}$ is the maximum concentric velocity at the resting length and are used in equation (2.4). Furthermore, until additional research is done on eccentric muscle properties, it appears reasonable to accept an inverted Hill's model within a range of parameters described by equations 2.5d and 2.5e with a saturation value of 1.3 $F_{m,o}$ for eccentric contractions (i.e. $V/V_{m,o} \le 0$).

Summary

Using a parabolic model of muscle for the force-length properties (equation 2.3) and the Hill hyperbolic model for the force-velocity properties (equation 2.4) yields a generic model for skeletal muscle. The results of this model, plotted in dimensionless format, are shown in figure 2.8 (k_5 =-6.9, k_6 =13.8, k_7 =-5.9, $a / F_{m,o}$ =0.28, and $b / V_{m,o}$ =0.28). This model is computational simplified by neglecting both the parallel and series elastic elements. Incorporation of the parallel element is only necessary if the muscle will be stretched appreciatively beyond its resting length and incorporation of the series elastic element is only necessary when the muscle length is large with respect to the tendon length.

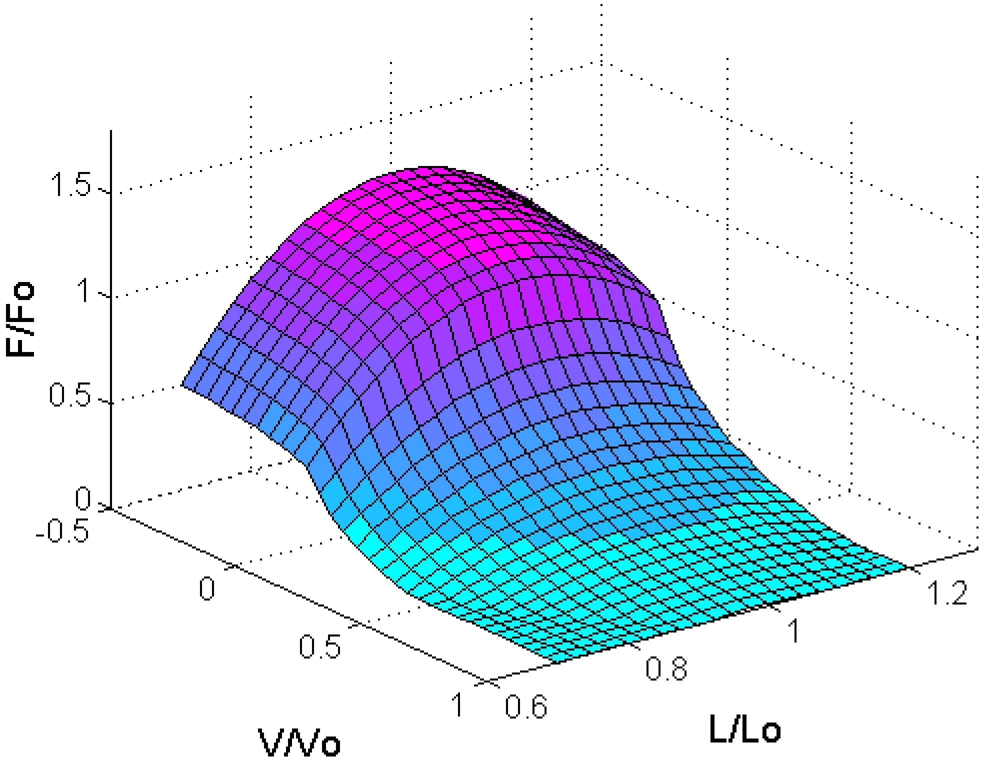

Figure 2.8: Dimensionless force-length-velocity plot of skeletal muscle.

Chapter 3: McKibben Actuators

A number of investigators have described the development of an “artificial muscle.” Some investigators have proposed the use of commercially available actuators to serve as artificial muscles (e.g. Yoda and Shita, 1994; Cocatre-Zilgien et al., 1996). Others have suggested more novel approaches such as shape-memory alloys (Mills, 1993), electro-reactive gels (Mitwalli et al., 1997), and ionic polymer-metal composites (Mojarrad and Shahinpoor, 1997). All of these approaches for an artificial muscle have one thing in common with biological muscle: when the actuator is activated, they contract. However, when considering the force produced as a function of length, velocity, and activation, all of these approaches fall far short of performing like real muscle.

Description and History

Our approach has used a pneumatic actuator invented by R. H. Gaylord in the 1950’s (Gaylord, 1958). Gaylord’s original applications included a door opening arrangement and an industrial hoist, but J. L. McKibben adapted the actuator for use by polio patients as an orthotic appliance (Murray, 1959). By the early 1960’s, the actuator and orthotic splint was sufficiently mature to be used in clinical trials (Nickel et al., 1963). Powered by compressed gas, the actuator is made from an inflatable inner bladder sheathed with a double helical weave which contracts lengthwise when expanded radially (see figure 3.1). The McKibben device can be considered a biorobotic actuator because it comes reasonably close to mimicking the force-length properties of skeletal muscle (Chou and Hannaford, 1996).

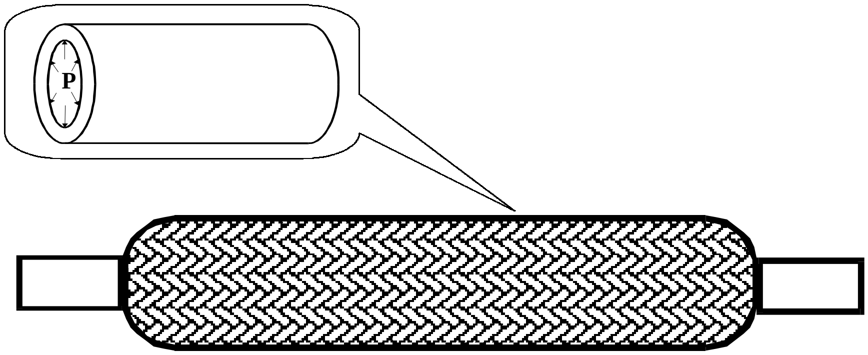

Figure 3.1: McKibben actuator with exterior braid and inner elastic bladder.

The actuators used by Chou and Hannaford (1996) were constructed such that the bladder length was slightly less than the braid length. This construction technique provides an equivalent to a series elastic element as the actuator can be passively (i.e. no activation pressure) elongated. However, when pressure is applied with the actuator at its natural resting length (equal to the bladder length), the actuator first elongates to the maximum braid length, and then begins to shorten. As this initial elongation is decidedly non-muscle-like, the actuators used here are all constructed with equal bladder and braid lengths.

Modeling Approaches

Our interest in a mathematical model of the McKibben actuator was to better understand the design parameters in order to improve desirable characteristics (e.g. output force v. input pressure) while minimizing undesirable characteristics (e.g. hysteresis and fatigue failure). Previous efforts to model the McKibben actuator fall into several categories:

(a) empirical models (Gavrilovic and Maric, 1969; Medrano-Cerda et al., 1995),
(b) models based on geometry (Chou and Hannaford, 1996; Gaylord, 1958; Schulte, 1961; Tondu et al., 1994; Paynter, 1996), and
(c) models that include material properties (Chou and Hannaford, 1996; Schulte, 1961).

A few investigators have plotted their model predictions versus experimental results, but no theoretical model has achieved satisfactory results. As a result, most investigators developing applications for this actuator have relied on the inaccurate, but simple, geometric models. This chapter will present an improved model that includes the material properties of the inner bladder constrained by braid kinematics and will compare the model predictions with experimental results.

Theoretical Model

Using conservation of energy and assuming the actuator maintains dV/dP equal to zero, reasonable for actuators built with stiff braid fibers that are always in contact with the inner bladder, the tensile force produced can be calculated from:

$$F = P\frac{dV}{dL} - V_b\frac{dW}{dL} - F_f \tag{3.1}$$

where P is the input actuation pressure, dV is the change in the actuator's interior volume, dL is the change in the actuator's length, V_b is the volume occupied by the bladder, and dW is the change in strain energy density (also known as the change in stored energy per unit volume). F_f describes the lumped effects of friction arising from sources such as contact between the braid and the bladder and between the fibers of the braid itself. Neglecting the second and third terms on the right hand side of equation (3.1) and assuming the actuator maintains the form of a right circular cylinder with an infinitesimally thin bladder yields known solutions (Chou and Hannaford, 1996; Gaylord, 1958; Medrano-Cerda et al., 1995; Schulte, 1961).

The solution to the second term on the right side of equation (3.1) is based on a non-linear materials model developed by Mooney and Rivlin in the 1940's and 1950's (e.g. Treloar, 1958). Their well-known research proposed a relationship between stress ($\overline{\sigma}$) and strain ($\overline{\varepsilon}$) given by $\overline{\sigma} = dW/d\overline{\varepsilon}$ where W is the strain energy density function. Using the assumptions of initial isotropy and incompressibility, W can be described as a function of two strain invariants (I_1 and I_2):

$$W = \sum_{i=0,\, j=0}^{\infty} C_{ij} (I_1 - 3)^i (I_2 - 3)^j \tag{3.2}$$

where C_{ij} are empirical constants (Treloar, 1958). Only two Mooney-Rivlin constants (C_{10} =118.4 kPa and C_{01} =105.7 kPa) were necessary for accurate results with the natural latex rubber bladder, however, other materials may require additional constants. For the case of the McKibben actuator, the experimental methods required to determine these constants are dramatically simplified because the McKibben actuator's strain invariants, constrained by braid kinematics, are nearly the same as the strain invariants for uniaxial tension (Klute and Hannaford, 1998a). This fortuitous relationship eliminates the need for multi-axial testing that would otherwise be necessary.

Solving equation (3.1) using the non-linear Mooney-Rivlin materials model results in a McKibben actuator model whose structure is allowed to deform as well as store elastic energy in a non-linear fashion (Klute and Hannaford, 1998b). This model is given by:

$$\begin{aligned} F_{\mathrm{mr}} = {} & P\left\{ \frac{3(\lambda_1 L_o)^2 - B^2}{4N^2\pi} \right\} \\ & - V_b \left\{ \begin{aligned} & \frac{1}{2L_o^3\lambda_1^3} \Bigg\{ 4(C_{10} + C_{01}) L_o^2 \left(-1 + \lambda_1^4\right) + \frac{4L_o^6 \left(-1 + \lambda_1\right)\lambda_1^2 \left(1 + \lambda_1\right)\left(C_{10} + C_{01}\lambda_1^2\right)}{\left[-4N^2\pi^2 R_o^2 + L_o^2\left(-1 + \lambda_1^2\right)\right]^2} \\ & - \frac{4L_o^4\left(C_{10} + C_{01}\lambda_1^4\right)}{-4N^2\pi^2 R_o^2 + L_o^2\left(-1 + \lambda_1^2\right)} - \frac{L_o^4\lambda_1^4\left[C_{10} + C_{01}\left(-1 + 2\lambda_1^2\right)\right]}{N^2\pi^2 R_o^2} \Bigg\} \end{aligned} \right\} \end{aligned} \tag{3.3}$$

where F_{mr} is the predicted force, and parameters N, L_o, B, and R_o are shown in figure 3.2 and given in table 3.1. Bladder thickness is denoted by t_o and is used in the bladder volume calculation. λ_1 refers to the actuator's longitudinal stretch ratio and is given by $\lambda_1 = L_i / L_o$, where L_i is the actuator's instantaneous length and L_o is the original, resting state length.

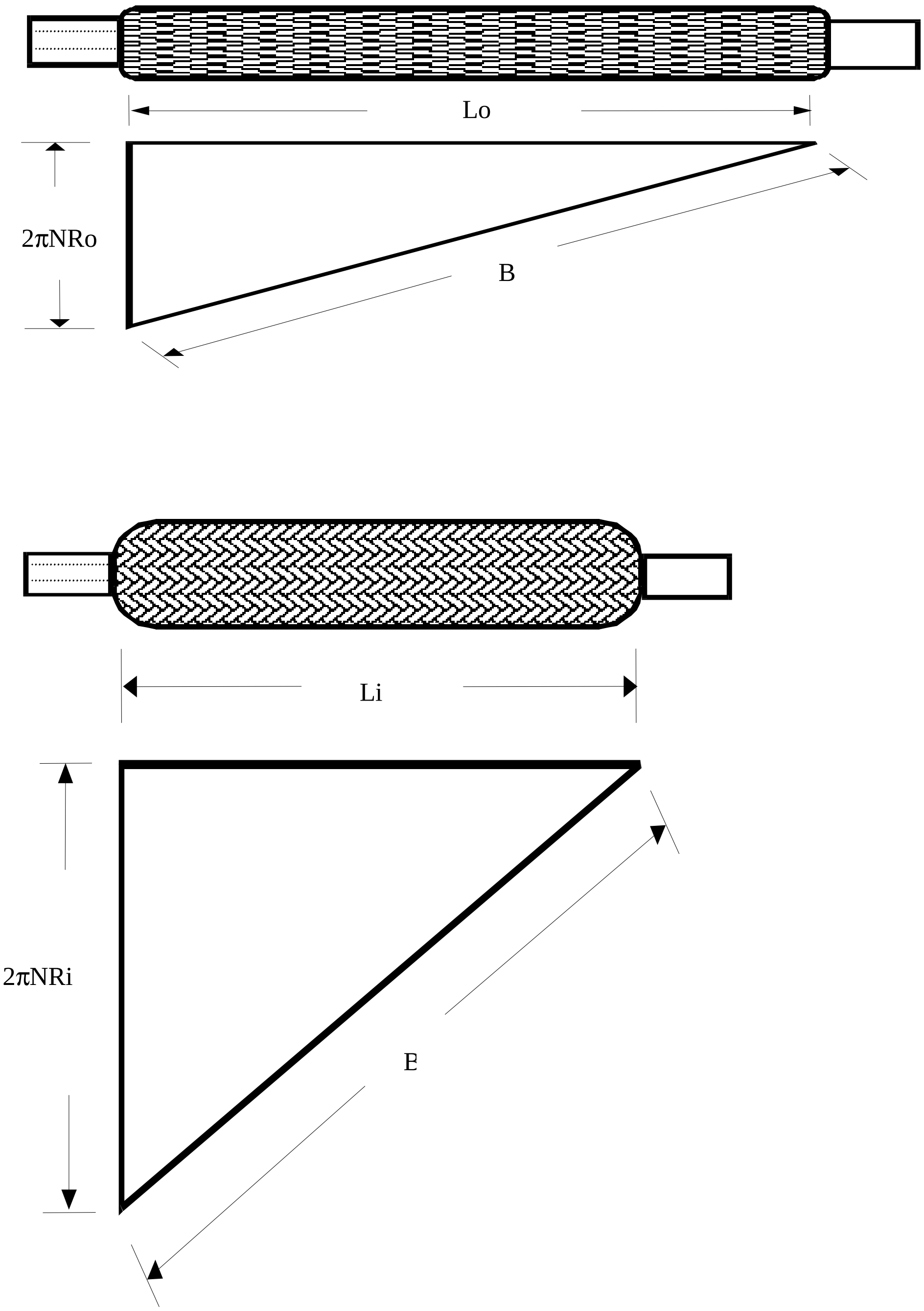

(3.2a)

(3.2b)

Figure 3.2: McKibben actuators are fabricated from two principle components: an inflatable inner bladder made of a rubber material and an exterior braided shell wound in a double helix. At ambient pressure, the actuator is at its resting length (figure 3.2a). As pressure increases, the actuator contracts proportionally until it reaches its maximally contracted state at maximum pressure (figure 3.2b). The amount of contraction is described by the actuator's longitudinal stretch ratio given by $\lambda_1 = L_i / L_o$ where L is the actuator's length, and subscript i refers to the instantaneous dimension and the subscript o refers to the original, resting state dimension.

Table 3.1: Model constants for three different sized McKibben actuators. The braid for each actuator was constructed from a polyester thread and the bladder of each was made of natural latex rubber.

General Dimensions		Braid Dimensions			Bladder Dimensions		Friction Parameters	
Braid	Bladder	N	L_o	B	R_o	t_o	m	b
inches[1]	inches[2]	turns	mm	mm	mm	mm	N/bar	N
1-1/4	1/2 x 3/32	1.5	264.0	277.1	8.7	2.4	56.9	109.8
3/4	3/8 x 1/16	1.5	181.0	190.6	6.4	1.6	28.0	-38.2
1/2	5/32 x 3/64	1.7	126.0	130.5	3.2	1.2	3.6	28.3

[1] The braid is described by the manufacturer's designation for nominal diameter in inches (i.e. 1-1/4 = 1.25 in). Alpha Wire Corp., Elizabeth, New Jersey, U.S.A.

[2] The bladder is described by the internal diameter (inches) and the wall thickness (inches) following the convention typical of most manufacturers.

Experimental Methods

To test the predictive value of the model, we conducted a series of experiments on three different sized McKibben actuators. We used an axial-torsional Bionix™ testing instrument (MTS Systems Corp., Minnesota, U.S.A.) to apply uniaxial displacements while measuring the output force at specific input pressures. To ensure maintenance of a constant pressure, we attached a pressure vessel whose volume was significantly larger than the actuator (4000:1 minimum volume ratio). Out of consideration for typical industrial pneumatic supplies, we limited the maximum input pressure to 5 bar. To minimize tip-effects at the actuator's ends, the three different sized actuators (see table 3.1) were constructed such that their lengths to diameter ratios were at least 14. A schematic of the test set-up is shown in figure 3.3.

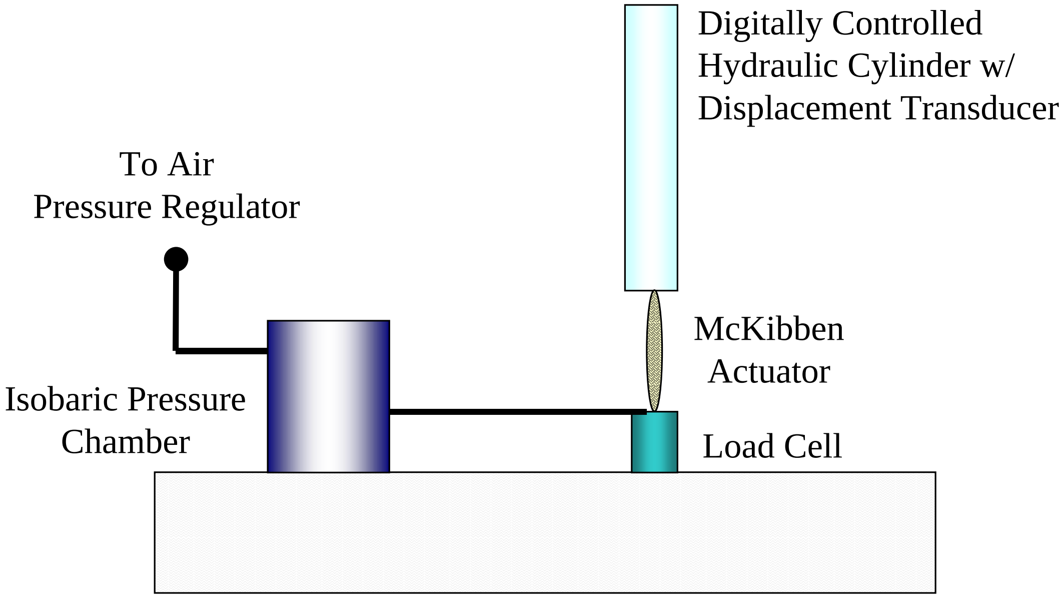

Figure 3.3: Experimental set-up for measuring the force-length properties of McKibben actuators at various pressures. The isobaric pressure chamber ensures pressure within the actuator is independent of its length (i.e. volume).

Experimental Results and Discussion

The results comparing the experimental measurements with the model predictions are shown in figure 3.4 for the largest of the three actuators tested (1-1/4 in. nominal braid diameter). Schulte's model ($F_{schulte}$), based strictly on braid geometry and does not account for bladder thickness or material, over-predicted the actual force by approximately 500 N over the entire contraction range at 5 bar. The model incorporating bladder geometry and Mooney-Rivlin material properties (F_{mr} , equation 3.3) also over-predicted the actual force, but by only 250 N at 5 bar. Proportional results for both models were also obtained at 2, 3, and 4 bar, but are not shown. Similar results were obtained for the smaller two actuators but are also not shown.

Accounting for the non-linear properties of the bladder yields a significantly more accurate model. However, a discrepancy remains that is likely the result of friction between the bladder and the braid, as well as between the fibers of the braid itself.

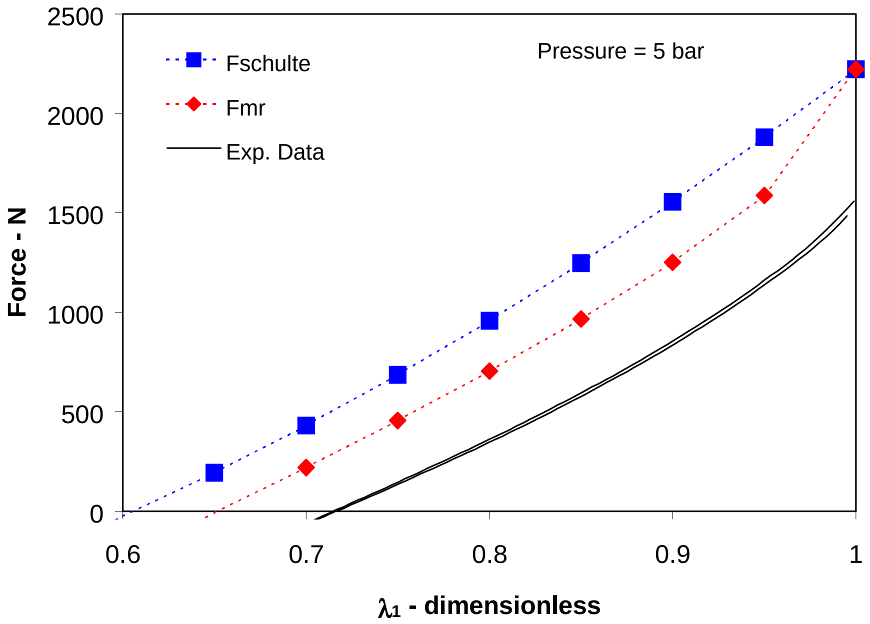

Figure 3.4: Model predictions versus experimental results are presented for the largest of the three actuators tested (nominal braid diameter of 1-1/4). $F_{schulte}$ refers to the model developed by Schulte (1961) which does not account for bladder material. F_{mr} refers to our model which incorporates both bladder geometry and Mooney-Rivlin material properties.

Estimation of Frictional Effects

The third term on the right of equation (3.1) represents these frictional losses which are a function of (1) braid material, (2) bladder material, (3) pressure, and (4) actuator length. In lieu of a model that incorporates a function for each of these, we have taken the intermediate step of lumping all of these effects into a single parameter (F_f) as a simple function of pressure. Analysis of the experimental data and theory predictions (F_{mr} , equation 3.3) suggests a linear form given by:

$$F_f = mP + b \tag{3.4}$$

where m and b are empirically determined constants (see table 3.1 for values of three different sized actuators).

The actuator model, which now includes the geometry of the braid and bladder, the material properties of the bladder, and a term for frictional effects (all three terms of equation 3.1) is given by:

$$F = F_{\mathrm{mr}} - F_f \tag{3.5}$$

A comparison of this model versus experimental results for the largest actuator (nominal braid diameter of 1-1/4 in.) is presented in figure 3.5. The figure shows a reasonably close fit for each of the four activation pressures tested. Similar results were obtained for the two smaller actuators (nominal braid diameters of ¾ and 1/2) but are not shown.

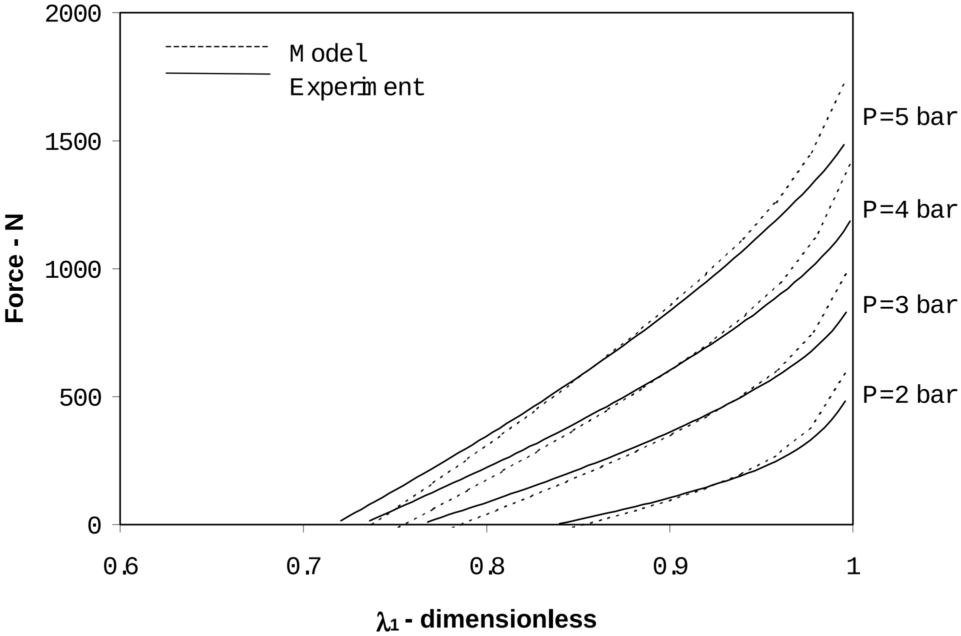

Figure 3.5: Model predictions versus experimental results are presented for the largest of the three actuators tested (nominal braid diameter of 1-1/4 in.) at pressures ranging from 2 to 5 bar. The model incorporates geometric properties of the exterior braid, geometric and material properties of the inner bladder, and empirically determined frictional effects.

Static Properties Compared with Biological Muscle

Advances in the theoretical modeling of the McKibben actuator have been presented with the objective of identifying the dependence of performance on the properties of both the exterior braided shell and the inner bladder. By modeling the inner bladder as an incompressible Mooney-Rivlin material and estimating frictional losses, we have been able to improve predictions of the actual output forces as a function of length and pressure. However, to eliminate the need to empirically determine frictional losses and any other factors not considered, further work is required.

The properties and performance of the McKibben actuator can now be compared with biological muscle. As presented in chapter 2, the muscle physiology literature contains numerous reports identifying the relationship between force and length during isometric contractions (constant length) when the activation is maximal. Figure 3.6 presents this relationship in a dimensionless form for the McKibben actuator as well as rat, frog, cat, and human muscles (using the parallel, series, and contractile elements as specified in chapter two). Along the ordinate, the instantaneous output force at any length is normalized by the output force at the muscle’s *in-vivo* resting length, while along the abscissa, the instantaneous length is normalized by the *in-vivo* resting length. As is readily observable, the passive properties of muscle allow it to stretch far beyond its *in-vivo* resting length, while the McKibben actuator cannot. However, for lengths less than resting, the McKibben actuator provides a first order approximation of biological muscle and meets the requirements specified in equations (2.5a, b, and c).

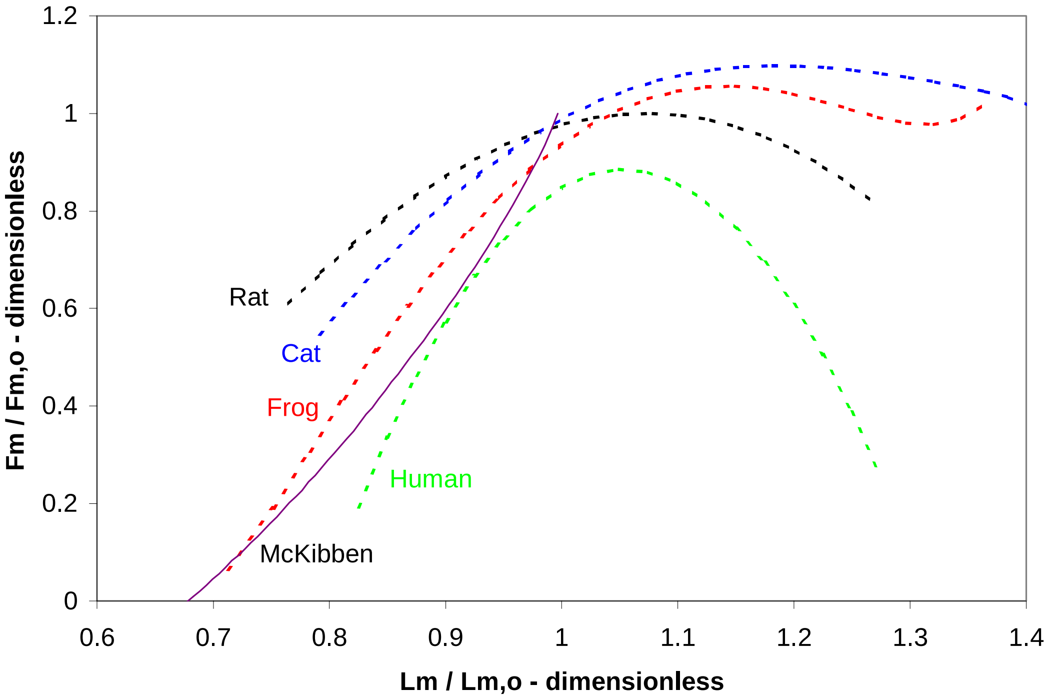

Figure 3.6: The dimensionless relationship between force and length under isometric conditions at maximal activation for various animals as well as a McKibben actuator pressurized to 5 bar.

As noted at the beginning of this chapter, it is possible to construct actuators such that the bladder length is shorter than the braid length as opposed to the equal lengths used here. In this case, where the resting length is equal to the braid length, the McKibben curve in figure 3.6 would be offset to the right. This would provide contraction forces at $L_m / L_{m,o}$ greater than one as well as provide an equivalent series elastic element. However, because this construction technique also results in an actuator that first elongates and then contracts during activation, it is not used here.

Dynamic Properties of McKibben Actuators

To measure the force-velocity properties of the McKibben actuator, we again conducted a series of experiments with the axial-torsional Bionix™ (MTS Systems Corp., Minnesota, U.S.A.) tensile testing instrument using the same test set-up. Actuators of all three sizes (see table 3.1) were constructed and tested. Each experiment measured the force output at a constant pressure over the contraction range at various velocities. One end of the actuator was rigidly attached to the load cell while the other end was moved in response to the instrument's digital controller. Step velocity profiles were applied such that one end of the actuator was rapidly accelerated and held to a constant velocity until the end of the actuator's working length was reached. Input step velocity profiles tested included 1, 10, 25, 50, 100, 150, 200, 250, and 300 mm/s for concentric contractions and 1, 10, 25, 50, 100, and 150 mm/s for eccentric contractions. Up to 500 mm/s is possible; however, instantaneous fluctuations in velocity of 15 percent were measured during trails at 500 mm/s. The magnitude of these fluctuations decreased at lower velocities, and was less than 9 percent at 300 mm/s and 6 percent at 200 mm/sec. This anomaly is thought to arise from the hydraulic pump.

Experimental Results

The experimentally measured output force of a single McKibben actuator, plotted as a function of both length and velocity, is shown in figure 3.7. The results shown are from an actuator whose nominal braid diameter was ¾ inch and constructed with a natural latex bladder. The actuator pressure was 5 bar and the original, resting state length of the actuator was 180 mm. The output force is clearly a function of length, but not of velocity. Similar results were obtained at lower pressures and with the other two sized actuators, but are not shown.

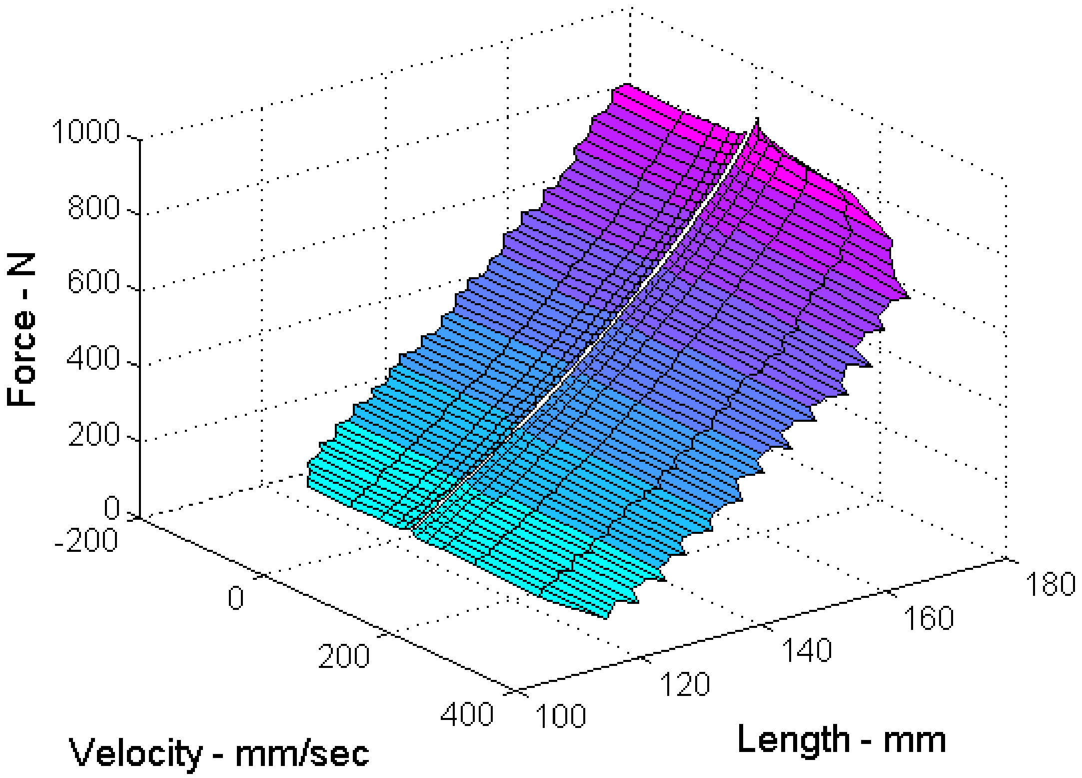

Figure 3.7: McKibben actuator force (experimental data) plotted as a function of both length and velocity. Ripples at higher velocities are artifacts of the hydraulic pump used in the testing instrument. The actuator was constructed with a nominal braid diameter of ¾ in. (see table 3.1), a resting state length of 180 mm, and tested at an actuation pressure of 5 bar.

By placing multiple actuators in parallel, it is possible to generate larger output forces in proportion to the number of actuators. Using the same methods outlined above, additional experiments were conducted with two McKibben actuators (3/4 in. nominal braid diameter) placed in a parallel configuration. The concentric and eccentric contraction velocities were 1, 10, 25, 50, 100, 150, 200, 250, and 300 mm/s. To achieve a larger contraction range, longer actuators were constructed such that the resting state length was increased to 250 mm. Actuation pressures were 2, 3, 4, and 5 bar.

The results of this test are shown in figure 3.8. The output force is a function of length and not velocity, but its magnitude is twice that of a single actuator. Similar results were obtained at each of the tested actuation pressures but are not shown.

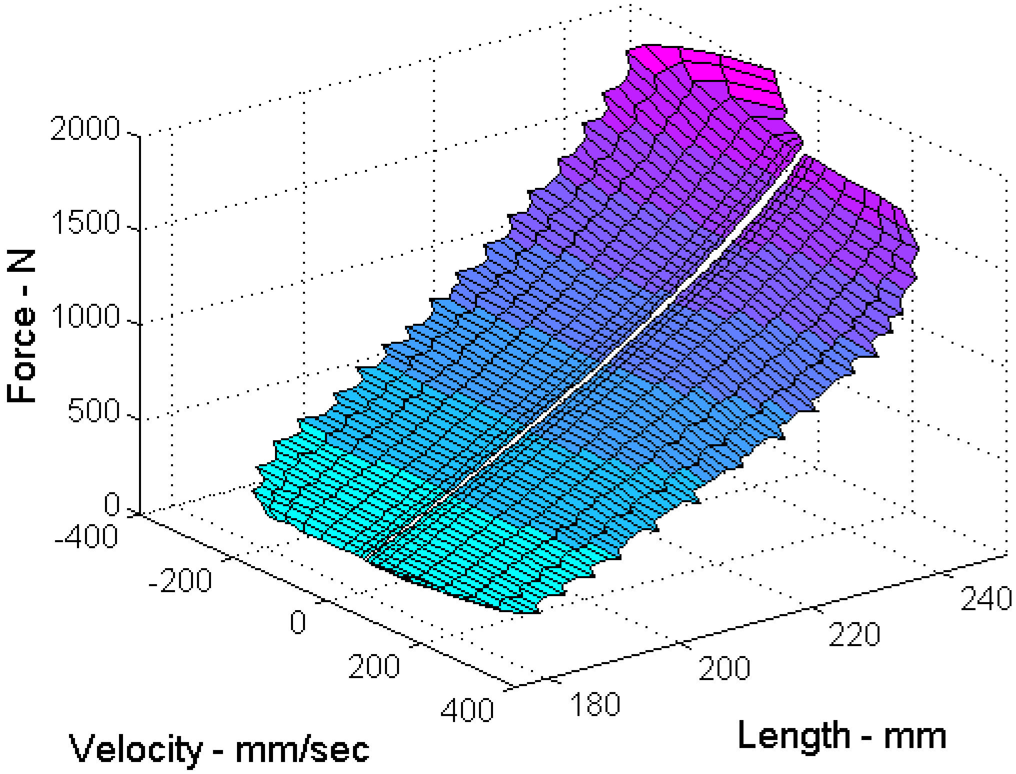

Figure 3.8: Experimental data from two McKibben actuators operating in parallel and plotted as a function of both length and velocity. The original resting state length for the pair of actuators was 250 mm and the actuation pressure was 5 bar.

Dynamic Properties Compared with Biological Muscle

To compare with the "enveloped" properties of biological muscle (developed in chapter two), a portion of this data is re-plotted as force versus velocity at a constant length in figure 3.9. In the muscle physiology literature, it is common to select the muscle's *in-vivo* resting length as this constant value; however, our test set-up requires a few milliseconds to reach the target velocity. Therefore, in figure 3.9, the experimental data and biological model values (F_{m} and V_{m}) were taken when the actuator's length (l_{m}) was slightly shorter than the resting length (such that $l_{\mathrm{m}} = 0.96\, l_{\mathrm{m,\,o}}$). The maximum force of the McKibben actuator ($F_{\mathrm{m,\,o}}$) was 734 N under near static conditions (1 mm/s), and decreased with increasing velocity. At 300 mm/s, the output force was 690 N, a decrease of only 6 percent.

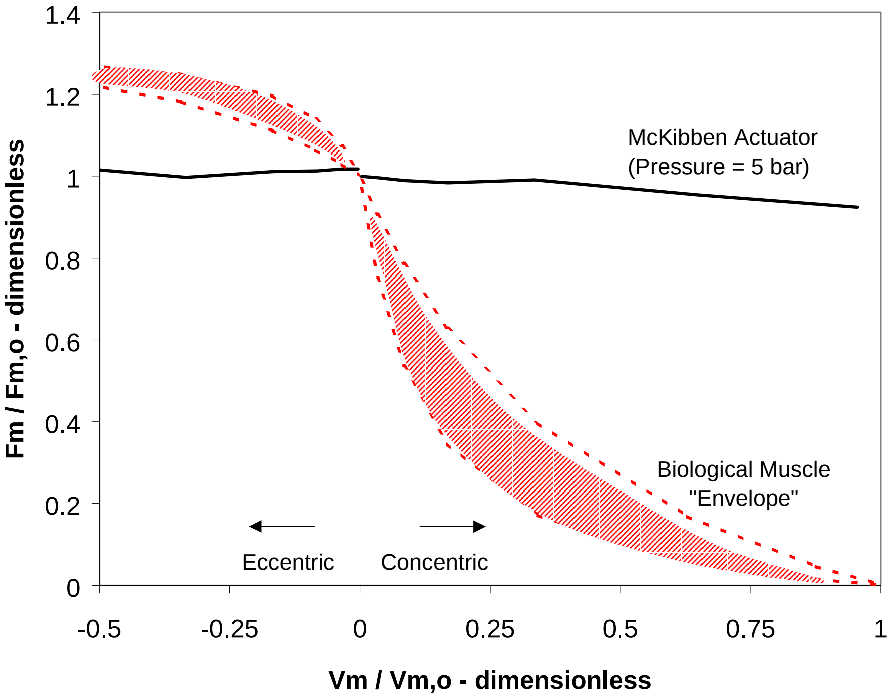

Figure 3.9: McKibben actuator output force (solid line) as a function of velocity compared with an animal "envelope" based on the Hill model of skeletal muscle (dashed line). The length of the muscle and actuator for which these curves are plotted are explained in the text.

Summary

From the experimental results, it is evident that the McKibben actuator has only a small amount of natural damping. The output force is clearly a function of length, but changes in velocity have only a small effect. When compared with the force-length design requirements identified in chapter two (equations 2.5a, b, and c), the McKibben actuator falls within the specified range. However, it is clear that the McKibben actuator has significantly different performance than biological muscle with respect to velocity (equations 2.5d and e). By adding additional damping, it may be possible to create an improved actuator whose properties are muscle-like with respect to both length and velocity. This topic will be addressed in the next chapter.

Chapter 4: Artificial Muscle

As demonstrated in chapter three, the McKibben actuator has little natural damping in comparison to skeletal muscle. One method for increasing the damping is to add a hydraulic damper in parallel to the pneumatic McKibben actuator as shown in figure 4.1.

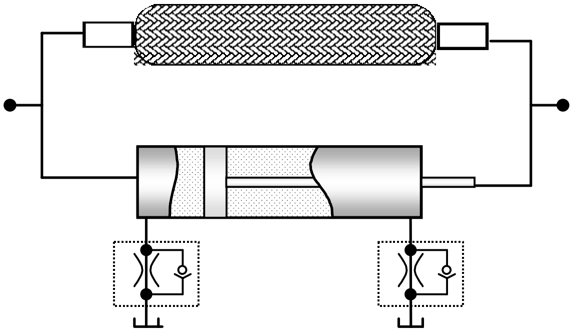

Figure 4.1: A hydraulic damper with orifice flow control valves in parallel with a McKibben actuator.

Damping Theory

For a damper in parallel with a McKibben actuator, the desired damping force (F_d) is simply:

$$F_d = F_{McK} - F_m \tag{4.1}$$

where F_{McK} is the McKibben actuator output force whose value can either be taken from experiment or from the model developed in Chapter 3. F_m is the force produced by biological muscle, modeled by equations (2.1) through (2.5).

For small hydraulic components, a common design constraint is the maximum allowable cylinder pressure (P_{cyl}) identified by the manufacturer. This constraint, along with the desired damping force, allows calculation of the minimum acceptable inside diameter (ϕ_1) of the hydraulic cylinder:

$$F_d = \left(\frac{\pi \phi_1^{\,2}}{4} \right) P_{cyl} \qquad (4.2).$$

The orifice size to provide the desired damping can be calculated from Bernoulli's equation using the assumptions of an ideal, incompressible fluid under steady state conditions. Bernoulli's equation is given by:

$$\frac{P_1}{\rho} + \frac{v_1^{\,2}}{2g} = \frac{P_2}{\rho} + \frac{v_2^{\,2}}{2g} \tag{4.3}$$

where P is pressure, v is fluid velocity, ρ is the fluid density, and g is the acceleration of gravity. The subscripts 1 and 2 refer to cylinder and orifice locations (see figure 4.2). While this application fails to rigidly hold these assumptions, Bernoulli's equation provides a simple model that yields necessary design specifications. These specifications can then be verified by experiment.

In addition to the relationship given by Bernoulli's equation, conservation of mass (m) demands:

$$\dot{m}_1 = \dot{m}_2 \tag{4.4}$$

such that:

$$\rho A_1 v_1 = \rho A_2 v_2 \tag{4.5}$$

where A is the cross-sectional area. An empirical enhancement to this equation is the multiplication of a discharge coefficient (C_d) to the right side of equation (4.5). This coefficient accounts for *vena contracture* at the orifice, an effective reduction in cross-sectional area (see figure 4.2). The value of this coefficient can be as low as 0.61 for very high Reynolds numbers, however, we have set this parameter to 1.0 for our simulations but plan future experimental measurements.

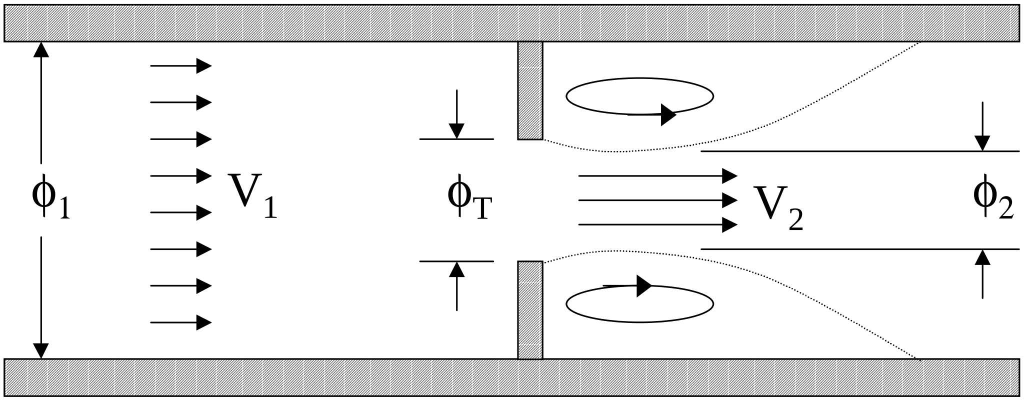

Figure 4.2: Schematic of an orifice flow restriction. Flow separation at the orifice throat results in *vena contracture*, an effective reduction in orifice diameter.

Substitution and simplification yields an equation for determining the ideal orifice size:

$$\phi_T{}^4 = \frac{\pi v_1{}^2 \phi_1{}^6 \rho}{8 F_d C_d{}^2 + \rho \pi \phi_1{}^2 v_1{}^2 C_d{}^2} \tag{4.6}$$

where ϕ_T is the throat diameter of the orifice. Of course, solving this equation requires specification of all the parameters on the right hand side of the equation. The working fluid was chosen to be mineral oil to minimize friction and cavitation. This specification gives a fluid density ρ of 900 kg/ m^3. The discharge coefficient (C_d) has been set equal to one as stated above. The remaining terms (v_1 , F_d , and ϕ_1) are application dependent and require specification of the muscle to be emulated.

Muscle Selection and Specification

One application of this technology is an actuator for a below-knee prosthesis. The general design of a below-knee prosthesis includes a socket for the residual limb, a load bearing pylon, and a foot. The socket shape and pylon length are custom components dependent on the level of amputation and the individual patient's anthropometry while prosthetic feet are available from a number of manufacturer's and can be tuned by a prosthetist to match a patient's performance.

For an intact human, the lower limb propulsive forces are produced by the *triceps surae* muscle group that includes the *gastrocnemius medialis*, *gastrocnemius lateralis,* and *soleus* muscles. The *gastrocnemius medialis* and *lateralis* muscles are bi-articulate about both the ankle and knee joints, while the *soleus* is mono-articulate about the ankle alone. To avoid the complexity of creating an actuator insertion above the knee, the design of our powered prosthetic limb will be mono-articulate about the ankle joint. The single actuator will need to produce the force, work and power of the *triceps surae* muscle group, but with the velocity analogous to the *soleus* muscle alone.

Numerous reports on the function and performance of the *triceps surae* are available in the literature. Mueller et al. (1995) reported a peak moment about the ankle of 90.2 N-m while walking at 1.26 m/s. Alexander and Vernon (1975) reported peak moments of 96 N-m and 107 N-m for walking at 1.8 m/s and 2.6 m/s respectively. Winters (1990) found peak moments of 110 N-m at 1.4 m/s. From data reported by Hof et al. (1983), it can calculated that peak moments of 115 to 160 N-m arise from walking at 2.0 m/s. Using an approximate ankle moment arm of 47 mm (Spoor et al., 1990) and an ankle moment of 110 N-m, the peak *triceps surae* force expected is 2340 N. From kinematic data also provided by Winters, it can be calculated that the maximum origin-insertion velocity of the *soleus* muscle and Achilles tendon during walking would be approximately 200 mm/s (concentric), while the velocity during the peak moment is significantly less at 61 mm/s. Using this data, Hill model axis intercepts (zero force maximum velocity and zero velocity maximum force) can be estimated. The maximum contraction velocity is expected to be 300 mm/s with zero output force and the maximum force is expected to be 3750 N at zero contraction velocity. This force could be achieved with McKibben actuators using three of the largest actuators in parallel (1-1/4 in. nominal braid diameter) at a pressure of 5 bar. Unfortunately, this combination would be too large to locate on a below-knee prosthesis. For practical considerations, it is realistic to consider mounting only two of the medium sized actuators (3/4 in. nominal braid diameter) with a hydraulic damper on a real prosthesis.

If only two medium sized actuators (3/4 in. nominal braid diameter) are used in the prosthesis design, the peak isometric force that can be realized is only 1800 N. When used with a hydraulic damper at the velocities seen during normal walking, a peak moment of approximately 80 N-m can be produced. This moment is lower than reported in the literature for walking, but amputees tend to walk at slower speeds and hence might prefer a smaller ankle moment. Waters and others (1976) reported that the self-selected walking speed of a non-amputee control group (N=50) was 1.37 m/s. However, trauma induced below-knee amputee's self-selected pace was 1.18 m/s (N=14) while those patients whose amputations arose from vascular problems walked at an even slower pace of 0.75 m/s (N=13). While the goal remains replacing the lost function of the amputated limb, it seems reasonable to accept the use of an under-powered limb at this phase of development. Higher actuator pressures and efforts to improve the layout of the prosthesis design are two ways to increase the capacity of the system.

Cylinder Size

The inside diameter of the hydraulic cylinder can now be specified using equation (4.2). While the desired damping force can be calculated for any length and velocity using equation (4.1) and the biological model (equations 2.3 and 2.4; k_5 =-6.9, k_6 =13.8, k_7 =-5.9, $a / F_{m,o}$ =0.28, and $b / V_{m,o}$ =0.28), only the maximum damping force is necessary to size the cylinder. This condition occurs during a maximal concentric contraction (high shortening velocity and low output force). It follows from inspection that the maximum damping force must be equal to the maximum McKibben force of 1800 N. For a cylinder with a maximum allowable pressure of 13.6 MPa (2000 psi), the minimum cylinder diameter is 13.0 mm. Fortunately, a number of small bore cylinders are commercially available that meet these requirements.

Damping Simulation Results

The instantaneous orifice throat diameter (equation 4.6) required for Hill-like damping of two McKibben actuators in parallel (3/4 in. nominal braid size) is plotted in figure 4.3. The maximum velocity was taken to be 300 mm/sec for both eccentric and concentric contractions with a maximum McKibben actuation pressure of 5 bar. The inside diameter of the hydraulic cylinder was selected to be 22.3 mm (7/8 in.). As shown in equation (4.6), the orifice throat diameter varies with both velocity and length because the desired damping force is a function of velocity and length (see equation 4.1).

Equation (4.6) gives the instantaneous orifice throat diameter required to obtain the precise amount of damping desired. While an actively controlled orifice with a fast response might be able to perfectly mimic biological muscle, such an orifice would add a significant level of complexity to the system. Our approach is to add a passive, fixed orifice damper in order to minimize the additional complexity. Adopting this approach results in a simpler system, albeit with a corresponding loss in potential performance.

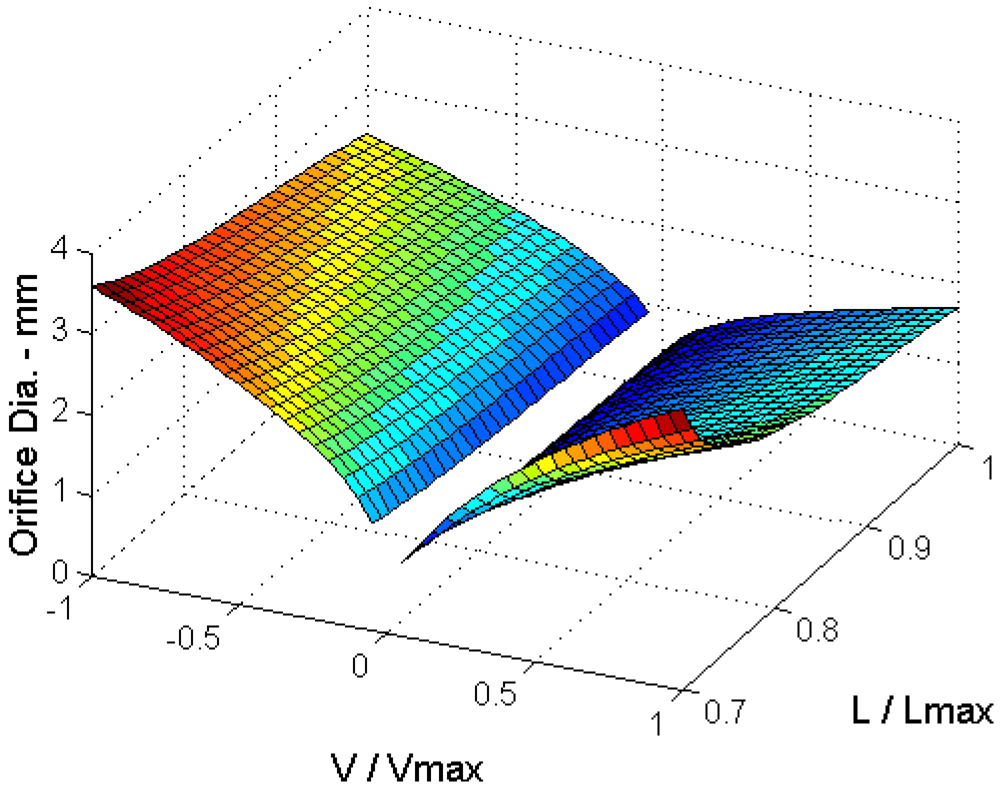

Figure 4.3: The instantaneous orifice diameter required to obtain Hill-like damping based on the properties of skeletal muscle and the McKibben actuator.

The damping force generated by a fixed orifice damper can be calculated from:

$$F_{\mathrm{hyd}} = \frac{\pi\rho\phi_1^{\,2}\,\mathrm{v}_1^{\,2}}{8}\left(\frac{\phi_1^{\,4}}{C_d^{\,2}\phi_{\mathrm{T}}^{\,4}} - 1\right) \quad (4.7).$$

It follows that the force produced by the artificial muscle (F_{am}), that is a McKibben in parallel with the fixed orifice hydraulic damper, is given by:

$$F_{\mathrm{am}} = F_{\mathrm{McK}} - F_{\mathrm{hyd}} \quad (4.8).$$

Orifice Selection

In order to optimize the damper design, the orifice selection is chosen by minimizing the square of the difference between a McKibben actuator with perfect, Hill-like damping and a McKibben with fixed orifice damping across the length and velocity ranges:

$$J_d = \int_{\mathrm{L}}\int_{\mathrm{V}} \left(F_d - F_{\mathrm{hyd}}\right)^2 \quad (4.9).$$

This optimization criterion can be thought of as minimizing a “volume” defined by force, length, and velocity coordinates. The volume represents the difference in performance of a McKibben actuator with perfect, Hill-like damping and one with a fixed orifice damper. The volume is bounded by physical limits of the actuator's contraction range (length), the tested velocity range, and the force produced by the actuator when the actuation pressure is maximal.

The parameters used in determining the optimal orifice throat diameters for the eccentric and concentric conditions are given in table 4.1. The maximum force was selected to be 1800 N which corresponds to two McKibben actuators in parallel (3/4 in. nominal braid diameter) at 5 bar. The maximum velocity was 300 mm/s for both eccentric and concentric contractions. For these conditions, the optimization criterion was minimized when the eccentric orifice diameter was 1.5 mm (rod side of cylinder) and the concentric orifice diameter was 1.2 mm (bore side of cylinder).

Table 4.1: Damping system parameters used in conjunction with Bernoulli's equation to design the damping element.

Parameter	Value - units
Number of Actuators	2
Braid Dimension	¾ - inches[1]
Bladder Dimensions	3/8 x 1/16 - inches[2]
ϕ_1 (cylinder diameter)	22.225 mm (7/8 in)
ϕ_{rod} (rod diameter)	6.35 mm (1/4 in)
ρ (mineral oil)	900 kg/m^3
μ (mineral oil)[3]	0.03150 Pa-sec

[1] The braid is described by the manufacturer's designation for nominal diameter in inches, Alpha Wire Corp., Elizabeth, New Jersey, U.S.A.

[2] The bladder is described by the internal diameter (inches) and the wall thickness (inches) following the convention typical of most manufacturers.

[3] The viscosity term is not required by Bernoulli's equation (ideal fluid assumption) but is provided for completeness.

Damping Experiments

To measure the force-velocity properties of the proposed hydraulic damper and validate the use of Bernoulli's equation, we conducted a series of experiments with the axial-torsional Bionix™ (MTS Systems Corp., Minnesota, USA) tensile testing instrument described earlier. The damper system was composed of a hydraulic cylinder, a ballast chamber, and two valves. The hydraulic cylinder was a Clippard Minimatic Cylinder (Clippard Instrument Laboratory, Cincinnati, Ohio, U.S.A.; part number 7D-3) with a 22.2 mm (7/8 in) bore, a 76.2 mm (3 in.) stroke, and a maximum cylinder pressure of 13.6 MPa (2000 psi). The ballast chamber, to accommodate fluid displacement from the cylinder piston rod, was constructed from polyvinyl chloride pipe and had a volume of 100 ml. The two valves, one each for concentric and eccentric damping, incorporated check valves to provide unrestricted fluid flow into the cylinder while metering the fluid flow out through an orifice. To facilitate development, adjustable needle valves were used instead of fixed orifices (Parker Hannifin, Elyria, Ohio, U.S.A.; part number F200B4).

The theoretical development provided precise orifice dimensions, but in practice, the equivalent orifice throat dimensions of a needle valve cannot be obtained. As a result, the valves were adjusted until the desired damping force was achieved at a velocity of 200 mm/s. The velocity of 200 mm/s was selected as this is the peak velocity achieved between the origin and insertion of the *soleus* muscle and Achilles tendon during normal walking (Winters, 1990 and Spoor et al., 1990). The hydraulic damping force was predicted (equation 4.7) using fixed orifices selected with equation (4.9). At 200 mm/s, the hydraulic concentric damping force is 820 N and the hydraulic eccentric damping force is 260 N for these conditions.

Each experiment measured the force output at a specified velocity. The instrument's digital controller was used to input step velocity profiles for concentric and eccentric contractions of 1, 10, 25, 50, 100, 150, 200, 250, and 300 mm/s. The "loop direction" (shown on the result figures with arrows) indicates the direction of movement. The test begins with the damper fully extended (stroke position of 68 mm) and performs a shortening displacement. The shortening displacement ends when the damper is fully retracted (stroke position of 0 mm). The lengthening displacement then begins from this retracted position and the damper is then fully extended to complete the test "loop."

The damping velocity and force produced during the shortening displacements are shown in figures 4.4 and 4.5 respectively. Because the fluctuations in force and velocity were negligible for the step input test velocities of less than 100 mm/s, they are not shown. As can be seen in the figure 4.4, the step velocity profile cannot be instantaneously obtained and gets progressively worse at higher velocities. This effect, arising from the testing instrument, is most severe at the beginning of the loop. Small variations can be seen in the velocity profile beginning at 100 mm/s. These variations increase with increasing commanded velocity and peak at 300 mm/s. Both the delays in obtaining the desired velocity and the fluctuations can be seen in the damper force output shown in figure 4.5.

The damping velocity and force produced during the lengthening displacements are shown in figures 4.6 and 4.7 respectively. As before, the slower velocities are not shown. Figure 4.6 shows similar delays and fluctuations in the target velocities during the lengthening phase of the loop. As a result, the damper's force profile is affected, particularly at higher velocities at the beginning of the lengthening displacement (see figure 4.7). Note that the damping force required during lengthening is significantly lower than the damping force required during shortening.

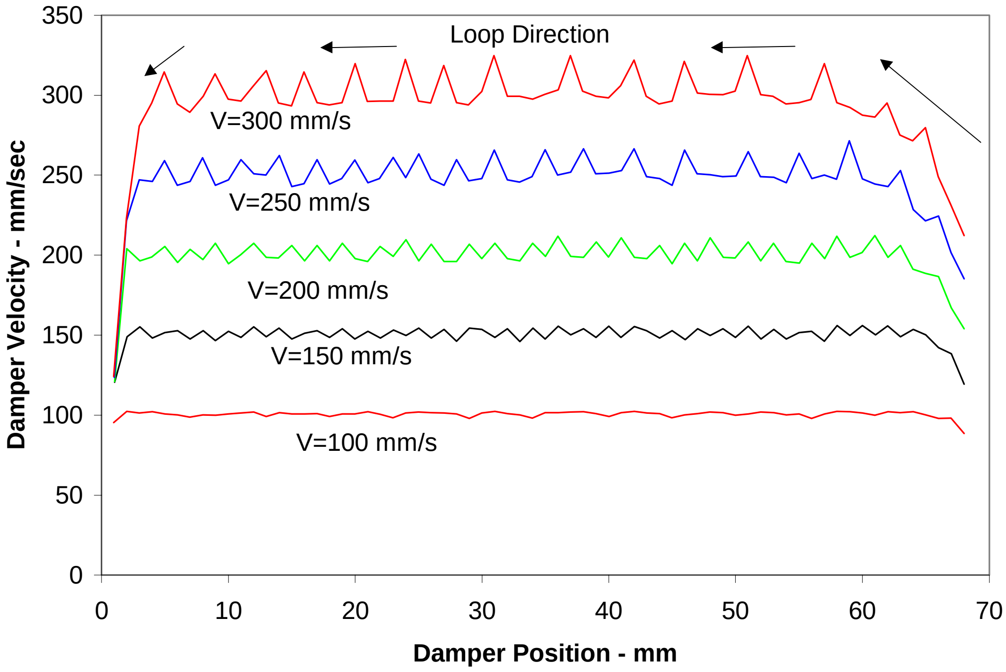

Figure 4.4: Concentric damping velocity versus position.

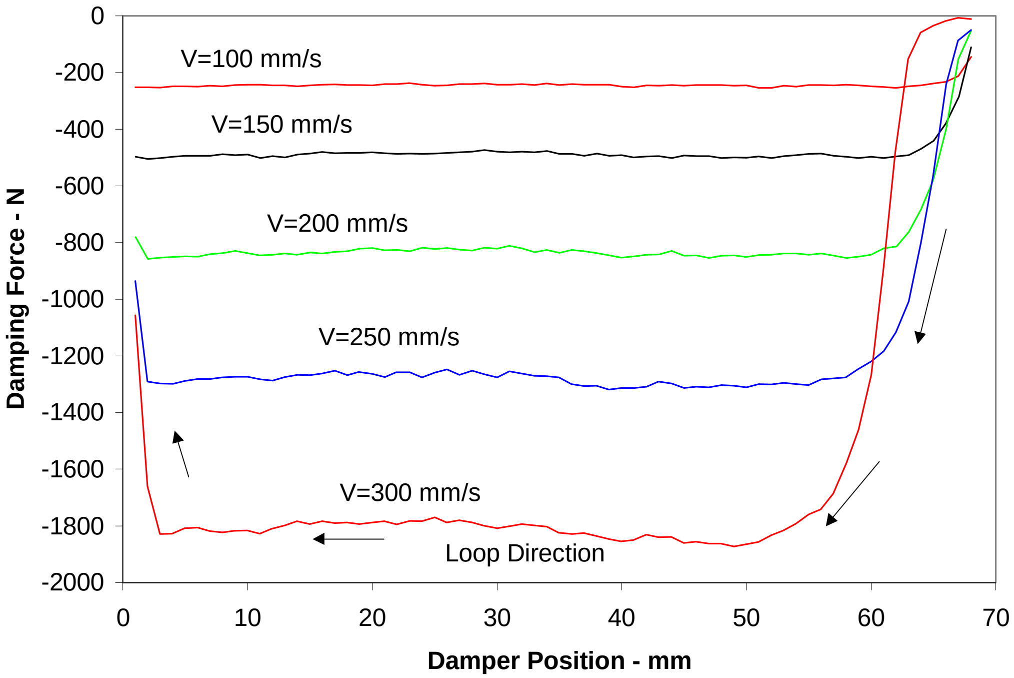

Figure 4.5: Concentric damping force versus position.

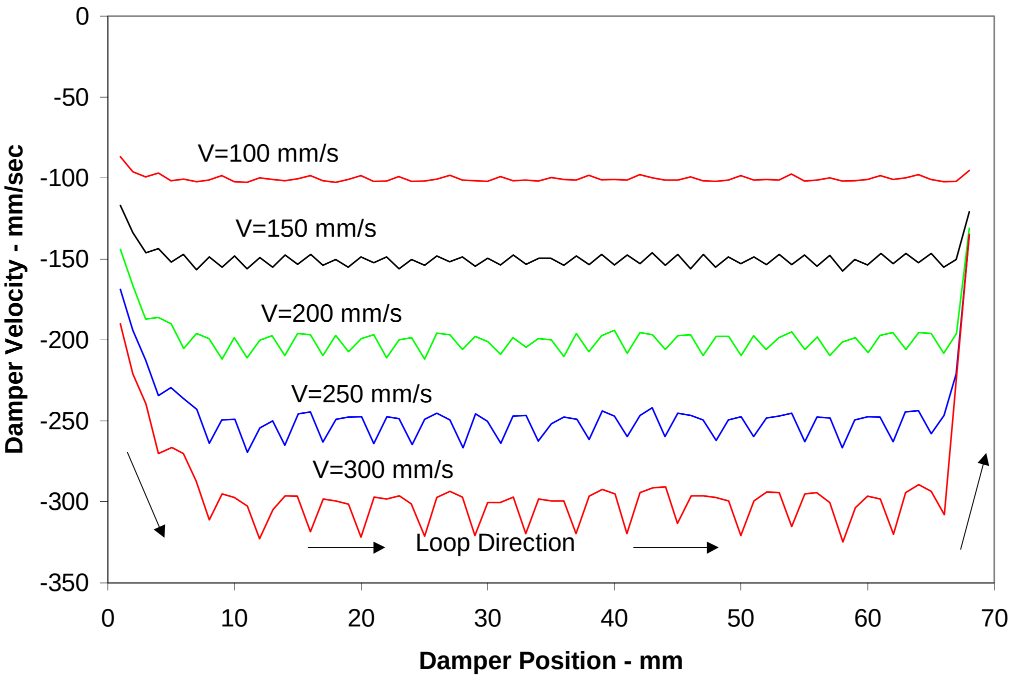

Figure 4.6: Eccentric damping velocity versus position.

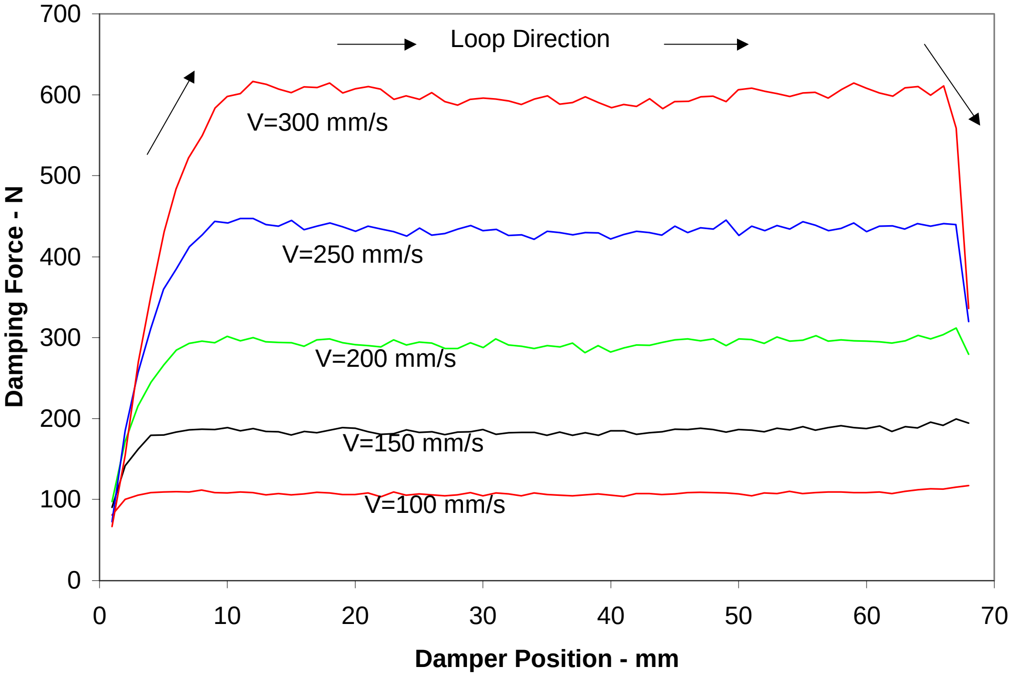

Figure 4.7: Eccentric damping force versus position.

A summary of the experimental results is shown in figure 4.8 where the damping force is plotted as a function of velocity. Error bars represent one standard deviation from the mean force across the entire damper stroke length of 68 mm. The realized damping force is slightly higher than the desired force at low velocities indicating lipseal friction on the order of 20 to 30 N. At high velocities, the realized damping force is close to the desired force, however the standard deviations are larger than expected, particularly for the concentric velocity of 300 mm/s. This large standard deviation occurs because the damping force took some time to develop at the higher velocities as shown in figure 4.5 and 4.7. High velocity step inputs are difficult to achieve in practice.

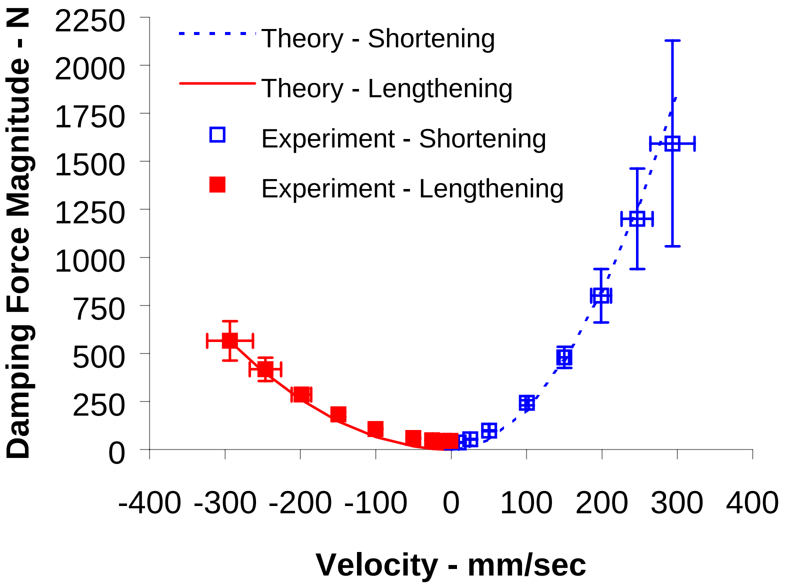

Figure 4.8: Desired and experimental damping force as a function of velocity.

Artificial Muscle Simulation Results

As presented in chapter two, a parabolic force-length and hyperbolic force-velocity relationship can be used to model skeletal muscle (equations 2.3 and 2.4; k_5 =-6.9, k_6 =13.8, k_7 =-5.9, $a / F_{m,o}$ =0.28, and $b / V_{m,o}$ =0.28). The results are plotted in figure 4.9 with the added constraint of restricting the muscle length to that equal or less than the resting length.

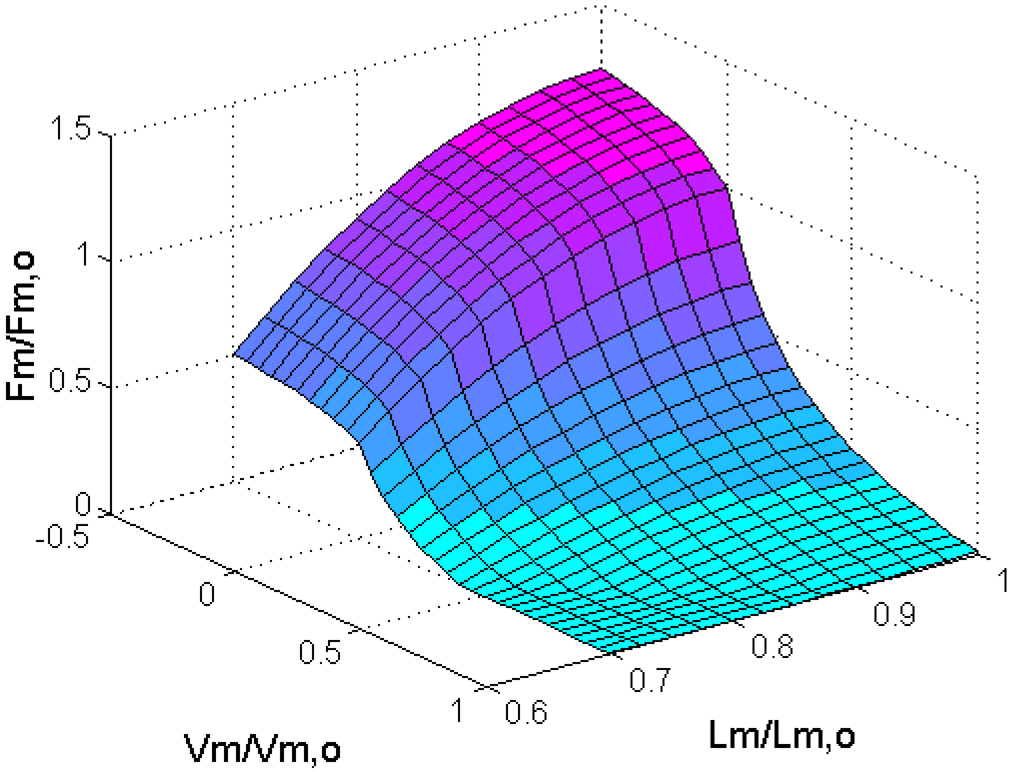

Figure 4.9: The force-length-velocity relationship of skeletal muscle with the added constraint that the muscle's length cannot be elongated beyond its resting length.

If an ideal, Hill-like damper were placed in parallel with the McKibben actuator, the results would be as shown in figure 4.10. This hypothetical, ideal damper would rely on an orifice whose diameter can be varied instantaneously and whose cylinder and hydraulic values are given in table 4.1. As noted earlier, this could be achieved using an actively controlled needle valve with a fast response in an effort to perfectly mimic biological muscle.

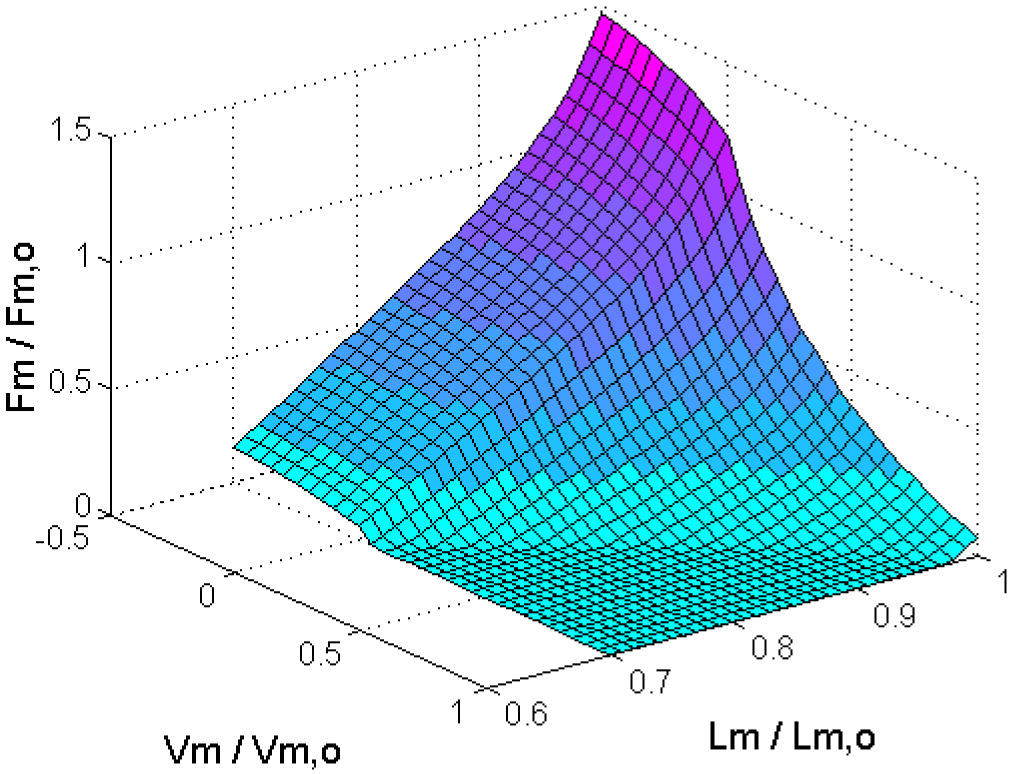

Figure 4.10: Predicted output force of a McKibben actuator in parallel with perfect, Hill-like damper.

The results of such an artificial muscle with a perfect damper can be compared with the results of a more practical, fixed orifice damper. Simulation results of an artificial muscle using a fixed orifice damper are shown in figure 4.11, again in dimensionless format. The cylinder and hydraulic values are given in table 4.1. The eccentric orifice diameter was 1.5 mm (rod side of cylinder) and the concentric orifice diameter was 1.2 mm (bore side of cylinder).

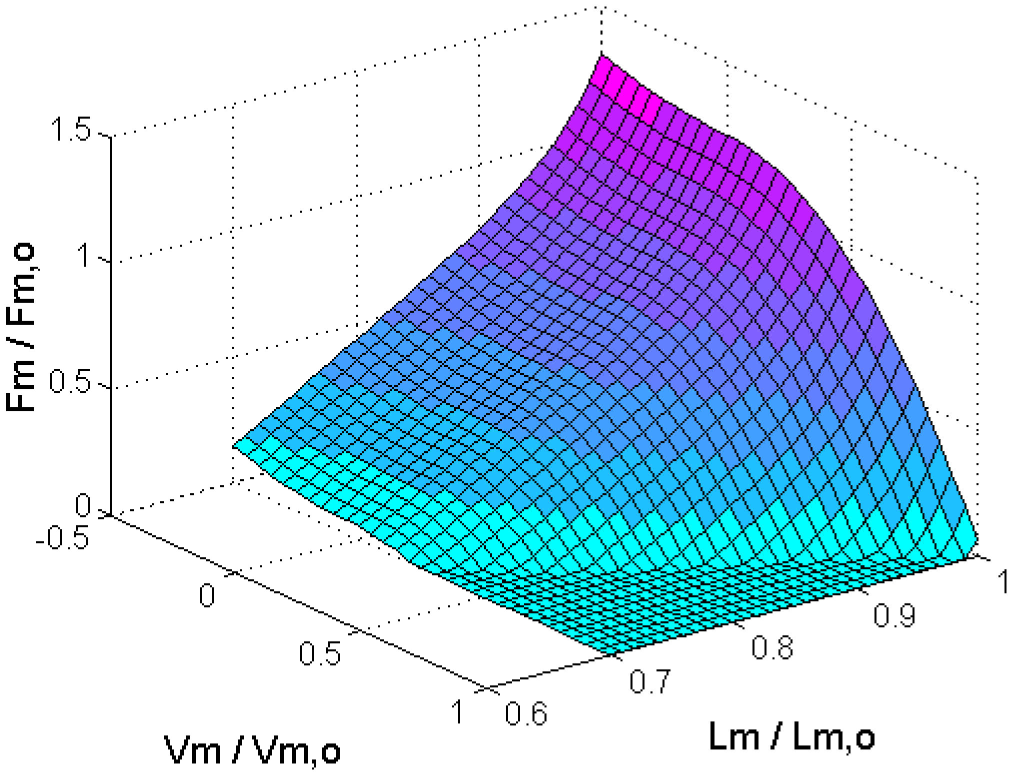

Figure 4.11: Predicted output force of a McKibben actuator in parallel with a passive, fixed orifice hydraulic damper.

Discussion

The fixed orifice damper, in parallel with a McKibben actuator, provides a first order approximation to the desired Hill model damping of biological muscle. However, identification of a number of caveats is in order. The hydraulic model presented here (equations 4.1 through 4.9) is a simple model intended to capture the significant factors for design purposes. This model ignores losses due to piston rod lipseal friction, frictional losses within the hydraulic lines, the effects of *vena contracture* (ignored when C_d =1.0), and other sources. Furthermore, many of these losses are a function of the Reynolds number. In this system, the Reynolds number varies widely depending on location and actuator contraction velocity.

Lastly, the biological model (developed in chapter 2) demonstrates significant variability not only across different species but also upon contraction direction (concentric or eccentric). Refinements to the proposed system can certainly be introduced such as stepper motor controlled needle valves or passive orifices constructed from materials that deform under pressure.

A direct comparison of these results, at a fixed length, can be seen in figure 4.12. Because the hydraulic damping force is a function of the square of the velocity, the shape of the force v. velocity curve for the artificial muscle is convex instead of the desired concavity exhibited by biological muscle (except as noted for *in-vivo* experiments shown in figure 2.7).

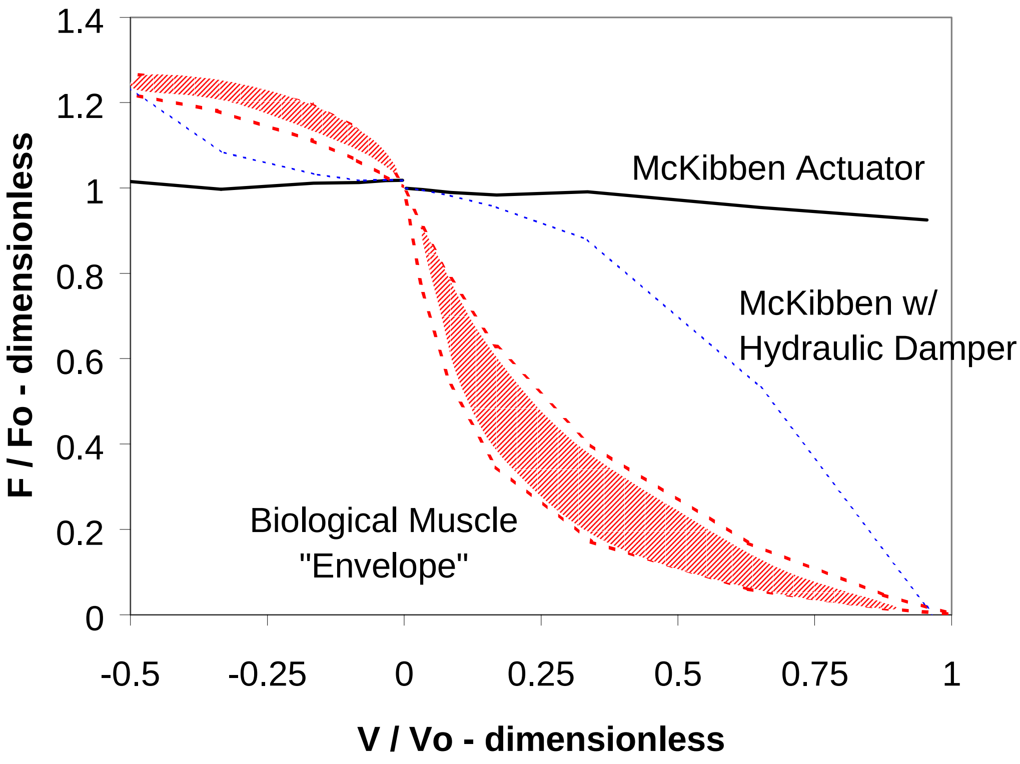

Figure 4.12: Comparison of the force-velocity profile of biological muscle with the current McKibben actuator acting alone and the predicted profile of the artificial muscle using a hydraulic damper with fixed orifice sizes in parallel with a McKibben actuator.

Summary

To achieve the damping exhibited by skeletal muscle as predicted by the Hill model, a hydraulic damper has been designed to work in parallel with McKibben actuators. The damper design was based on Bernoulli's equation and assumes steady state flow of an ideal, incompressible fluid. To validate the design and the use of these assumptions, experiments were conducted on the damper alone. The results indicate the damper behaved as predicted. Furthermore, when placed in parallel with McKibben actuators, it is expected that an appreciable portion of the desired damping exhibited by biological muscle can be produced and the system will emulate the performance of biological muscle.

Chapter 5: Biological Tendon

Tendon has two distinct purposes: one for transmitting muscular action into forces for fine manipulation and the other for energy storage during locomotion (Ker et al., 1988). As our applications include mobile robots and lower limb prosthetics, the focus of our modeling efforts will be on energy storing tendons. Data from a variety of mammals will be examined and used to formulate a model for an energy-storing tendon. This model will be compared with those proposed by others and then used to design an artificial tendon.

Animal and Human Data

There is a wide body of literature describing the behavior of energy storing tendons under load. Some investigators have removed structural characteristics by reporting stress (σ) versus strain (ε), while others have reported the form in which the data was recorded, namely force versus elongation. The stress v. strain curve (or force v. elongation) of tendon exhibits a characteristic toe region where stress (or force) increases slowly with strain (or elongation), followed by a more or less linear region until failure. Confounding experimental problems include the freshness of the specimen (some investigators have used embalmed tissue), grip failures, and selection of appropriate, physiological strain rates (e.g. Lewis and Shaw, 1997; Ker et al., 1988).

The tangent modulus (E_t) is used by many investigators to describe a tendon's performance under load. It can be calculated from the slope of the experimentally determined stress-strain curve:

$$E_t = \frac{\partial \sigma}{\partial \varepsilon} \qquad (5.1).$$

Bennett and others (1986) noted that the reported tangent modulus is often a function of the maximum stress on the tendon instead of depending on the tendon within or across different species. Following the work of Bennett et al. (1986, their figure 3), the tangent modulus is plotted versus maximum stress for a variety of mammals in figure 5.1. Bennett's data on the donkey, pig, horse, wallaby, sheep, and deer is supplemented with additional data from the sheep (Ker, 1978; his tables 1 and 2), horse (Herrick et al., 1978; their figures 6 and 9; Riemershma and Schamhardt, 1985; their figures 4 and 5), rat (Minns and Muckle, 1982; their figure 2), dog (Webster and Werner, 1983; their table 1), pig (Woo et al., 1981; their figure 7), wallaby (Ker at al., 1986; their table 2), camel (Alexander et al., 1982; their test on page 305), and human (Harris et al., 1966; their figure 6 and text; Lewis and Shaw, 1997, their figure 5). Of course, a variety of experimental protocols were used by the different investigators, but all of the tendon data presented in figure 5.1 are from lower limbs and involve energy storage during locomotion.

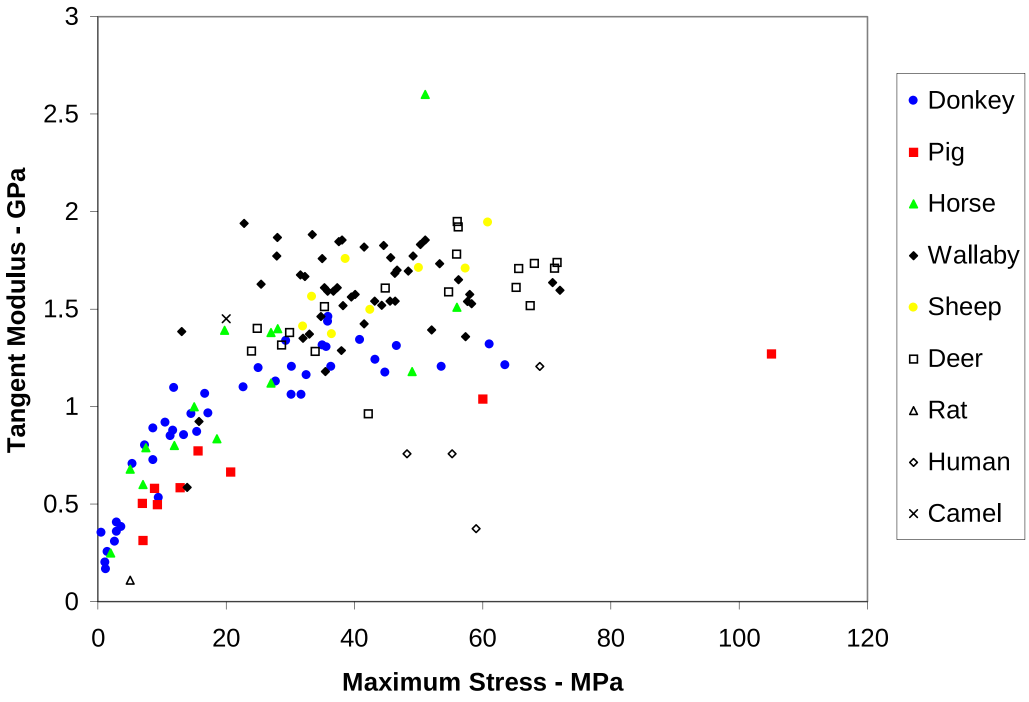

Figure 5.1: The tangent modulus versus maximum stress from a variety of mammals whose lower limb tendons are suspected to store significant amounts of energy during locomotion.

Evident in figure 5.1 is widespread variation in the data; however, the tangent modulus clearly increases with increasing maximum stress. Unfortunately, the maximum stress obtained under in-vivo conditions is not well understood. One study attempting to measure the maximum force in the *Achilles* tendon was conducted by Komi (1990). Experimenting with an *in-vivo* transducer, Komi calculated the *Achilles* tendon stress of a 73 kg male running at 6.0 m/s to be approximately 111 MPa. Komi’s *in-vivo* value is significantly larger than most of the *in-vitro* or *in-situ* experimental data presented in figure 5.1 and clearly demonstrates the need for caution in interpreting experimental data because the maximum force may be far less than that exerted *in-vivo*.

Tendon Models

With respect to human performance, a number of biomechanical models of the *Achilles* tendon are available in the literature (e.g. Bobbert et al., 1986; Zajac, 1989; Bobbert and Ingen Schenau, 1990; Voigt et al., 1995a and b; Hof, 1998). These models attempt to capture tendon characteristics by monotonically relating tendon force (or stress) to elongation (or strain) in a form given by:

$$F = k \cdot l_t^{\,n} \tag{5.2}$$

where F is the force across the tendon, l_t is the elongation of the tendon, and k and n are empirically determined constants. Reformulated, equation (5.2) becomes:

$$\sigma = E\varepsilon^{n} \tag{5.3}$$

where stress (σ) and strain (ε) are related by the empirically determined modulus of elasticity (E).

To enable switching between equations (5.2) and (5.3), structural properties of tendon are required, namely the tendon cross-sectional area and length. A number of studies have reported the cross-sectional area of the *Achilles* tendon and their results are tabulated in table 5.1. The mean cross-sectional area from these investigations is 65 mm^2. The length of the *Achilles* tendon is more difficult to ascertain due to the area across which it attaches to bone and muscle. Yamaguchi and others (1990) cite two references for tendon lengths of the *gastrocnemius medialis*, *gastrocnemius lateralis*, and *soleus* muscles that form the *triceps surae*. The average length of these tendons, collectively taken as the *Achilles* tendon, is 363.5 mm.

Table 5.1: *Achilles* tendon cross-sectional area as reported by various sources in the literature.

Source	Cross-sectional area – mm^2
Perrynowski and Morrison, 1985	49
Woittiez et al., 1985	55
Ker et al., 1987	89
Abrahams, 1967	61
Komi, 1990	81
Voight, 1994	65
Lewis and Shaw, 1997	54

Using the length and cross-sectional area data of the Achilles tendon, the biomechanical models reported in the literature (Bobbert et al., 1986; Zajac, 1989; Bobbert and Ingen Schenau, 1990; Voigt et al., 1995a and b; Hof, 1998) can now be formulated in terms of stress versus strain (see table 5.2). Particular attention should be paid to the work of Hof (1998) who reported *in-vivo* measurements on the human *triceps surae – Achilles* tendon complex. Hof lumped the series elasticity of muscle with tendon, and found his experimental finding's were best represented by a model with a quadratic toe region followed by linear region whose stiffness was proportional to the number of active muscle fibers. Given the complexity of this model, Hof also proposed a simpler model in the form of equation (5.3). Using an ankle moment arm of 47 mm (Spoor et al., 1990), a cross-sectional area of 65 mm^2, and a length of 363.5 mm, the equivalent modulus of elasticity from his results is 5773 (s.d. 1561) MPa with a strain exponent of 2.

For comparison with the tendon models reported in the literature, an energy-storing tendon (EST) model will also be presented. The EST model is simply a least squares fit to the animal data in figure 5.1 resulting in E=10289 MPa and n=1.91 (r^2=0.6942). However, caveats abound as different methods were used to collect the data and some data points represent many specimens while others represent only a single specimen. Never the less, the EST fit is nearly the same as the model reported by Voigt and others (1995a and b). As can be seen in table 5.2, there are significant differences between the other models for both the modulus of elasticity and the strain exponent.

Table 5.2: Modulus of elasticity (E) and strain exponent (n) for several biomechanic models of tendon.

Model	E - MPa	n - dimensionless
Bobbert et al., 1986	6250	2
Zajac, 1989	12007	1
Bobbert and Ingen Schenau, 1990	27614	2
Voigt et al., 1995a and b	13333	2
Hof, 1998	5773	2
EST Model	10289	1.91

It is now possible to plot the tangent modulus versus stress of both the experimental data and the biomechanical models (see figure 5.2). Interestingly, the data is bounded by the two models by Bobbert and others (Bobbert and Ingen Schenau, 1990; Bobbert et al., 1986) while both the Voigt (Voigt et al., 1995a and b) and the EST models are near the mean values. The data from Hof (1998) is on the lower bound, but closer to the few human data points (Harris et al., 1966; their figure 6 and text; Lewis and Shaw, 1997, their figure 5) than the other models.

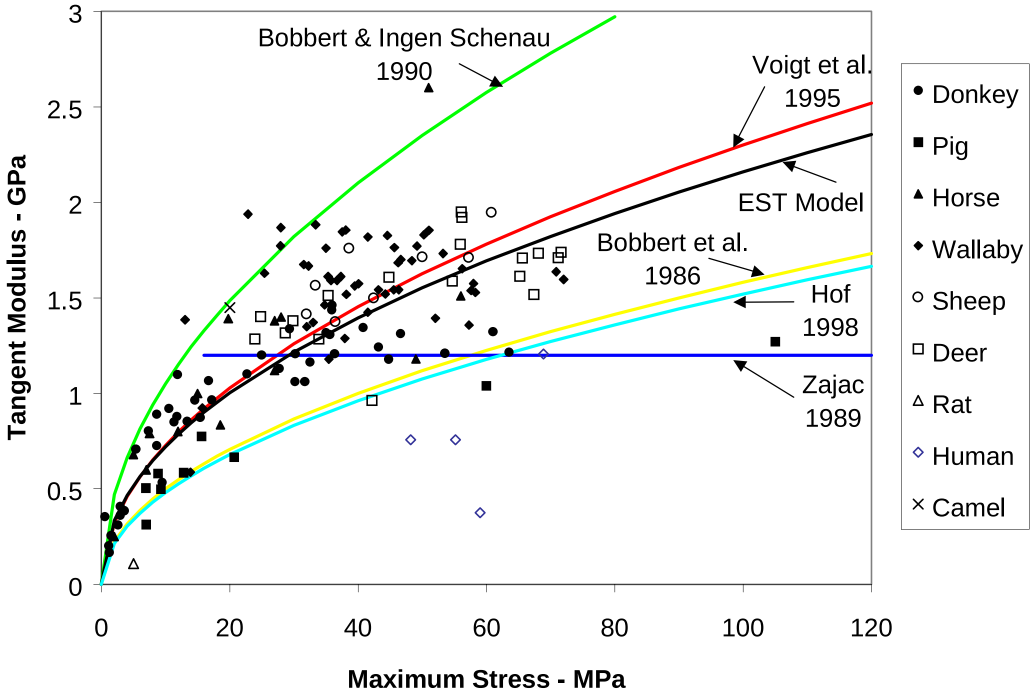

Figure 5.2: The tangent modulus versus maximum stress for a variety of mammals plus several different tendon models.

Design Requirements

To specify the requirements for an artificial tendon, it is useful to plot the biomechanic models in the more conventional stress versus strain format (see figure 5.3). Clearly all but Zajac's model (1989) reproduce the characteristic toe region followed by a more or less linear region. For applications using a design based on the relationship in equation (5.3), these results imply it is reasonable to allow for a tendon that falls between Bobbert and Ingen Schenau (1990) and Hof (1998) such that:

$$5773 \leq E \leq 27614 \qquad (5.4a)$$

$$n \approx 2 \qquad (5.4b).$$

where n is dimensionless and the units of E are MPa.

These requirements will be used in chapter six to design an artificial tendon suitable for use in a robotic or prosthetic application.

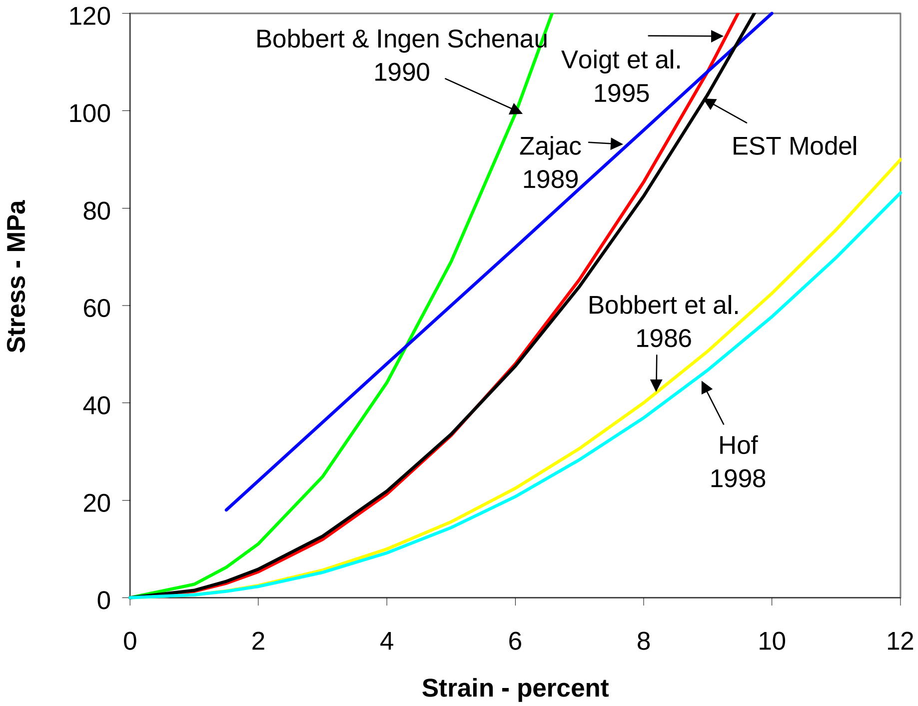

Figure 5.3: Tendon stress versus strain of five different biomechanic models of the *Achilles* tendon.

Chapter 6: Artificial Tendon

An artificial tendon is a key component in the design of a musculo-tendon system. As the tendon is arranged in series with the muscle, all of the force produced by the contractile element must be transmitted through the tendon. In 1969, Frisen and others proposed a physical model of tendon that used a number of offset linear springs arranged in parallel (see figure 6.1) to achieve the parabolic force-elongation relationship described in chapter five. With more springs comes better performance, but practical realization of such a system suffers from a penalty in terms of the space to accommodate numerous springs as well as their associated weight. Our approach was to utilize two springs to minimize this penalty, albeit with the commensurate loss of performance.

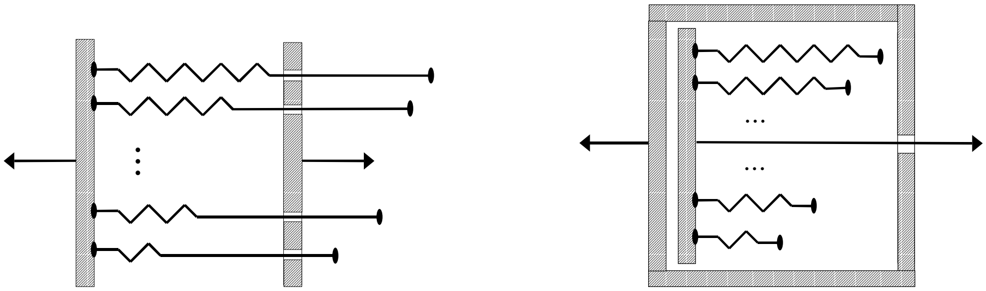

Figure 6.1: Offset linear springs can achieve a “tendon-like” parabolic force-length relationship (adapted from Frisen et al., 1969). The implementation on the left accomplishes this with the springs in tension, while the implementation on the right does the same but with the springs in compression.

A model of this two-spring system is given by:

$$F_{\text{2spring}} = K_{\text{eq}} x \tag{6.1}$$

where F_{2spring} is the force of the two offset springs, x is the deformation, and K_{eq} is the equivalent spring constant.

Artificial Tendon Design

The design of a two-spring artificial *Achilles* tendon used the EST model as the desired performance objective. The spring constants ($\mathrm{K_a}$ and $\mathrm{K_b}$) were selected by minimizing the difference in stored energy between the two spring implementation and the EST model:

$$J_t = \int_{\mathrm{Lt}} \left(F_{\text{2spring}} - F_{\text{EST}} \right) \tag{6.2}$$

where F_{2spring} is the force of the two offset springs, F_{EST} is the modeled tendon force, and L_{t} is elongation for springs in tension and deformation for springs in compression. The discontinuous point of the bi-linear $F_{2spring}$ curve where the load path transitions from one spring to two was also used as a constraint condition. This point was forced to lie upon the F_{EST} curve and is evident in figure 6.2. An alternative approach could square the term in equation (6.2) and discard the discontinuous point constraint.

While a variety of different spring types and design approaches could be used to achieve the desired results, the approach used here incorporated die compression springs arranged as shown on the right of figure 6.1. For calculating the spring constants for an artificial *Achilles* tendon, a walking ankle moment of 110 N-m (Winter, 1990) and a moment arm of 47 mm (Spoor et al., 1990) results in a 2340 N force acting through the *Achilles* tendon. By minimizing equation (6.1), the spring constant of the first spring (K_a) acting alone for 8.89 mm was calculated to be 63.9 N/mm. For deformations greater than 8.89 mm, a second spring acts in parallel with the first, with a spring constant (K_b) of 116.3 N/mm. The equivalent spring constant for the two springs acting in parallel is 180.2 N/mm. The result of this minimization is shown in figure 6.2 and is within the design requirements specified by equations 5.4a and b.

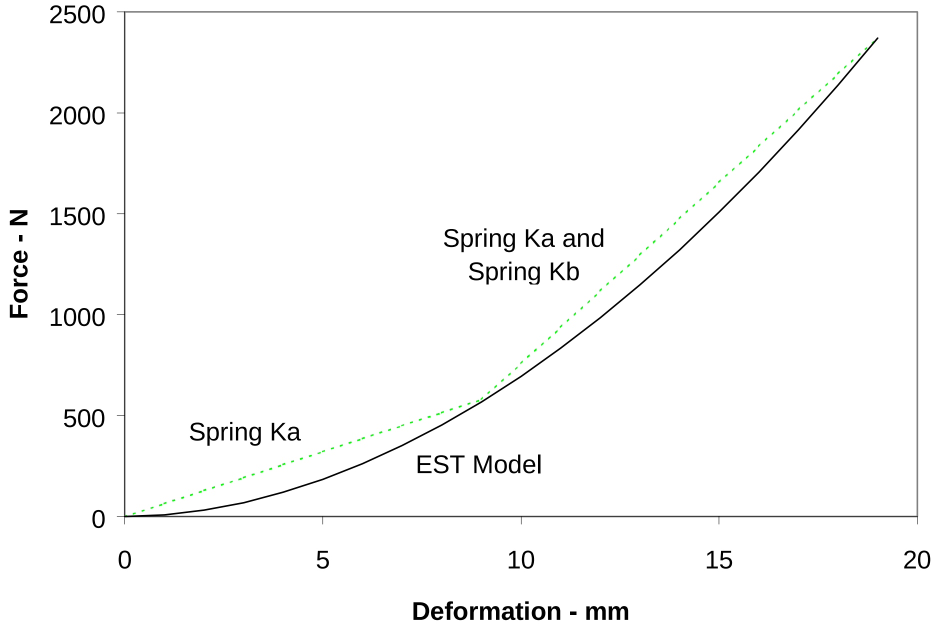

Figure 6.2: Tendon design based on two-spring model.

Experimental Methods

To measure the force-deformation properties of the proposed two spring artificial tendon, we conducted several experiments with the tensile testing instrument previously used to test the McKibben actuators (see chapter three) and the hydraulic damper (see chapter 5). Two commercially available springs were selected. Spring K_a had a spring constant of 65 N/mm and mass of 0.17 kg (Century Spring Corp., Los Angeles, CA, U.S.A.; part number D-79) and spring K_b had a spring constant of 115 N/mm and mass of 0.16 kg (Century Spring Corp., Los Angeles, CA, U.S.A.; part number D-1251). Each test (N=3) was conducted at a velocity of 1 mm/s for the working length of the spring.

The first series of tests measured the force-deformation properties of the springs individually. The second series of tests measured the force-deformation properties of the two springs configured in an offset, parallel arrangement.

Experimental Results

The experimental results of the individual spring tests are shown in figure 6.3. Error bars of one standard deviation are present but not evident due to very repeatable performance. The extremely linear, monotonic increase in force with deformation for each spring was expected as die compression springs are a mature technology.

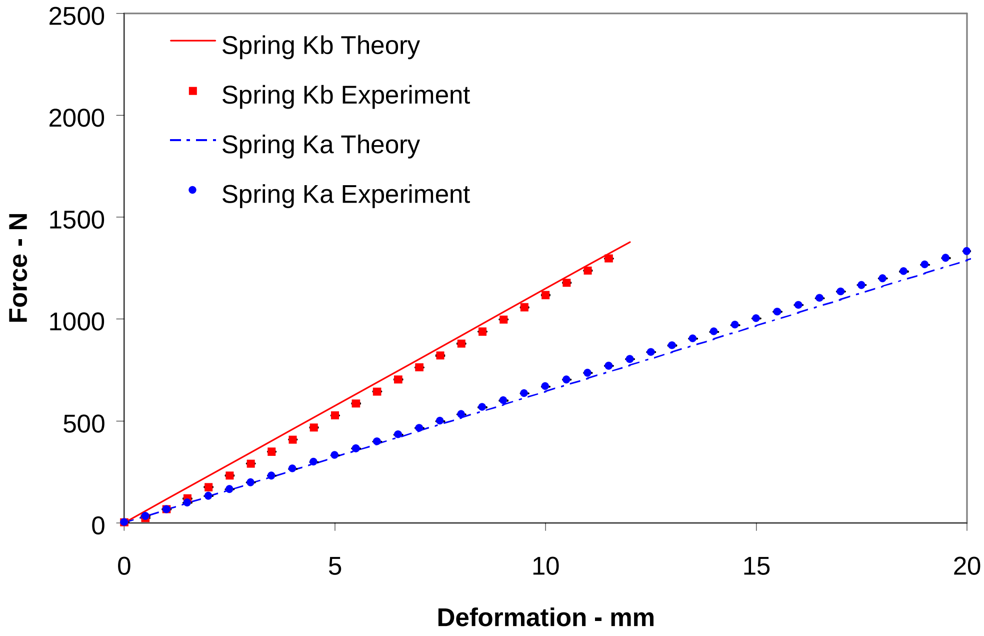

Figure 6.3: Experimental results (N=3) of the individual springs (K_a and K_b) demonstrate a linear force versus deformation relationship. Error bars of one standard deviation are present but not evident due to very repeatable performance.

The experimental results of the two springs configured in an offset, parallel arrangement are shown in figure 6.4. Again, error bars of one standard deviation are present but not evident due to very repeatable performance. The bi-linear, monotonic increase in force with deformation was expected based on the results from the individual spring tests. As predicted, the result is within the design requirements specified in chapter five (equations 5.4a and b).

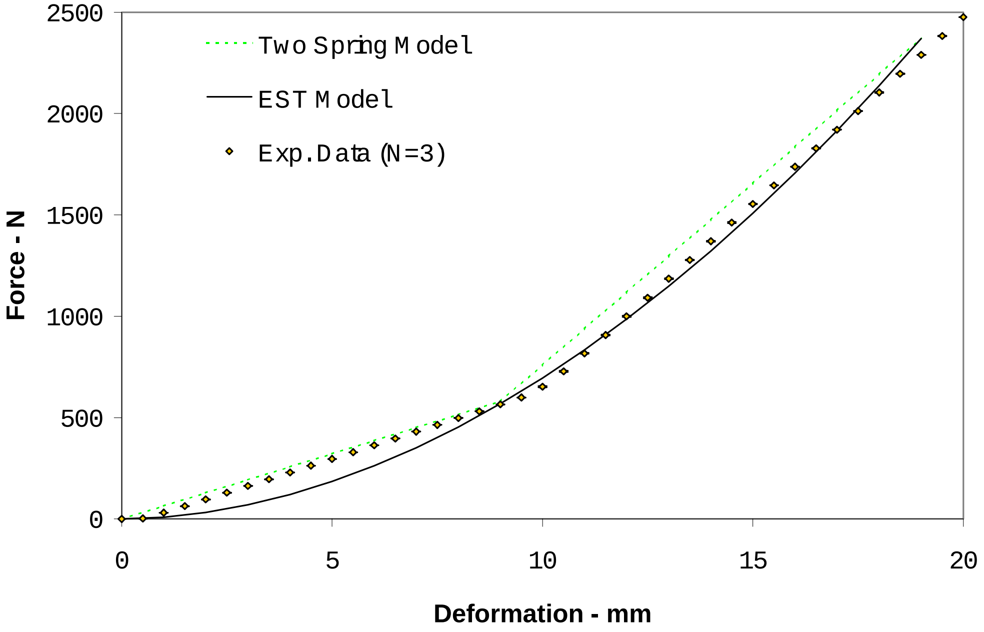

Figure 6.4: Experimental results (N=3) of the two springs configured in an offset, parallel arrangement demonstrate a bi-linear force versus deformation relationship. Error bars of one standard deviation are present but not evident due to very repeatable performance.

<u>Summary</u>

Industrial manufacturers have been fabricating die compression springs for many years, so it is not surprising the test results indicate linear response over the expected deformation range. Future efforts may focus on developing a non-linear spring polymer spring to achieve the desired performance with a lower weight penalty. However, the current test results of the two-spring implementation provide repeatable force versus deformation response with a combined mass of 0.33 kg. The result is performance close to the desired EST model and the design yields a suitable artificial tendon.

Chapter 7: Artificial Muscle-Tendon Performance

In the preceding chapters, both theoretical and experimental work was presented addressing the performance of individual components of the proposed artificial musculo-tendon system. In this chapter, a model of the musculo-tendon system will be presented to predict the system performance followed by experimental results.

Musculo-tendon Model

The artificial musculo-tendon system presented here is designed to replicate the function of the *triceps surae*. This muscle group is characterized by a short contractile element (i.e. the muscle) and a long tendon. The model used to predict its performance includes a muscle whose force-length-velocity properties are those of two McKibben actuators (nominal braid diameter of ¾ in.; equation 3.5) in parallel with a fixed orifice hydraulic damper (equation 4.7 and 4.8), which is then placed in series with the two-spring artificial tendon (equation 6.1).

Model Results and Discussion

The artificial musculo-tendon model provides a prediction of output force as a function of length, velocity, and activation pressure. Figure 7.1 presents model predictions for activation pressures of 2, 3, 4, and 5 bar. As can be observed in the figure, the output is proportional to the activation pressure. Higher pressures result in higher forces. For fast concentric contractions (positive velocity values), the output of the system can be zero force. This is similar to biological muscle when the velocity between the origin and insertion of the muscle-tendon is forced to be faster than the muscle can contract. The muscle then becomes slack. Furthermore, during concentric contractions, the muscle force decreases with the square of velocity due to the hydraulic damper. As noted in figure 4.4 (but see also figure 2.7), this result was expected and is the result of using fixed orifices. For eccentric contractions (negative velocity values), figure 7.1 demonstrates that the force increases with the square of velocity, again arising as the result of fixed orifices.

The muscle force increases with length; however, the artificial tendon results in a longer length with respect to force due to tendon stretch than would be expected without the tendon. This shifts the force-length relationship to the right along the length axis (compare with figure 4.12).

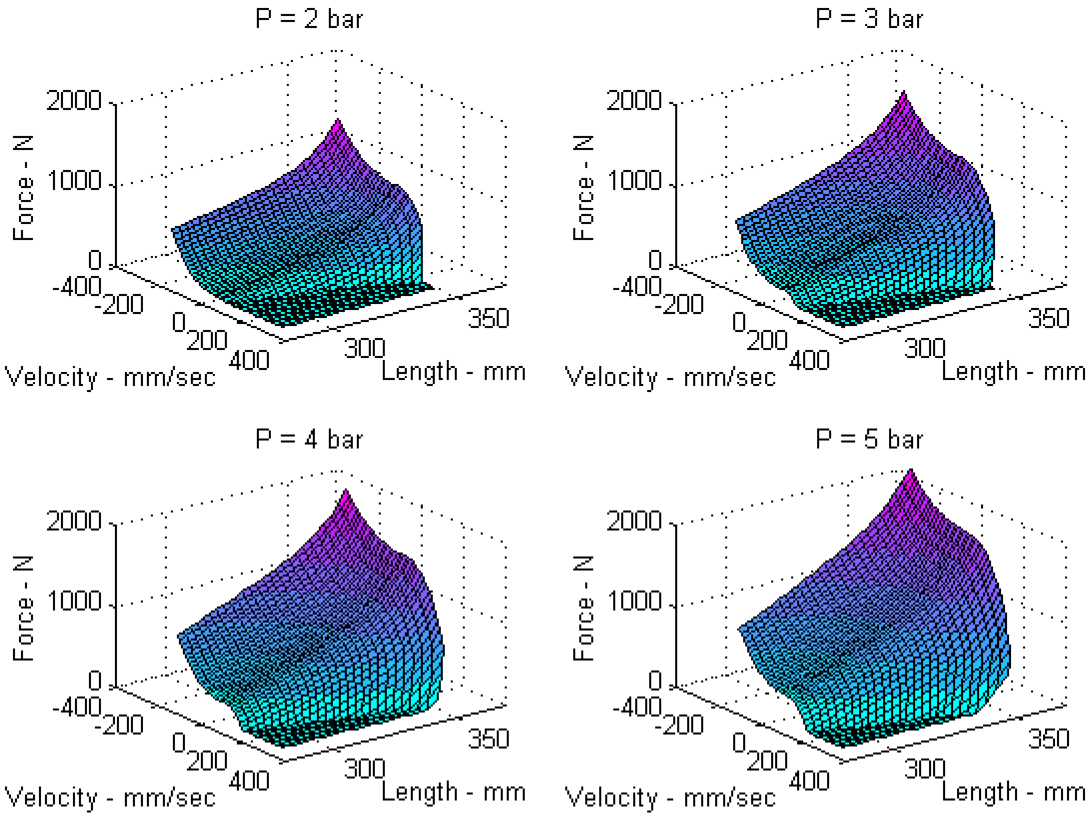

Figure 7.1: Model results for activation pressures of 2, 3, 4, and 5 bar.

<u>Experimental Test Set-up and Methods</u>

To compare the model predictions with the performance of the physical hardware, a number of tests were conducted. The artificial musculo-tendon system consisted of two McKibben actuators (3/4 in. nominal braid diameter with a resting length of 250 mm) placed in a parallel configuration. The actuators were also in parallel with a damper system composed of a hydraulic cylinder, a ballast chamber, and two valves (described in chapter four). The actuators and damper were in series with a two-spring artificial tendon (described in chapter seven) and aligned using four linear bearings (Thomson Industries, Port Washington, New York, U.S.A.; part number TWN-8). The complete set-up is shown in figures 7.2 and 7.3.

The tests were conducted using the axial-torsional Bionix™ (MTS Systems Corp., Minnesota, U.S.A.) tensile testing instrument (see figures 7.2 and 7.3). The concentric and eccentric contraction velocities were 1, 10, 25, 50, 100, 150, 200, 250, and 300 mm/s. Actuation pressures were 2, 3, 4, and 5 bar and applied through a pressure vessel whose volume was significantly larger than the actuators (described in chapter three).

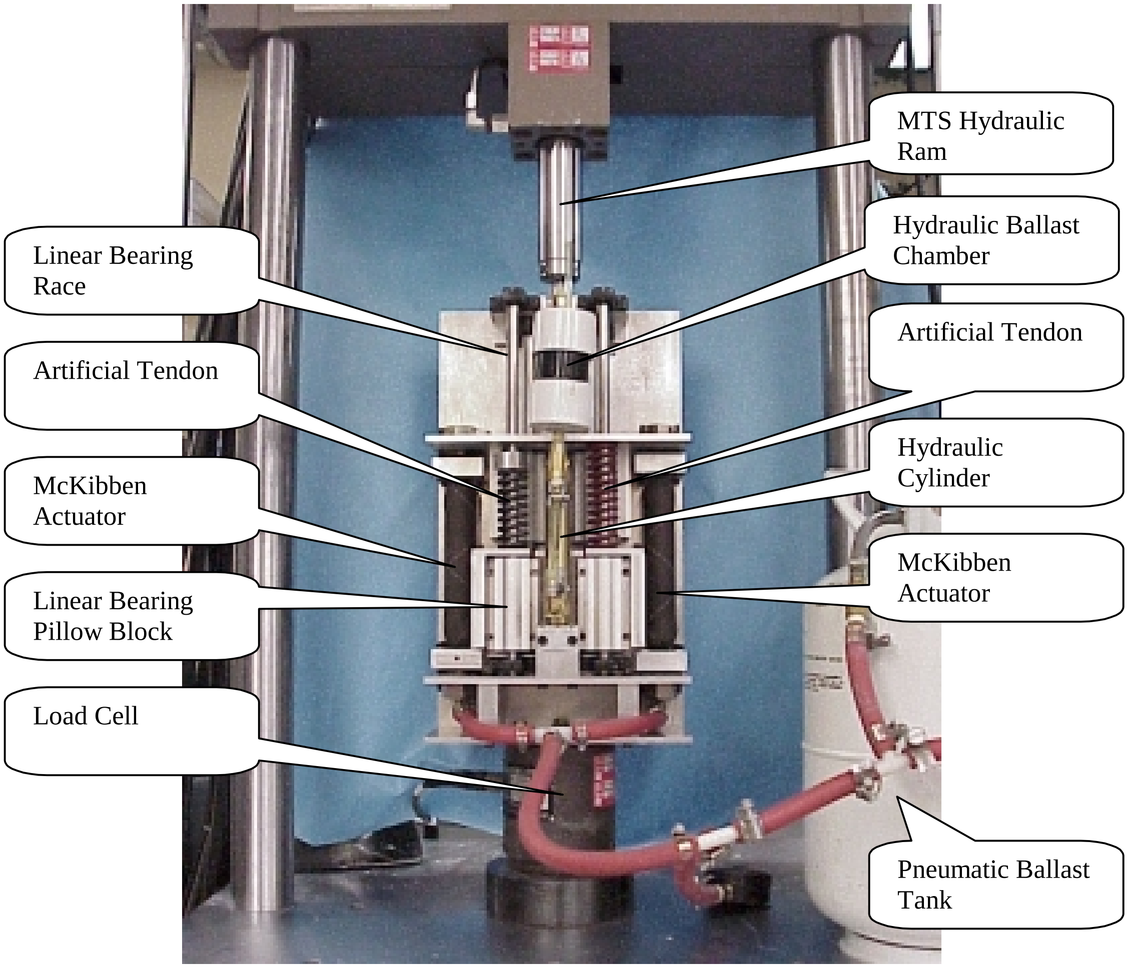

Figure 7.2: Artificial muscle and tendon experimental set-up.

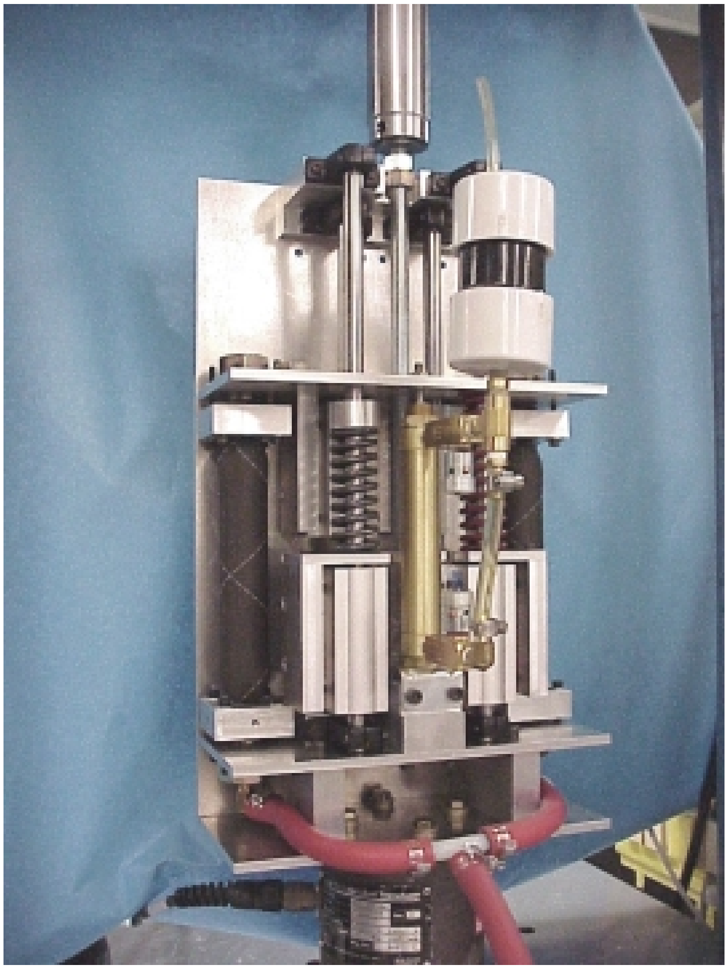

Figure 7.3: Off center view of artificial muscle and tendon test setup.

Experimental Results

The experimental results are shown in figure 7.4 for each of the pressures tested. The output force clearly increases with increasing activation pressure. The observed force is a function of the square of the velocity, decreasing with higher concentric velocities and increasing with higher eccentric velocities. The output force is also a monotonically increasing function of muscle length.

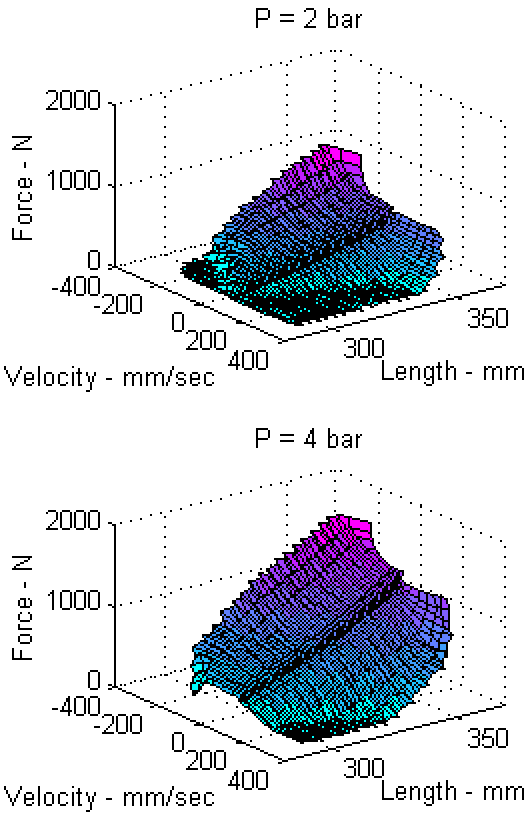

Figure 7.4: Experimental results for activation pressures of 2, 3, 4, and 5 bar.

Experimental Discussion

Comparing the model predictions (figure 7.1) and the experimental results (figure 7.4), a number of significant points can be made. Clearly evident is the effect of the hydraulic damper's lipseal friction discussed in chapter 4. This directionally dependent frictional force is on the order of 20 to 30 N and can be seen in figure 7.4 as a step along the zero-velocity plane. While the output force with respect to length was as predicted, there are several discrepancies with respect to velocity. At high concentric velocities, the output force was higher than predicted near the resting length due to the difficulty of achieving the commanded step input (discussed in chapter 4). Similarly, at high eccentric velocities, the output force was lower than predicted for the same reason. While this discrepancy arises from the test instrument performance, it is worth noting that biological systems also fail to achieve instantaneous performance.

To directly compare the results with the model predictions, both are plotted in figure 7.5. For much of the eccentric conditions, the output force is nearly the same as predicted. However, for the concentric contractions, the output force was less than predicted. Fortunately, the shape of the concentric portion of the curve (more clearly seen in figures 7.1 and 7.4) is as desired.

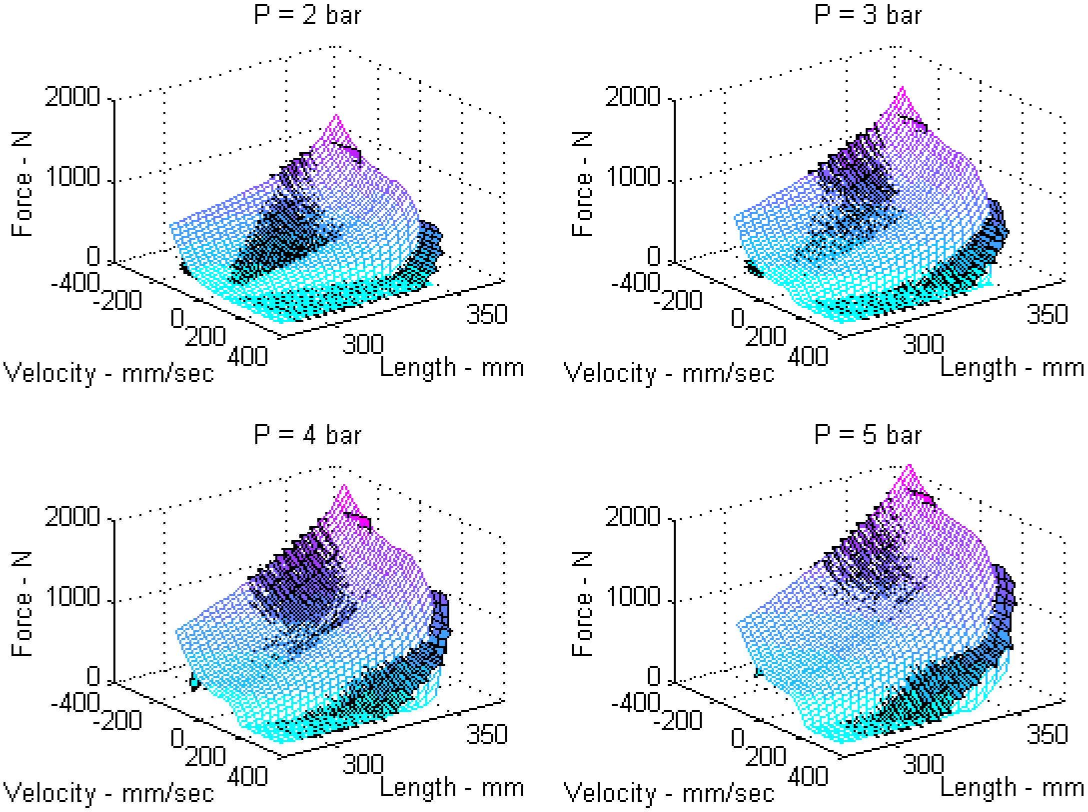

Figure 7.5: Experimental results superimposed on the model predictions.

For the 5 bar test condition (lower right of figure 7.5), force versus velocity has been plotted at three different muscle-tendon lengths (310, 330, and 350 mm) and is shown in figure 7.6. The lipseal friction is clearly evident for each length at zero velocity. The model matches the experimental more closely for the longer lengths (330 and 350 mm), but there is some deviation at the 310 mm length.

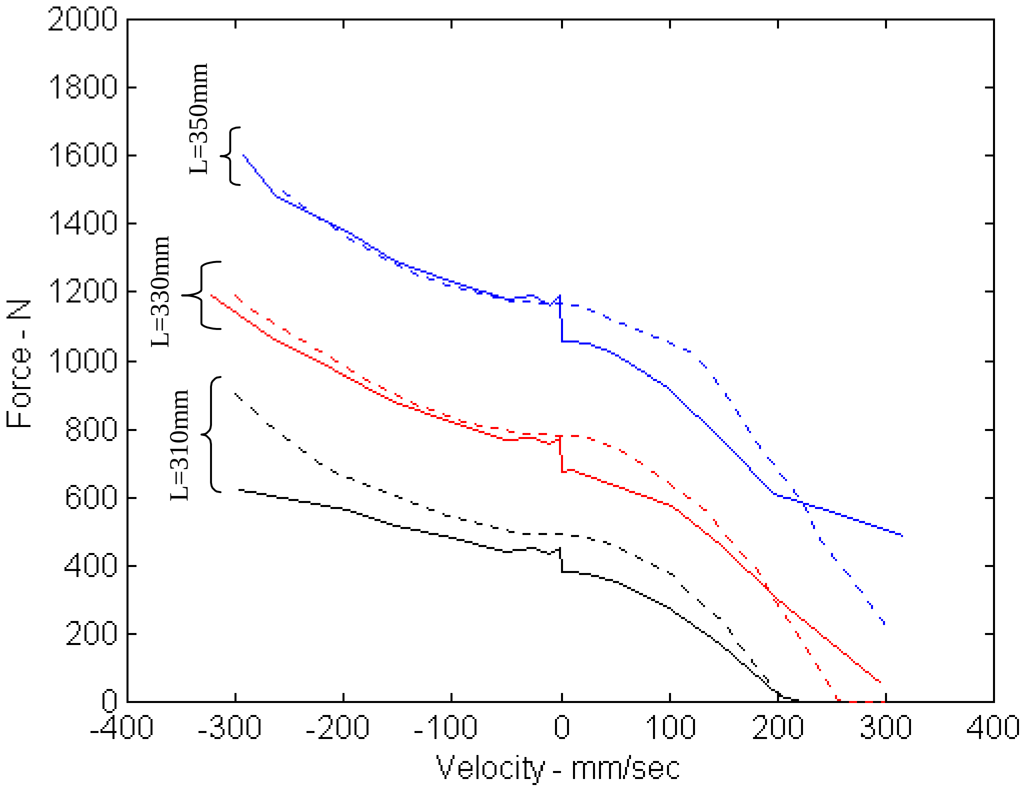

Figure 7.6: Force versus velocity experimental results (solid lines) plotted with model predictions (dotted lines) at 5 bar for three muscle-tendon lengths (310, 330, and 350 mm).

Summary

A first order approximation to biological muscle as been achieved by the artificial musculo-tendon system. The output force of the physical hardware was as predicted and reasonably close to that of biological muscle.

Chapter 8: Work Loop Studies

Of the various functions that biological muscle performs, the ability to do work by operating against a load is certainly the most important. The work done by the muscle, and the rate at which muscle can do work (i.e. its power output), can be calculated from the force-length-velocity relationship. However, the work predicted from a Hill-like model typically overestimates the sustainable amount of work performed by biological muscle (Josephson, 1993). This arises for a number of reasons:

(1) In practice, muscle often functions in repeated stretch-shortening cycles observed during running, swimming, or flying. During the shortening portion of this periodic cycle, muscle does work on the environment. However, during the stretch portion of the cycle, the environment or an antagonistic muscle must do work on the muscle to lengthen it. The work to stretch the muscle can be simply due to mechanical factors such as natural damping in passive tissues or arise from muscle remaining partially (or fully) activated during lengthening. Under these circumstances, the net work done over the whole cycle can be much less than that during shortening alone.

(2) Hill models predict maximal power output at about 0.3 times peak contractile velocity, but realistic trajectories never hold velocity, length, and activation constant. As a result, model predictions may be reliable for peak estimates under isokinetic conditions, but not for the repeated, variable velocity profiles observed *in-vivo* (e.g. Monti et al., 1999 and shown in figure 2.7).

(3) Muscle activation and relaxation is not instantaneous with the beginning and end of the shortening displacement of a stretch-shortening cycle. This phase lag results in lower net work. Furthermore, predicting the activation phase which maximizes work can be difficult (Daniel, 1999).

(4) Muscle activation is often partial, arising from graded excitation. However, models usually assume instantaneous tetanic excitation, and hence over predict the work performed.

In summary, force-length-velocity relationships can be used to predict the maximum work and instantaneous power output of a muscle, but they are not a good measure of the sustainable performance produced during periodic or stretch-shortening cycles. These limitations are what led to the development and subsequent popularity of the work loop technique.

Work Loop Theory

In an effort to determine the sustainable performance produced *in-vivo* during the stretch-shortening cycles of locomotion, a number of investigators have been involved with the development and refinement of the work loop technique (e.g. Machin and Pringle, 1960; Josephson, 1985, 1989, 1993; James et al., 1995; Ettema, 1996; Askew and Marsh, 1997; Full et al., 1998). The technique involves subjecting a muscle to a cyclic length change during appropriate stimulation (see figure 8.1).

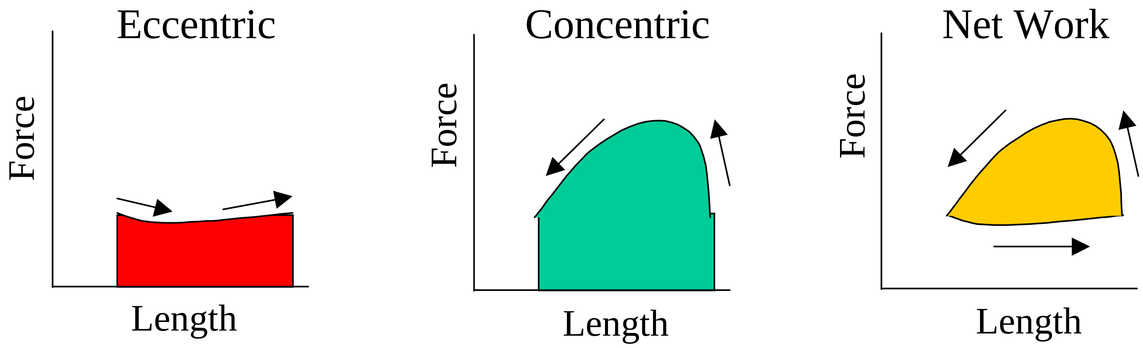

Figure 8.1: A work loop is formed from the stretch-shortening cycle.

The work loop begins with an eccentric contraction where the muscle is stretched from its shortest to longest length. The work done by the environment, or antagonistic muscles, is simply the area under this curve. The cycle continues with a subsequent concentric contraction where the muscle actively contracts from its longest to shortest length. The work done by the muscle is the area under the curve, and for many cases, is greater than the work required to stretch the muscle. The loop area, and hence the net work done over the complete cycle, is the difference between the work done by the muscle during the concentric phase and the work done by the environment (or antagonistic muscles) during the eccentric phase.

As might be expected, there are a number of factors that affect the power output measured in work loop investigations. These factors include:

(1) The *in-vitro* or *in-vivo* experimental methods (i.e. experimental preparation, bathing solution etc.),
(2) The cycle frequency or velocity,
(3) The cycle trajectory (square, sawtooth, sinusoidal, or simulation of *in-vivo* movement, etc.),
(4) The average muscle length upon which the length change or strain is superimposed,
(5) Stimulation phase and pattern within a stretch-shortening cycle,
(6) Which cycle in a repeated series selected for analysis (i.e. fatigue factors),
(7) Muscle temperature (a very significant factor), and
(8) Differences arising between muscles of different species as well as between different muscles within a species.

Typically, some of these parameters are selected such that *in-vivo* conditions are mimicked as closely as possible. The other parameters are either chosen arbitrarily or varied in an effort to obtain the values that result in maximal performance. Not surprisingly, biological muscle exhibits a tremendous variability. Josephson (1993, his table 1) tabulated the results from numerous investigators attempting to experimentally measure muscle work. He found the instantaneous maximum power during isotonic contractions varied from 7 to 500 W/kg, while the sustainable power output using the work loop approach was from less than 5 to over 150 W/kg.

Artificial Musculo-tendon Work Loop Measurements

Using the artificial musculo-tendon system, a number of experiments were conducted using the work loop technique. The experiments were conducted using the axial-torsional Bionix™ (MTS Systems Corp., Minnesota, U.S.A.) tensile testing instrument (see figures 7.2 and 7.3). The test set-up was identical to that used to measure the force-length-velocity relationships in chapter seven. Again, the artificial musculo-tendon system consisted of two McKibben actuators (3/4 in. nominal braid diameter with a resting length of 250 mm) which were both placed parallel the hydraulic damper. These items were then placed in series with the two-spring artificial tendon. Actuation pressures were 2, 3, 4, and 5 bar and applied through a pressure vessel whose volume was significantly larger than the actuators (described in chapter three). A pneumatic servo-regulator (Festo Corporation, Germany, model number MP3-1/8) was used to apply and release pressure upon command.

A square velocity trajectory was selected as shown in figure 8.2. Other trajectories, such as sinusiodal and sawtooth, have been applied to biological muscle, but lower power outputs were observed in comparison to the square wave (Josephson, 1989; Askew and Marsh, 1997). The concentric and eccentric contraction velocities were 1, 10, 25, 50, 100, 150, 200, 250, and 300 mm/s.

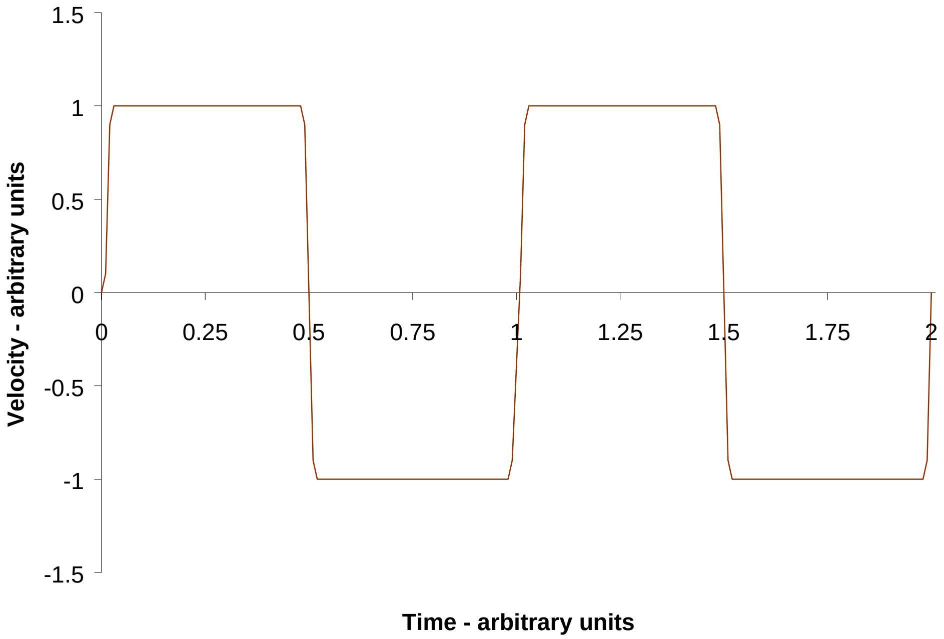

Figure 8.2: Square velocity trajectory selected for work loop experiments.

Two different stimulation profiles were selected. The first profile, concentric activation, applied pressure to the artificial muscle only during the concentric phase of the stretch-shortening cycle (see figure 8.3). Pressure was vented to atmospheric during the eccentric phase of the cycle.

The second profile, eccentric activation, applied pressure to the artificial muscle only during the eccentric phase of the stretch-shortening cycle (see figure 8.4). Pressure was vented to atmospheric during the concentric phase of the cycle.

Concentric Activation Results

The results of the concentric activation tests are shown in figure 8.5. The plot in the upper left is for a stretch-shortening cycle with a square velocity trajectory of 1 mm/sec. As the muscle was passively stretched during the eccentric phase, near zero force was recorded. Upon reaching its maximum length, the artificial muscle was activated to the specified pressure (2, 3, 4, or 5 bar). The force rapidly increased and the muscle began to actively contract. As the muscle shortened, the force decreased until the end of its contraction range was reached. This direction of this counter-clockwise work loop cycle is shown with arrows in figure 8.5.

The plot in the upper right of figure 8.5 follows a similar loop, but at a faster velocity of 50 mm/sec. At the beginning of the eccentric phase, the muscle takes some time to completely relax and achieve near zero force. Similarly, at the beginning of the concentric phase, the muscle takes some time to reach its maximum force.

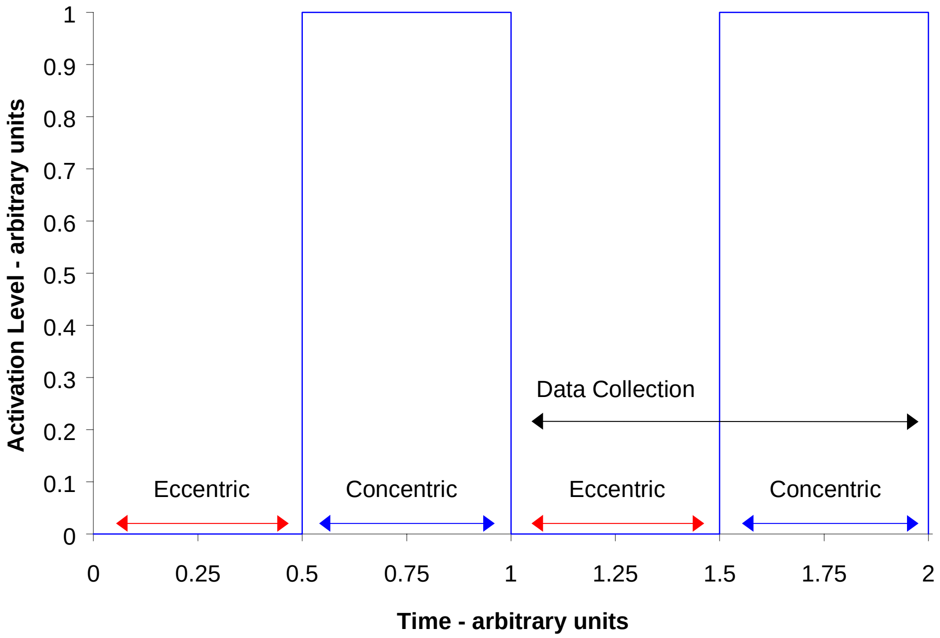

Figure 8.3: Concentric activation profile stimulates the artificial muscle during the concentric phase of the stretch-shortening cycle and allows it to relax during the eccentric phase.

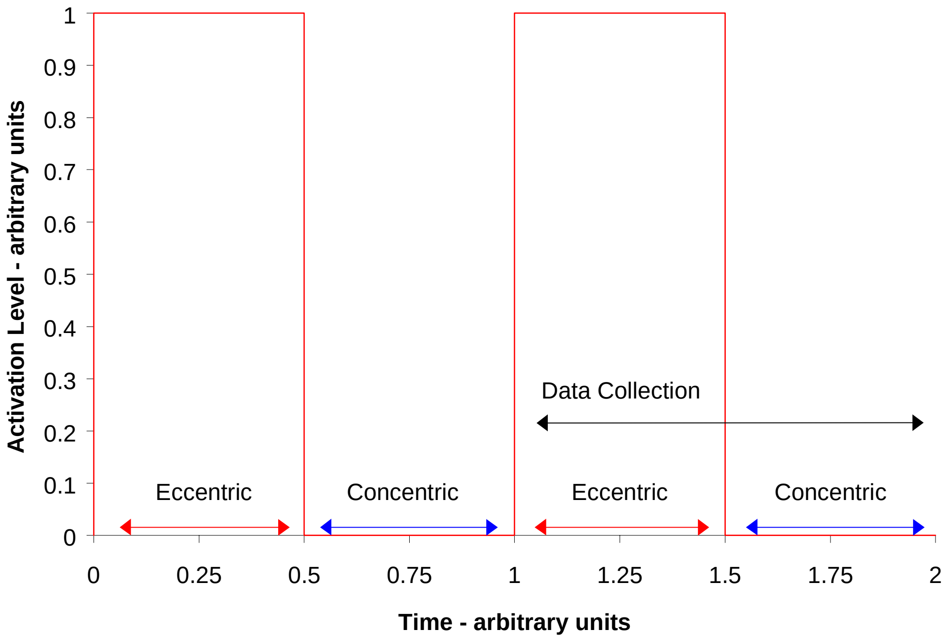

Figure 8.4: Eccentric activation profile stimulates the artificial muscle during the eccentric phase of the stretch-shortening cycle.

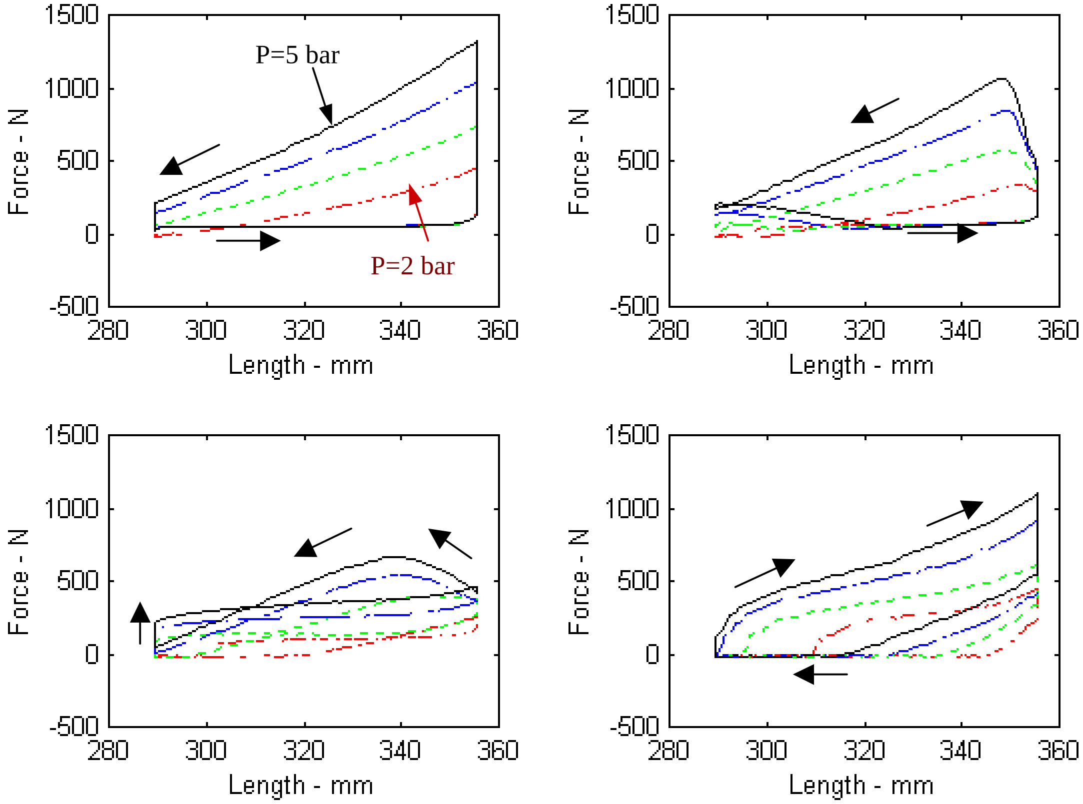

Figure 8.5: Concentric activation work loops for stretch-shortening cycles. Velocity profiles shown are step inputs at 1 mm/sec (upper left), 50 mm/sec (upper right), 100 mm/sec (lower left), and 200 (lower right). Activation pressures of 2 and 5 bar labeled in the upper left with proportional pressures of 3 and 4 bar in-between but unlabeled.

For the faster velocity of 100 mm/sec, shown in the lower left of figure 8.5, the actuator force takes a significant amount of time to relax at the beginning of the eccentric phase and does not achieve zero force for the highest pressure of 5 bar. Lower pressures do achieve complete relaxation, but only for a short period of time. However, the work loop cycle now forms a “figure eight” and indicates the concentric activation profile does both positive and negative work. At 200 mm/sec, shown in the lower right of figure 8.5, the actuator never completely relaxes and the work loop (shown with arrows) forms a clockwise loop in which no positive work is done.

The net work for each of the velocities tested is provided in figure 8.6 and table 8.1. The maximum positive net work of 43.7 J was achieved with the concentric activation profile was at the highest activation pressure (5 bar) and the lowest velocity (1 mm/sec). The net work was positive for each work loop until velocities of 100 mm/sec. At higher velocities, the negative work that was required to passively stretch the artificial musculo-tendon was greater than the positive work performed during the active concentric contraction.

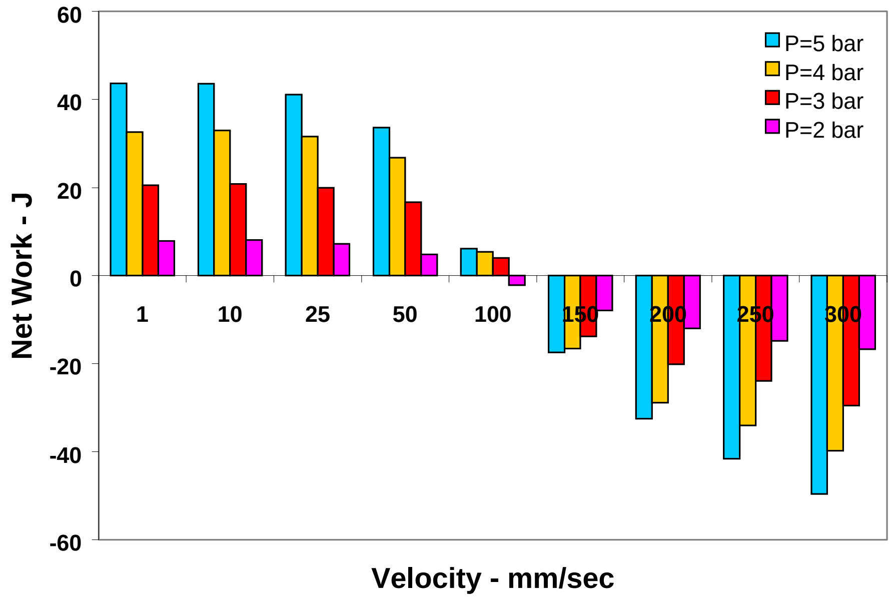

Figure 8.6: Net work (J) performed during isokinetic stretch-shortening cycles using concentric activation.

Table 8.1: Net work (J) performed during the stretch-shortening cycle with concentric activation.

Velocity - mm/s	Pressure - bar			
	2	3	4	5
1	7.9	20.5	32.6	43.7
10	8.1	20.8	33.0	43.6
25	7.2	20.0	31.6	41.1
50	4.8	16.7	26.8	33.6
100	-2.2	4.0	5.4	6.1
150	-7.9	-13.8	-16.6	-17.4
200	-12.0	-20.1	-28.9	-32.5
250	-14.8	-23.9	-34.0	-41.6
300	-16.7	-29.5	-39.8	-49.6

Concentric Activation Discussion

Positive work is done by the artificial musculo-tendon system at velocities less than 100 mm/sec for all pressure activation conditions tested. However, at 100 mm/sec, the net work starts to become negative. At velocities of 150 mm/sec and higher, the work required to stretch the system was greater than that done by the actuator, resulting in a negative net work for all pressure conditions. Even though the actuator is being vented to atmospheric pressure during the eccentric phase, the force increases. This result occurs because the actuator is being lengthened while some residual pressure remains and because of the system's damping.

Chou and Hannaford (1996) performed a variation of the work loop technique on a smaller McKibben actuator (1/2 in. nominal braid diameter with a resting length of 155 mm) at a pressure of 5 bar. The work performed during a concentric activation, shorten-stretch cycle under quasi-static conditions was 2.59 J. The lowest velocity test condition (1 mm/s) could be considered equivalent to Chou and Hannaford's (1996) quasi-static test, but the results are not directly comparable as their actuator had a smaller nominal diameter and shorter resting length.

Eccentric Activation Results

The results of the eccentric activation tests are shown in figure 8.7. The plot in the upper left is for a stretch-shortening cycle with a square velocity trajectory of 1 mm/sec. As the muscle was actively stretched during the eccentric phase, the force rapidly increased from near zero to maximum for the pressure, velocity, and length conditions. At the end of the eccentric phase, the artificial muscle pressure was vented to atmospheric and near zero force was rapidly obtained for the concentric portion of the cycle. As the testing instrument shortened the passive artificial muscle, the force remained near zero until the cycle was complete. The direction of this clockwise work loop cycle is shown with arrows in figure 8.7.

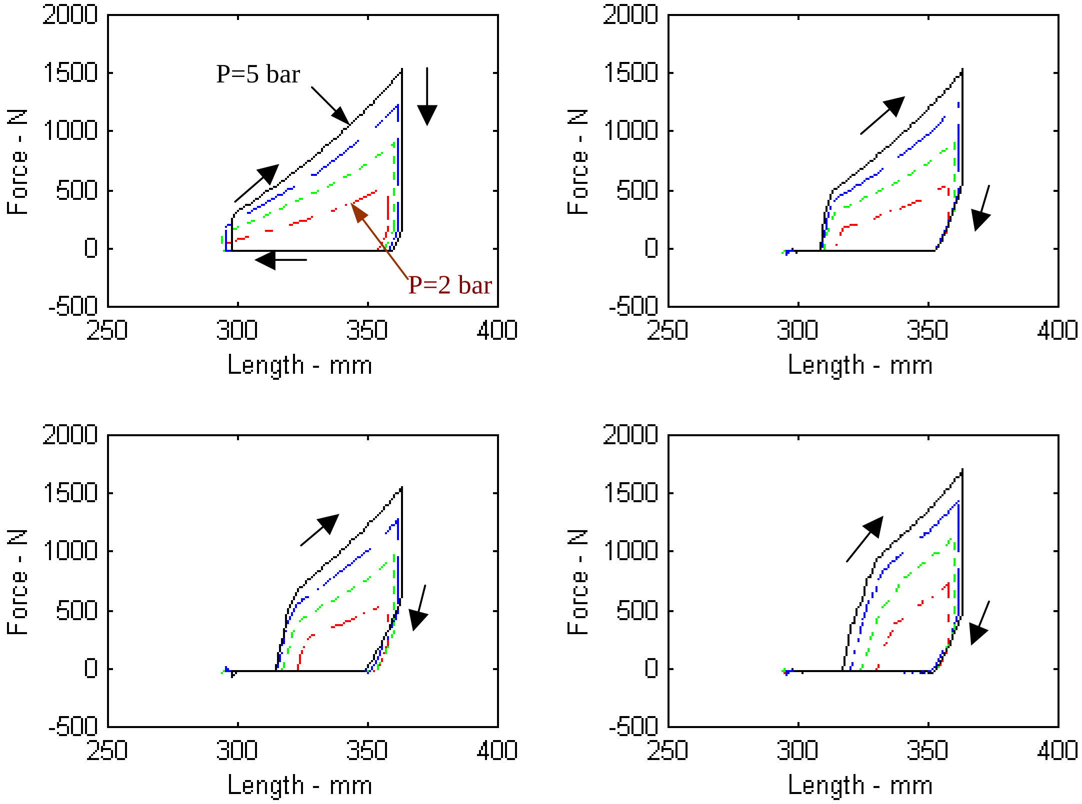

Figure 8.7: Eccentric activation work loops for stretch-shortening cycles. Velocity profiles shown are step inputs at 1 mm/sec (upper left), 50 mm/sec (upper right), 100 mm/sec (lower left), and 200 (lower right). Activation pressures of 2 and 5 bar are shown in the upper left with proportional pressures of 3 and 4 bar in between but unlabeled.

For a faster velocity of 50 mm/sec, the plot in the upper right of figure 8.7 follows a similar loop, but the force remains at near zero for a period of time prior to ramping up during the active eccentric phase. During the passive concentric phase, the muscle quickly relaxes to near zero force.

For the faster velocity of 100 mm/sec, shown in the lower left of figure 8.7, the actuator force again does not immediately ramp up and nor ramp down at the beginning of the eccentric and concentric phases respectively. This also occurs at even faster velocities (e.g. 200 mm/sec) as shown in the lower right of figure 8.7.

The net work for each of the velocities tested is provided in figure 8.8 and table 8.2. The maximum negative net work of 56.7 J was achieved with the eccentric activation profile at the highest activation pressure (5 bar) and the lowest velocity (1 mm/sec). The net work remained negative for all the test conditions, however, its magnitude first decreased in increasing velocity, and then increased.

Eccentric Activation Discussion

Negative net work is done by the artificial musculo-tendon system for all velocities and pressure conditions tested. Not surprisingly, higher pressures yielded higher negative net work as shown in figure 8.8 and table 8.2. Interestingly, the work began to decrease with increasing velocity and then increase. This most likely arises from the increasing amount of work required to move the damper as the damper force increases with the square of the velocity.

Summary

The experimental results presented in this chapter indicates the artificial musculo-tendon system can perform work on the environment as well as allow the environment (or antagonistic muscles) to perform work on it. As muscles are often used to both accelerate an animal during locomotion and decelerate it, these results provide a measure of functional capacity.

Clinical interpretation of these results is difficult. Gitter and others (1991) reported the ankle musculature contributed 36 J of energy to locomotion for each step in the gait cycle. However, the origin-insertion velocity of the *triceps surae* during the gait cycle is far from the isokinetic profiles used in the work loop studies here. However, the data reported in tables 8.1 and 8.2 can be used as benchmark data for comparing alternative approaches to an artificial muscle as well as improvements to the design presented here. The square velocity trajectory and the concentric or eccentric activation profiles, also square waves with no phase lag or lead, can be easily duplicated by other investigators.

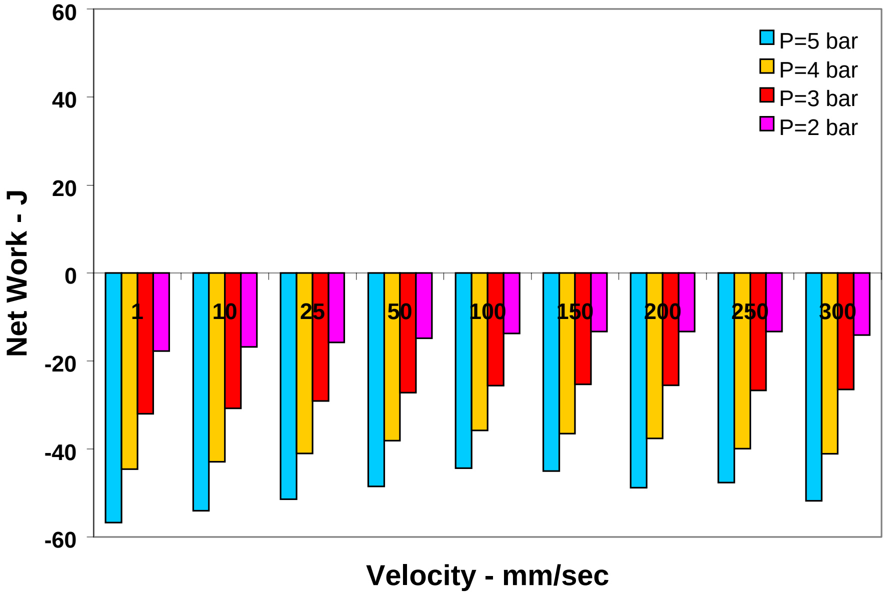

Figure 8.8: Net work (J) performed during isokinetic stretch-shortening cycles using eccentric activation.

Table 8.2: Net work (J) performed during the stretch-shortening cycle with eccentric activation.

Velocity - mm/s	Pressure - bar			
	2	3	4	5
1	-17.7	-32.0	-44.6	-56.7
10	-16.8	-30.7	-42.9	-54.0
25	-15.8	-29.1	-41.0	-51.4
50	-14.8	-27.2	-38.1	-48.5
100	-13.7	-25.6	-35.8	-44.4
150	-13.3	-25.3	-36.5	-45.0
200	-13.3	-25.5	-37.6	-48.8
250	-13.3	-26.7	-39.9	-47.6
300	-14.1	-26.5	-41.1	-51.8

Chapter 9: Conclusions

Biorobotic research seeks to develop new robotic technologies based on human and animal properties. The development of one component of such a system, an artificial muscle and tendon, is documented here. The device is based on existing knowledge of neuromuscular physiology and biomechanics and is designed to mimic the function of the human *triceps surae*. Known static and dynamic properties are extracted from the literature and used to mathematically describe the unique force, length, and velocity properties of biological muscle. As biological muscle exhibits wide variation in performance, ranges are identified which encompass typical behavior.

One candidate for the contractile element of an artificial muscle and tendon, a McKibben pneumatic actuator, is presented and a current model of the actuator is extended to include the material properties of the actuator's inner bladder as well as frictional effects. This model is then experimentally validated where it is shown the force-length properties are muscle-like, but the force-velocity properties are not. The addition of a hydraulic damper is proposed to improve the actuators velocity-dependent properties resulting in a more muscle-like system. The theoretical design for a hydraulic damper is then presented with computer simulations demonstrating the expected performance to be within the range identified as acceptable. Experimental tests were conducted to validate the theoretical assumptions used in development and the results meet expectations.

To provide appropriate connective tissue between the artificial muscle and its skeleton, the properties of tendons are examined in detail for the purposes of designing an artificial tendon. In particular, the properties of weight-bearing tendons, suspected to store significant amounts of energy during locomotion, are extracted from the literature and compared with a number of existing tendon models. A mathematical model for an energy-storing tendon is proposed and a range of acceptable performance is identified. Noting that offset linear springs arranged in parallel can achieve tendon-like performance, a design is proposed that maximizes performance while minimizing a weight penalty. A series of experimental tests verifies that the design provides suitable tendon-like performance.

A complete model of the artificial musculo-tendon system is then used to predict the expected force-length-velocity performance. The physical system was then assembled and subjected to numerous performance tests. The results exhibited muscle-like performance in general: higher activation pressures yielded higher output forces, faster concentric contractions resulted in lower force outputs, faster eccentric contractions produced higher force outputs, and output forces were higher at longer muscle lengths than shorter lengths. Several areas could be improved such as the shape of the concentric and eccentric surfaces (concave versus convex) and reduction of dynamic friction, particularly at low velocities.

The ability of the artificial musclo-tendon system to perform work is then examined. While knowledge of the force-length-velocity relationship provides data for calculating biological muscle's instantaneous work and power output, it greatly over-predicts capability to perform sustained activities such as locomotion. This shortcoming has lead to the development of the work loop technique that was used to experimentally measure the performance of the artificial system during stretch-shortening cycles. Two activation profiles were examined. The first profile activated the artificial muscle during the concentric phase and allowed it to relax during the eccentric phase. This profile maximized the positive work output at low velocities, but due to an activation-to-force-production lag and an increase in force produced by the damper, work output decreased at higher velocities. The second profile activated the muscle only during the eccentric phase. This profile maximized the negative work at low velocities, followed by a reduction in work at intermediate velocities, and then higher negative work at high velocities. Again, this was due to the effects of lag and velocity-dependent damping forces.

In conclusion, both a model and physical hardware that mimics the performance of a specific biological muscle group, the human *triceps surae*, is demonstrated.

Suggestions for Further Research

This first generation artificial musculo-tendon system provides a wealth of opportunity for future research. Investigations can be made into the many refinements that might improve its performance as well the innumerable applications that could use such a device.

Regarding performance improvements, the force-length properties of the actuator might be improved by using elastic outer braid fibers in the McKibben actuator. A non-linear fiber material, in combination with the inherent contraction ratio related changes in braid angle, might yield the desired parabolic force-length relationship as well as allow elongation beyond the initial resting length.

The shape of the force-velocity curve could be improved with the development of either a servo-controlled valve or a flexible orifice whose diameter changes as a function of pressure. The servo-controlled valve and feedback loop could be used to precisely mimic the desired force-velocity relationship of both concentric and eccentric contractions, albeit at the cost of additional complexity. However, an orifice made from an elastic material might be able to improve the performance using a passive rather than active approach.

The performance of the artificial tendon can be improved with the current design approach, but only at the cost of additional springs (i.e. a weight penalty. However, lightweight polymer springs might better mimic the toe region of the stress-strain curve through the use of non-linear elastic materials. Such an approach might improve performance while reducing the system’s weight.

The artificial muscle presented here was developed to mimic the performance of the muscles within the human *triceps surae*. However, there are numerous additional muscles for which a design study could identify the appropriate fixed orifice sizes, cylinder dimensions, and McKibben actuator sizes.

Perhaps the most prominent area for improving performance involves the development of a theoretical model relating the output force rise and fall profiles to time of activation. Such a model would be dependent on the muscle size, its contraction ratio, its activation pressure, as well as components of the pneumatic system. However difficult, combining this model with the models of the McKibben actuator, the hydraulic damper, and artificial tendons could result in accurate predictions of the parameters (e.g. activation trajectories within the stretch-shortening cycle) for which output work and power can be maximized.

Regarding the applications that could use such a device, reducing the weight of the system would certainly be important for applications in robotics and prosthetics. A double acting cylinder would eliminate the need for the ballast chamber and plastic hydraulic fittings could replace the heavier brass ones used in the prototype. Substituting plastic for aluminum in the custom machined actuator end fittings would also reduce the system weight as would replacing the adjustable orifice valves with fixed orifices. Non-linear polymer springs could be used as replacements for the heavy die springs used for the tendon. The prototype also used four linear bearings, but an effective design could be realized with only three, further reducing weight. The bearing shafts could also be used as a structural load path in an application, eliminating the need for a prosthetic limb pylon or robotic “skeleton.”

Lastly, this unique artificial muscle-tendon system could serve as an actuator in numerous different applications yet to be explored. Potential applications include: personal robotics, automation devices that share the work space with humans, entertainment robots, service robots for the elderly, tele-operated devices, and systems that extend or augment human capabilities are but a few of the possibilities.

Bibliography

Abbott, B. C. and Wilkie, D. R., 1953. The relation between velocity of shortening and the tension-length curve of skeletal muscle. Journal of Physiology, 120:214-22.

Albus, J. S., 1990. Robotics: where has it been? Where is it going? *Robotics and Autonomous Systems* 6(3):199-219.

Alexander, R. McN. and A. Vernon, 1975. The dimensions of knee and ankle muscles and the forces they exert. *Journal of Human Movement Studies*, 1:115-123.

Alexander, R. McN., Maloiy, G. M. O., Ker, R. F., AS Jayes, and CN Warui, 1982. The role of tendon elasticity in the locomotion of the camel (*Camelus dromedarius*), *J. Zoology, London*, 198:293-313.

Anonymous, 1998. Robot population and applications rise. *Design News*, May 18, 1998.

Askew, G. N. and Marsh, R. L., 1997. The effects of length trajectory on the mechanical power output of mouse skeletal muscles. *Journal of Experimental Biology*, 200:3119-3131.

Bahler, A. S., 1967. Series elastic component of mammalian skeletal muscle. *American Journal of Physiology*, 213(6):1560-1564.

Bahler, A. S., 1968. Modeling of mammalian skeletal muscle. *IEEE Transactions of Bio-Medical Engineering*, BME-15(4):249-257.

Bennett, M. B., Ker, R. F., Dimery, N. J., and Alexander, R. McN., 1986. Mechanical properties of various mammalian tendons. *Journal of Zoology, London*, A209:537-548.

Bobbert, M. F. and van Ingen Schenau, G. J., 1990. Isokinetic plantar flexion: experimental results and model calculations. *Journal of Biomechanics*, 23(2):105-119.

Bobbert, M. F., Huijing, P. A., and van Ingen Schenau, G. J., 1986. A model of the human triceps surae muscle-tendon complex applied to jumping. *Journal of Biomechanics*, 19(11):887-898.

Bouaziz, Z., Bouaziz, M., and M. Hugon, 1975. Modulation of soleus electromyogram during electrical stimulation of medial gastrocnemius nerve in man. *Electromyography and Clinical Neurophysiology*, 15(1):31-41.

Cai, D. and Yamaura, H., 1996. A robust controller for a manipulator driven by artificial muscle actuator. *Proceedings, 1996 IEEE International Conference on Control Applications*, Dearborn, MI, pp. 540-545.

Chou, C. P. and Hannaford, B., 1996. Measurement and modeling of artificial muscles. *IEEE Transactions on Robotics and Automation,* 12:90-102.

Cocatre-Zilgien, J. H., Delcomyn, F. and Hart, J. M., 1996. Performance of a muscle-like “leaky” pneumatic actuator powered by modulated air pulses. *Journal of Robotic Systems*, 13(6):379-390.

Cook, G. and Stark, L., 1968. The human eye movement mechanism: experiments, modelling and model testing. *Arch. Opthal.*, 79:428-436.

Ejiri, M., 1996. Towards meaningful robotics for the future: are we headed in the right direction? *Robotics* *and Autonomous Systems* 18(1-2):1-5.

Ettema, G. J. C., 1996. Mechanical efficiency and efficiency of storage and release of series elastic energy in skeletal muscle during stretch-shorten cycles. *Journal Experimental Biology*, 199:1983-1997.

Fox, R. W. and McDonald, A. T., 1985. Introduction to Fluid Mechanics, third edition. John Wiley and Sons, New York, N. Y.

Franklin, S., 1997. Artificial Minds. MIT Press, Cambridge, MA.

Frisen, M., Magi, M., Sonnerup, L., and Viidik, A., 1969. Rheological analysis of soft collagenous tissue. Part I: theoretical considerations. *Journal of Biomechanics*. 2:13-20.

Full, R. J., Stokes, D. R., Ahn, A. N., and Josephson, R. K., 1998. Energy absorption during running by leg muscles in a cockroach. *Journal of Experimental Biology*, 201:997-1012.

Gavrilovic, M. M. and Maric, M. R., 1969. Positional servo-mechanism activated by artificial muscles. *Medical and Biological Engineering*, Vol. 7, pp. 77-82.

Gaylord, R. H., 1958. Fluid actuated motor system and stroking device. United States Patent 2,844,126.

Gitter, A., Czerniecki, J. M., and DeGroot, D. M., 1991. Biomechanical analysis of the influence of prosthetic feet on below-knee amputee walking. *American Journal of Physical Medicine and Rehabilitation*, 70(3):142-148.

Gordon, A. M., Huxley, A. F., and Julian, F. J., 1966. The variation in isometric tension with sarcomere length in vertebrate muscle fibres. *Journal of Physiology, London*, 184:170-192.

Gregor, R. J., Roy, R. R., Whiting, W. C., Lovely, R. G., Hodgson, J. A., and Edgerton, V. R., 1988. Mechanical output of the cat soleus during treadmill locomotion: *in vivo* vs *in situ* characteristics. *Journal of Biomechanics*, 21(9):721-732.

Harris, E. H., Walker, L. B., and Bass, B. R., 1966. Stress-strain studies in cadaveric human tendon and an anomaly in the Young's modulus thereof. *Medicine and Biology in Engineering*, 4:253-259.

Hatze, H., 1981. Myocybernetic control models of skeletal muscle. University of South Africa, Pretoria.

Herrick, W. C., Kingsbury, H. B., and Lou, D. Y. S., 1978. A study of the normal range of strain, strain rate, and stiffness of tendon. *Journal of Biomedical Materials Research*, 12:877-894.

Hill, A. V., 1938. The heat of shortening and the dynamic constants of muscle. *Proceedings of the Royal Society, London*, B126:136-195.

Hill, A. V., 1953. The mechanics of active muscle. *Proceedings of the Royal Society, London*, B195:50-53.

Hof, A. L., Geelen, B. A., and van den Berg, J. W., 1983. Calf muscle moment, work and efficiency in level walking; role of series elasticity. *Journal of Biomechanics*, 16(7):523-537.

Hof, A. L. and van den Berg, J. W., 1981a. Emg to force processing I: an electrical analogue of the Hill muscle model. *Journal of Biomechanics*, 14(11):747-758.

Hof, A. L. and van den Berg, J. W., 1981b. EMG to force processing. II: estimation of parameters of the

Hill muscle model for the human triceps surae by means of a calf-ergometer. *Journal of Biomechanics*, 14:759-770.

Hof, A. L., 1998. *In vivo* measurement of the series elasticity release curve of human triceps surae muscle. *Journal of Biomechanics*, 31:793-800.

Hoy, M. G., Zajac, F. E., and Gordon, M. E., 1990. A musculoskeletal model of the human lower extremity: the effect of muscle, tendon, and moment arm on the moment-angle relationship of musculotendon actuators at the hip, knee, and ankle. *Journal of Biomechanics*, 23(2):157-169.

Huxley, A. F., 1957. Muscle structure and theories of contraction. *Progress in Biophysics and Biophysical Chemistry*, 7:257-318.

Inoue, K., 1987. Rubbertuators and applications for robots. *Proceedings, 4th Symposium on Robotics Research*, Tokyo, pp. 57-63.

James, R. S., Altringham, J. D., and Goldspink, D. F., 1995. The mechanical properties of fast and slow skeletal muscles of the mouse in relation to their locomotory function. *Journal of Experimental Biology*, 198:491-502.

Josephson, R. K., 1985. Mechanical power output from striated muscle during cyclic contraction. *Journal of Experimental Biology*, 114:493-512.

Josephson, R. K., 1989. Power Output from skeletal muscle during linear and sinusoidal shortening. *Journal of Experimental Biology*, 147:533-537.

Josephson, R. K., 1993. Contraction dynamics and power output of skeletal muscle. *Annual Reviews in Physiology*, 55:527-546.

Joyce, G. C., Rack, P. M., and Westbury, D. R., 1969. The mechanical properties of the cat soleus muscle during controlled lengthening and shortening movements. *Journal of Physiology*. 204:461-474.

Ker, R. F., 1978. Dynamic tensile properties of the plantaris tendon of sheep (Ovis aries). *J. Exp. Biol.*, 93:283-302.

Ker, R. F., Alexander, R. McN., and Bennett, M. B., 1988. Why are mammalian tendons so thick? *Journal of Zoology, London*, 216:309-324.

Ker, R. F., Dimery, N. J., and Alexander, R. McN., 1986. The role of tendon elasticity in hopping in a wallaby (*Macropus rufogriseus*). *J. Zoology, London* Series A, 208:417-428.

Kitano, H., Fujita, M., Zrehen, S., and Kageyama, K., 1998. Sony legged robot for RoboCup challenge. *Proceedings, 1998 IEEE International Conference on Robotics and Automation*, New York, NY, Vol. 4, pp. 2605-2612.

Klute, G. K. and Hannaford, B., 1998a, "Fatigue characteristics of McKibben artificial muscle actuators," *Proceedings, IEEE/RSJ 1998 International Conference on Intelligent Robotic Systems (IROS '98)*, Victoria BC, Canada, Vol. 3, pp. 1776-1781.

Klute, G. K. and Hannaford, B., 1998b, "Modeling pneumatic McKibben artificial muscle actuators:

approaches and experimental results," Submitted for review, *Journal of Dynamic Systems, Measurements, and Control*, November 1998, revised May 1999.

Komi, P. 1990. Relevance of in vivo force measurements to human biomechanics. *Journal of Biomechanics*, 23(Suppl. 1):23-34.

Lehman, S. L., 1990. Input identification depends on model complexity. In: Winters, J. M. and Woo, S. L-Y. (eds), Multiple Muscle Systems: Biomechanics and Movement Organization, Springer-Verlag, New York, NY, pp. 94-100.

Lewis, G. and Shaw, K. M. 1997. Tensile properties of human tendo achillis: effect of donor age and strain rate. *Journal of Foot and Ankle Surgery*, 36(6):435-445.

Machin, K. E. and Pringle, J. W. S., 1960. The physiology of insect fibrillar muscle. III. The effect of sinusiodal changes of length on a beetle flight muscle. *Proceedings of the Royal Society, London, Serial B.*, 152:311-330.

McCrorey, H. L., Gale, H. H., and Alpert, N. R., 1966. Mechanical properties of the cat tenuissimus muscle. *American Journal of Physiology*, 210:114-120.

Medrano-Cerda, G. A., Bowler, C. J., and Caldwell, D. G., 1995. Adaptive position control of antagonistic pneumatic muscle actuators. *Proceedings, 1995 IEEE/RSJ International Conference on Intelligent Robots and Systems (IROS '95)*, Pittsburgh, PA, Vol. 1, pp. 378-383.

Medrano-Cerda, G. A., Bowler, C. J., and Caldwell, D. G., 1995. Adaptive position control of antagonistic pneumatic muscle actuators. *Proceedings, 1995 IEEE/RSJ International Conference on Intelligent Robots and Systems (IROS '95)*, Pittsburgh, PA, Vol. 1, pp. 378-383.

Mills, J. W., 1993. Lukasiewicz' insect: the role of continuous-valued logic in a mobile robot's sensors, control, and locomotion. *Proceedings, 23rd International Symposium on Multiple-Valued Logic*, Sacramento, CA, USA, pp. 258-263.

Minns, R. J. and Muckle, D. S., 1982. Mechanical properties of traumatized rat tendo-achilles and the effect of an anti-inflammatory drug on the repair properties. *Journal of Biomechanics*, 15(10):783-787.

Mitwalli, A. H., Denison, T. A., Jackson, D. K., Leeb, S. B. and Tanaka, T., 1997. Closed-loop feedback control of magnetically-activated gels. *Journal of Intelligent Material Systems and Structures*, Vol. 8, No. 7, pp. 596-604.

Mojarrad, M. and Shahinpoor, M., 1997. Ion-exchange-metal composite artificial muscle actuator load characterization and modeling. *Proceedings, 1997 SPIE Conference on Smart Structures and Materials*, San Diego, CA, USA, Vol. 3040, pp. 294-301.

Monti, R. J., Roy, R. R., Hodgson, J. A., and Edgerton, V. R., 1999. Transmission of forces within mammalian skeletal muscles. *Journal of Biomechanics*, 32:371-380.

Mueller, M. J., Minor, S. D., Schaaf, J. A., Strube, M. J., and Shahrmann, S. A., 1995. Relationship of plantar-flexor peak torque and dorsi-flexion range of motion to kinetic variables during walking. *Physical Therapy*, 75(8):684-693.

Murray D, 1959. A father's helping hand. *Today's Health*. 37(5):38-39, 55-57, 61.

Nickel, V. L., Perry, J., and Garrett, A. L., 1963. Development of useful function in the severely paralyzed hand. *Journal of Bone and Joint Surgery*, Vol. 45A, No. 5, pp. 933-952.

Paynter, H. M., 1996. Thermodynamic treatment of tug-&-twist technology: Part 1. Thermodynamic tugger design. In: Stelson, K. and Oba, F. (eds): *Proceedings, Japan-USA Symposium on Flexible Automation*, Boston, MA, pp. 111-117.

Rack, P. M., Ross, H. F., Thibmann, A. F. and D. K. Walters, 1983. Reflex responses to the human ankle: the importance of tendon compliance. *Journal of Physiology, London*, 344:503-524.

Ralston, H. J., Polissar, M. J., Inman, V. T., Close, J. R., and B Feinstein, B., 1949. Dynamic features of human isolated voluntary muscle in isometric and free contractions. *Journal of Applied Physiology*, 1(7):526-533.

Riemershma D. J. and Schamhardt, H. C., 1985. In vitro mechanical properties of equine tendons in relation to cross-sectional area and collagen content. *Research in Veterinary Science*, 39:263-270.

Schulte, H. F., 1961. The characteristics of the McKibben artificial muscle. In: *The Application of External Power in Prosthetics and Orthotics*, Publication 874, National Academy of Sciences - National Research Council, Washington DC, Appendix H, pp. 94-115.

Spoor, C. W., van Leeuwen, J. L., Meskers, C. G. M., Titulaer, A. F., and Huson, A., 1990. Estimation of instantaneous moment arms of lower-leg muscles. *Journal of Biomechanics*, 23(12):1247-1259.

ter Keurs, H. E. D. J., Iwazumi, T., and Pollack, G. H., 1978. The sarcomere length-tension relation in skeletal muscle. *Journal of General Physiology*, 72:565-592.

Tondu, B., Boitier, V., and Lopez, P., 1994. Naturally compliant robot-arms actuated by McKibben artificial muscles. *Proceedings, 1994 IEEE International Conference on Systems, Man, and Cybernetics*, San Antonio, TX, Vol. 3, pp. 2635-2640.

Treloar, L. R. G., 1958. The Physics of Rubber Elasticity, Oxford University Press, London.

Trevelyan, J., 1997. Simplifying robotics – a challenge for research. *Robotics and Autonomous Systems*, 21(3):207-220.

Vogel, S., 1994. Life in Moving Fluids, 2nd edition. Princeton University Press, Princeton, N. J.

Voigt, M., Bojsen-Moller, F., Simonsen, E. B., and Dyhre-Poulsen, P., 1995a. The influence of Young's modulus, dimensions, and instantaneous moment arms on the efficiency of human movement. *Journal of Biomechanics*, 28(3):281-291.

Voigt, M., Simonsen, E. B., Dyhre-Poulsen, P., and Klausen, K., 1995b. Mechanical and muscular factors influencing the performance in maximal vertical muping after different prestretch loads. *Journal of Biomechanics*, 28(3):293-307.

Webster, D. A. and Werner, F. W., 1983. Mechanical and functional properties of implanted freeze-dried flexor tendons. *Clinical Orthopaedics and Related Research*, 180:301-309.

Wells, J. B., 1965. Comparison of mechanical properties between slow and fast mammalian muscle. *Journal of Phsiology*, 18:252-269.

Wilkie, D. R., 1950. The relation between force and velocity in human muscle. *Journal of Physiology*, K110:248-280.

Wilkie, D. R., 1956. The mechanical properties of muscle. *British Medical Bulletin*, 12(3):177-182.

Winter, D. A., 1990. The Biomechanics and Motor Control of Human Movement, 2nd edition. John Wiley and Sons, New York, N.Y.

Winters, J. M. and Stark, L., 1985. Analysis of fundamental movement patterns through the use of indepth anatgonistic muscle models, *IEEE Transactions on Biomedical Engineering*, BME-32:826-839.

Winters, J. M., 1990. Hill-based muscle models: a systems engineering perspective. In: Winters, J. M. and Woo, S. L-Y. (eds): Multiple Muscle Systems: Biomechanics and Movement Organization, Springer-Verlag, New York, N. Y., 69-93.

Winters, J. M., 1995. How detailed should muscle models be to understand multi-joint movement coordination? *Human Movement Science*, 14:401-442.

Woittiez, R. D., Huijing, P. A., Boom, H. B. K. and Rozendal, R. H., 1984. A three-dimensional muscle model: a quantified relation between form and function of skeletal muscles. *Journal of Morphology*, 182:95-113.

Woo, S. L. Y., Gomez, M. A., Amiel, D., Ritter, M. A., Gelberman, R. H., and Akeson, W. H., 1981. The effects of exercise on the biomechanical and biochemical properties of swine digital flexor tendons. *Journal of Biomechanical Engineering*, 103:51-56.

Wood, J. E., Meek, S. G., and Jacobsen, S. C., 1989. Quantitation of human shoulder anatomy for prosthetic arm control – I. Surface modeling. *Journal of Biomechanics*, 22(3):273-292.

Yamaguchi, G. T., Sawa, A. G.-U., Moran, D. W., Fessler, M. J., and Winters, J. M., 1990. A survey of human musculotendon actuator parameters. In: Winters, J. M. and Woo, S. L.-Y. (eds), Multiple Muscle Systems: Biomechanics and Movement Organization. Springer-Verlag, New York, N. Y., pp. 717-774.

Yoda, M. and Shiota, Y., 1994. A electromagnetic actuator for a robot working with a man. *Proceedings, 3rd IEEE International Workshop on Robot and Human Communication* (RO-MAN ’94), Nagoya, Japan, pp. 373-377.

Zahalak, G. I., 1990. Modeling muscle mechanics (and Energetics). In: Winters, J. M. and Woo, S. L-Y. (eds): Multiple Muscle Systems: Biomechanics and Movement Organization, Springer-Verlag, New York, N. Y., 1-23.

Zajac, F. E., 1989. Muscle and tendon: Properties, models, scaling, and application to biomechanics and motor control. *CRC Critical Reviews in Biomedical Engineering*, 17(4):359-41.

Vita

Glenn K. Klute

6625 Lakeview Drive #B202
Kirkland, WA 98033
425/889-4464
gklute@u.washington.edu

Bioengineering Dept., Box 352500
University of Washington
Seattle, WA 98195-2500
206/616-4936

http://rcs.ee.washington.edu/brl/people/gklute/

EDUCATION:

University of Washington, Seattle, WA
Ph.D. Candidate in Bioengineering
Degree expected Summer, 1999
Dissertation: Artificial Muscles: Actuators for Biorobotic Systems.

Pennsylvania State University
M.S. in Bioengineering, 1990
Thesis: The Penn State Electric Ventricular Assist Device: Minimum Energy Control Law, Stability, and Implementation.

University of Washington
B.S. in Mechanical Engineering, 1986

EXPERIENCE:

University of Washington
Seattle, WA September 1993 to present

Graduate Research Assistant. Developing lightweight robotic actuators that mimic the neuro-muscular properties of the human limb. Simulations using fluid, lumped parameter, and non-linear finite element models were used to design actuators with force-length-velocity characteristics similar to those predicted by the Hill muscle model. Experimentally validated results were used to optimize hardware design for improved performance and fatigue life characteristics. Current work involves fabrication of actuator hardware and development of biologically based controllers.

NASA Johnson Space Center
Houston, TX April 1991 to September 1993

Director, Anthropometry and Biomechanics Laboratory. Responsible for human performance, anthropometry, and biomechanics in the research areas relating to manned spaceflight. Duties included directing the technical activities of professional laboratory staff (2 Ph.D.'s, 3 M.S.'s, 2 B.S.'s, 1 technician, plus various undergraduate interns). Research tasks encompassed literature reviews, development of scientific proposals, collection of experimental data, and publication of results. Research projects included: cycle ergometer biomechanics in zero-gravity, hand-glove performance tests, isokinetic isolated dynamometry of test subjects wearing various extravehicular and intravehicular pressure suits, astronaut anthropometry, and evaluation of astronaut force and torque capabilities in reduced gravity environments.

KRUG Life Sciences, Inc.
Houston, TX September 1989 to March 1991

Mechanical Engineer. Lead engineer for design, development, and manufacture of the MKII Treadmill and Cycle Ergometer for Space Shuttle deployment. Project engineer of the Multi-Function Exercise Device development team. Leadership responsibilities included providing technical direction for software, electrical, and mechanical engineering personnel. Engineering responsibilities involved device design and analysis, schedule and cost assessments, hardware fabrication, assembly and test.

Pennsylvania State University
University Park, PA August 1987 to August 1989

Graduate Research Assistant. Applied optimal control theory to minimize energy consumption of a battery powered artificial heart. Implemented theoretically derived control algorithm with clinical hardware and conducted *in-vitro* laboratory tests to validate performance.

General Dynamics
San Diego, CA June 1986 to August 1987

Mechanical Design Engineer. Designed and tested components for submunition dispensing Tomahawk cruise missile.

SERVICE:

Professional Activities:

Reviewer for:

IEEE Transactions on Rehabilitation Engineering
IEEE Transactions on Robotics and Automation
IEEE Control Systems Magazine

Society Memberships:

Institute of Electrical and Electronics Engineers
American Society of Mechanical Engineers

Community Activities:

Commodore July 1997 to October 1998

Washington Yacht Club

Description: Head of organization whose mission is to promote sailing among the students, staff, faculty, and alumni of the University of Washington. Responsible for $15k annual budget.

Volunteer Autumn 1994 & Summer 1995

University of Washington Disabled Students Association

Description: Generated lecture notes for disabled students in Neural Behavior and Anatomy classes.

HONORS and AWARDS:

Honorary Lifetime Member October 1998

Washington Yacht Club

Awarded for “Exemplary Voluntary Service.”

David C. Auth Fellowship Autumn 1997

Electrical Engineering Department, University of Washington.

Electrical Engineering fellowship for research involving bioengineering.

Golden Eagle Award September 1992

NASA Johnson Space Center

Awarded for “Excellence in Research for Manned Spaceflight Programs.”